

DISS. ETH NO. 27934

Single cell engineering using fluidic force microscopy

A thesis submitted to attain the degree of
DOCTOR OF SCIENCES of ETH ZURICH

(Dr. sc. ETH Zürich)

presented by

Christoph Georg Erich Gäbelein

MSc, Albert-Ludwigs-Universität Freiburg

born on 04.10.1988

citizen of Germany

accepted on the recommendation of

Prof. Dr. Julia Vorholt

Prof. Dr. Matthias Peter

Prof. Dr. Sophie Martin

2021

Table of contents

Summary	5
Zusammenfassung	7
I Introduction	
1.1 Technologies in single cell analysis	10
1.2 Single-cell extraction and injection technologies	11
1.3 Fluidic force microscopy (FluidFM)	14
1.4 Molecule delivery into fungal cells	16
1.5 Controlled manipulation of organelle structures within single cells	17
1.6 Genetic manipulation of mitochondria	18
1.7 Mitochondrial quality control	20
1.8 Synthetic minimal systems in Symbiogenesis	24
1.9 Aims and outline of this thesis	26
1.10 References	27
II Injection into and extraction from single fungal cells	37
III Mitochondria transplantation between living cells	63
IV Engineering of synthetic endosymbioses using FluidFM injection of bacteria into host cells	118
V Discussion and outlook	134
Acknowledgements	146

Summary

Cells are the smallest units of life. The study of single cells as the universal building blocks of life is essential to advancing the understanding from cellular evolution to collective behavior of multicellular systems. Increasingly precise tools are being developed to enable insights into patterns and mechanisms governing the behavior of individual cells, which are themselves inherently complex systems. Fluidic force microscopy (FluidFM) unites the high spatial precision of an atomic force microscope (AFM) with the capability to control fluid flows. FluidFM cantilevers are hollow rigid structures that are supported at one end, composed of silicon nitride and with dimensions in the micrometer range. The apex carries a structural element, consisting of a pyramid or a cylinder, which interacts directly with the biological sample. These structural features can be further shaped using focused ion beam technology, allowing removal of material with nanometer precision. The hollow interior acts as a microchannel that is connected to an external pressure controller to regulate fluid flow into -and out of the cantilever through an aperture located at the apex. The aperture is the critical area of the cantilever concerning the ability to perturb fluidic flow and pressure, as it is the connecting point between the sample and the pressure controlled fluidic system. In addition, its size restricts the transported substances by affecting the range of acting fluid forces and forming a steric barrier for objects smaller than its own extent. In the presented work, the position and size of pyramidal and cylindrical cantilevers were tuned to allow injection and extraction from and into various cell types, as well as the extraction and re-injection of organelles from and into cultured mammalian cells and injection of bacteria into cultured mammalian cells.

In the first part of this thesis, minimization of aperture area as well as precise positioning of the aperture was crucial to manipulate fungi. Injection and extraction of fluids in walled fungal cells is challenging and the most common methods for delivery into fungi rely on the generation of protoplasts using cell wall degrading enzymes. This step represents a bottleneck when working with different species, in terms of experimental time and cell viability. Here, it was shown that FluidFM enables the injection of solutions into the cytoplasm of fungal cells as well as the extraction of cytoplasmic fluids from fungal cells, including the unicellular yeasts *Schizosaccharomyces pombe* and *Saccharomyces cerevisiae* and the multicellular fungus *Coprinopsis cinerea*. The approach preserves cell viability and allows for the study of cell responses of chemical as well as physical stimuli. Active transport of a fluorescently labelled protein carrying a nuclear localization signal to cell nuclei after injection was observed, as were transcriptional responses following extraction of cytoplasm from the syncytial fungus *C. cinerea*.

In the second step, the aperture area of FluidFM probes and concomitant hydrodynamic forces were optimized towards exertion of larger forces and cylindrical cantilevers were sharpened to allow minimally invasive organelle manipulation in cultured mammalian cells. Mitochondria and the complex endomembrane system are hallmarks of eukaryotic cells, which are difficult to manipulate in a spatially defined fashion. The developed approach allows extraction and transplantation of organelles from, and into, cultured live cells. Impaired mitochondria from HeLa cells were transplanted into primary keratinocytes and the fate of mitochondria after transplantation was followed in real time. The established protocol made it possible to observe subsequent remodeling and rescue of transferred mitochondrial subpopulations. Moreover, mitochondria can be studied in different nuclear backgrounds as their genomic content is propagated without the need for selection pressure. When extracting individual- or groups of mitochondria, their morphology transitions into a pearls-on-a-string phenotype, resulting in fission along tens of micrometers along mitochondria due to locally applied pulling forces. Studying the force induced pearling process, it was shown that the transition is calcium-signaling independent and coincides with recruitment of the canonical mitochondrial fission machinery.

In the third chapter, the use of sharpened cylindrical cantilevers was extended to facilitate the injection of bacteria into mammalian cells. By creating a synthetic merger of a cell-within-a-cell, a defined starting point for an emerging endosymbiosis can be initiated. Here, two heterotrophic organisms, mammalian HeLa cells and *Escherichia coli* bacterial cells were brought together. The intracellular growth behavior was analyzed using fluorescence microscopy and rapid growth of *E. coli* observed, leading to an unstable relationship. In order to impede this excessive growth behavior, auxotrophic mutants of *E. coli* were created. Intracellular growth was robust towards mutational load in amino acid synthesis and prone to pleiotropic effects when creating bottlenecks in purine metabolism. Hence, the system requires further engineering towards a stable synthetic merger.

In summary, the technological advances introduced in this work were translated towards the use in relevant biological systems beyond the establishment of technical proof of principles. Additionally, they provide powerful tools for single cell research across fields of biological research.

Zusammenfassung

Zellen sind die kleinsten Einheiten des Lebens. Die Untersuchung einzelner Zellen als universelle Bausteine des Lebens ist für das Verständnis der zellulären Evolution und des kollektiven Verhaltens multizellulärer Systeme von wesentlicher Bedeutung. Es werden immer präzisere Werkzeuge entwickelt, die Einblicke in die Muster und Mechanismen ermöglichen, die das Verhalten einzelner Zellen bestimmen, die ihrerseits komplexe Systeme sind. Die Fluidkraftmikroskopie (FluidFM) vereint die hohe räumliche Präzision eines Rasterkraftmikroskops (AFM) mit der Fähigkeit, Flüssigkeitsströme zu kontrollieren. FluidFM-Cantilever sind hohle, starre Strukturen, die an einem Ende gestützt werden, aus Siliziumnitrid bestehen und Maße im Mikrometerbereich haben. Die Spitze trägt ein Strukturelement, bestehend aus einer Pyramide oder einem Zylinder, das direkt mit der biologischen Probe interagiert. Diese Strukturelemente können mit der fokussierten Ionenstrahltechnologie weiter geformt werden, was einen Materialabtrag mit Nanometerpräzision ermöglicht. Der hohle Innenraum fungiert als Mikrokanal, der mit einem externen Druckregler verbunden ist, um den Flüssigkeitsstrom in den und aus dem Cantilever durch eine Öffnung an der Spitze zu regulieren. Die Öffnung ist der kritische Bereich des Cantilevers in Bezug auf die Fähigkeit, den Flüssigkeitsstrom und den Druck zu beeinflussen, da sie der Verbindungspunkt zwischen der Probe und dem druckgesteuerten Flüssigkeitssystem ist. Darüber hinaus schränkt ihre Größe die transportierten Substanzen ein, indem sie den Bereich der wirkenden Fluidkräfte beeinflusst und eine sterische Barriere für Objekte bildet, die kleiner als ihre eigene Ausdehnung sind. In der vorliegenden Arbeit wurden Position und Größe von pyramidalen und zylindrischen Cantilevern so abgestimmt, dass sie die Injektion und Extraktion aus und in verschiedene Zelltypen sowie die Extraktion und Re-Injektion von Organellen aus und in kultivierte Säugetierzellen und die Injektion von Bakterien in kultivierte Säugetierzellen ermöglichen.

Im ersten Teil dieser Arbeit war die Minimierung der Öffnungsfläche sowie die präzise Positionierung der Öffnung entscheidend für die Manipulation von Pilzen. Die Injektion und Extraktion von Flüssigkeiten in wandständige Pilzzellen ist eine Herausforderung, und die gängigsten Methoden zur Substanzeinbringung in Pilze beruhen auf der Erzeugung von Protoplasten unter Verwendung von zellwandabbauenden Enzymen. Dieser Schritt stellt bei der Arbeit mit verschiedenen Arten einen Engpass in Bezug auf die Versuchsdauer und die Lebensfähigkeit der Zellen dar. Hier wurde gezeigt, dass FluidFM die Injektion von Lösungen in das Zytoplasma von Pilzzellen sowie die Extraktion von Zytoplasmaliquiden aus Pilzzellen ermöglicht, einschließlich der einzelligen Hefen *Schizosaccharomyces pombe* und *Saccharomyces cerevisiae* und des mehrzelligen Pilzes *Coprinopsis cinerea*. Der Ansatz erhält die Lebensfähigkeit der Zellen und ermöglicht die Untersuchung der Zellreaktionen auf

chemische und physikalische Reize. Nach der Injektion eines fluoreszierend markierten Proteins, das ein Kernlokalisierungssignal trägt, wurde ein aktiver Transport zu den Zellkernen beobachtet, ebenso wie transkriptionelle Reaktionen nach der Extraktion von Zytoplasma aus dem synzytialen Pilz *C. cinerea*.

Im zweiten Schritt wurden die Öffnungsfläche der FluidFM-Proben und die damit verbundenen hydrodynamischen Kräfte optimiert und die Öffnung der zylindrischen Ausleger geschärft, um eine minimal invasive Manipulation von Organellen in kultivierten Säugetierzellen zu ermöglichen. Mitochondrien und das komplexe Endomembransystem sind charakteristische Merkmale eukaryontischer Zellen, die nur schwer räumlich definiert manipuliert werden können. Der entwickelte Ansatz ermöglicht die Extraktion und Transplantation von Organellen aus und in kultivierte lebende Zellen. Beeinträchtigte Mitochondrien aus HeLa-Zellen wurden in primäre Keratinozyten transplantiert, und das Verhalten der Mitochondrien nach der Transplantation wurde in Echtzeit verfolgt. Das etablierte Protokoll ermöglichte es, den anschließenden Umbau und die Rettung der übertragenen mitochondrialen Subpopulationen zu beobachten. Darüber hinaus können Mitochondrien in verschiedenen Kernhintergründen untersucht werden, da ihr genomischer Inhalt ohne Selektionsdruck vermehrt wird. Bei der Entnahme von einzelnen Mitochondrien oder Gruppen von Mitochondrien geht deren Morphologie in einen Perlen-auf-einer-Schnur-Phänotyp über, was zu einer Spaltung entlang von mehreren Mikrometern entlang der Mitochondrien aufgrund von lokal angelegten Zugkräften führt. Bei der Untersuchung des kraftinduzierten Perlbildungsprozesses konnte gezeigt werden, dass der Übergang kalziumunabhängig ist und mit der Rekrutierung der kanonischen mitochondrialen Spaltungsmaschinerie zusammenfällt.

Im dritten Kapitel wurde die Verwendung von geschliffenen zylindrischen Cantilevern erweitert, um die Injektion von Bakterien in Säugetierzellen zu erleichtern. Durch die Schaffung einer künstlichen Verschmelzung einer Zelle mit einer Zelle kann ein definierter Ausgangspunkt für eine entstehende Endosymbiose geschaffen werden. Hier wurden zwei heterotrophe Organismen, HeLa-Säugetierzellen und *Escherichia coli*-Bakterienzellen, zusammengebracht. Das intrazelluläre Wachstumsverhalten wurde mit Hilfe von Fluoreszenzmikroskopie analysiert und ein schnelles Wachstum von *E. coli* beobachtet, was zu einer instabilen Beziehung führte. Um dieses exzessive Wachstumsverhalten zu unterbinden, wurden auxotrophe Mutanten von *E. coli* eingesetzt. Das intrazelluläre Wachstum war robust gegenüber Mutationen in der Aminosäuresynthese und anfällig für pleiotrope Effekte, wenn Engpässe im Purinstoffwechsel entstehen. Daher muss das System weiter entwickelt werden, um eine stabile künstliche Fusion zu erreichen.

Zusammenfassend lässt sich sagen, dass die in dieser Arbeit vorgestellten technologischen Fortschritte über den funktionellen Nachweis hinaus auf die Anwendung in relevanten

biologischen Systemen übertragen wurden. Zusätzlich bieten sie wirksame Werkzeuge für die Einzelzellforschung in verschiedenen Bereichen der Biologie.

I Introduction

Technologies in single cell analysis

The cell is the smallest unit of life and every step taken in the evolution of life is based on a genetic change initially occurring in an individual cell. The timeframe in which genetic changes drive transition in behavior and genotype of a population are dependent on the impact of the introduced selective advantage within a given environment. These fundamental principles of evolution initially laid out in Darwin's description of speciation of animals¹ were substantiated in the earliest experiments on bacterial populations in the fully artificial environment of chemostats²:

"Manifestation of "Evolution" in the Chemostat. If a bacterial strain is grown over a long period of time in the Chemostat, from time to time a mutant might arise which grows faster, under the conditions prevailing in the Chemostat, than the parent strain. If this happens, practically the entire bacterial population in the Chemostat will change over from the parent strain to the new strain."

Novick and Szilard, *Science* 36, 1950

Thus, all shifts occurring in nature begin with the change of a singular cell within a larger population, be it bacteria in Chemostats, or in the evolution of mammals.

Limited by technology in terms of precision and sensitivity, biological studies historically focus on the investigation of cell populations rather than the behavior of single cells. However, since all evolutionary changes arise from single cell events, their investigation is central in understanding life's complexity. Furthermore, even if a cell population shares the same genetic information, variations in their state may give rise to heterogeneous responses to stimuli due to stochastic behavior or varying microenvironments^{3,4}. In recent years, the number of novel discoveries based on single cell studies rose rapidly. This development was driven by technological innovations that allow the investigation of biological processes in higher detail, be it in time and space via microscopy or at the molecular level, i.e. protein, metabolite or mRNA, using 'omics' technologies. This general trend is reflected in the relative interest search score for the terms 'single cell', 'single cell analysis' and 'single cell sequencing' (Fig. 1).

The study or manipulation of individual cells requires either their separation in space, e.g. via (micro) fluidic devices⁵ for subsequent analysis, or their direct manipulation and analysis *in situ*. Single cell analysis following cell isolation enables high throughput and connection with

'omics' technologies for downstream analysis, but all spatial context is lost. *In situ* studies rely on the high spatial resolution provided by microscopy methods and

are just beginning to link to 'omics' technologies via single cell sampling techniques⁶⁻⁸. Methods for single cell sampling and manipulation *in situ* additionally allow measurement of multiple time points if they are able to preserve cell viability while manipulating or extracting part of the cell content. In this thesis, the focus lies on the development of new techniques for minimally invasive manipulation and analysis of single cells using fluidic force microscopy (FluidFM)⁹, in combination with light microscopy for parallel analysis.

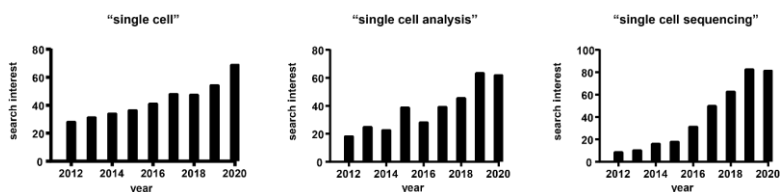


Figure 1: Popularity of search terms related to single cell technologies since 2012. Data from trends.google.com. The search interest is based on the popularity of indicated terms based on the absolute number of searches of indicated terms relative to the total number of searches received by

Single-cell extraction and injection technologies

Monitoring individual cells at different time points is crucial for understanding fundamental cellular processes. In time-resolved experiments, single cell technologies are used either to analyze globally induced stimuli at the single-cell level, or to perturb individual cells and subsequently monitor the cells' response to the stimulus. In both cases, miniaturized probes are powerful tools that combine high spatiotemporal control with minimal invasiveness.

Standard single cell analysis protocols are destructive and involve lysis of the cells, effectively ruling out dynamic studies over multiple time points. However, techniques for the extraction of small quantities of the cytosol of cells without impairing cell viability have been established in recent years¹⁰. The aim of single cell sampling techniques is to take a snapshot of a cell at a given time via downstream analysis of the extract, which requires sample amounts in the range of picoliters (pL)^{7,11}. To facilitate cell entry and defined extraction of cytosolic components, miniaturized probes are directly inserted. The probes are traversed by a microfluidic channel that allows controlled directional fluid flow into or out of the inserted device. Probes have been designed to be in a similar size range as the analyzed cell to improve spatial precision while preserving cell viability during cell entry (Fig. 2)¹¹. Several studies show engineering of hollow glass needles to deliver and extract small molecules and particles into and from cultured

cells. The use of glass needles as micro-injection tools emerged in the 1970's¹² i.e. for the intracytoplasmic injection of sperm into oocytes with a glass needle of an inner diameter of approximately 10 μm ¹³. Building on these early successes, the approach was later refined and modified.

Nanopipette-based methods use fine glass needles with an aperture pore size of around 50-100 nm in diameter^{14,15}. These needles can be integrated into a scanning ion conductance microscope (SICM). SICM was developed to image cells by measuring the current between the glass needles interior and the surrounding media. The measured current changes depending on the probes proximity to the surface, close proximity increasing the resistance, effectively allowing mapping of surfaces without requiring physical contact¹⁶. Extraction of molecules is achieved utilizing the potential-induced change of surface tension of 1,2-di-chloroethane, a process termed electrowetting, causing aqueous solutions to flow into the Nanopipette¹⁷. The volume typically extracted via Nanopipettes ranges around 50 femtoliters (fL). The high precision Nanopipettes was demonstrated to facilitate extraction of mRNA¹⁸, proteins and single mitochondria¹⁵.

Another refinement of glass needles can be achieved by combining them with carbon nanotubes, which was used for 'cellular endoscopies'¹⁹. Here, a carbon nanotube is placed at the tip of a glass pipette. Carbon nanotubes are even smaller (50-200 nm in diameter) and were shown to facilitate minimally invasive cell entry, extraction of fluorescently labelled Ca^{2+} and

Four ways for removing cell contents

Cao et al. used 150-nm-diameter alumina nanostraws combined with electroporation to extract cellular contents for analysis. This method complements nanobiopsy, fluid force microscopy, and carbon nanotube endoscopy.

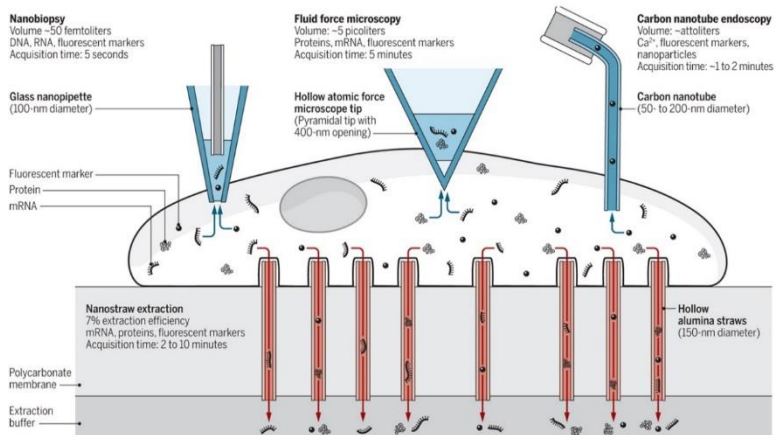


Figure 2: Four ways for removing cell contents: Nanobiopsy, Carbon nanotube endoscopy, Nanostraw extraction and fluid force microscopy. (Figure from Higgins and Stevens¹¹.)

delivery of fluorescent nanoparticles. However, they are limited to low amounts of liquid (attolitre volumes).

Glass micropipettes can also be chemically modified for the delivery of 'large cargo' i.e. bacteria or mitochondria into mammalian cells in a device termed the photothermal nanoblade^{20,21}. This technique has been exclusively used for cell injection. The authors used titanium (Ti) coated glass pipettes to facilitate cell entry by locally heating up the Ti layer via a laser pulse, resulting in local bubble formation cutting the cell membrane when in proximity to the probe. Using simultaneous exertion of positive pressure via a coupled pressure control system connected to the glass pipet, the authors showed injection of *Burkholderia thailandensis* into HeLa cells²⁰.

Beyond miniaturized probes for single cell sampling and injection, microfluidic- embedded substrates facilitate analysis and manipulation of adherent cells, although not necessarily designed for single cell studies. In Nanostraw extraction²², adherent cells are cultivated on top of a polycarbonate membrane traversed by Nanostraws that connect the cell interior to a small reservoir of extraction buffer kept below the membrane (see Fig. 2). Cell entry is facilitated by electroporation permitted by connecting the bottom of the system to an indium tin oxide electrode and immersing a platinum electrode into the cell culture media at the top of the setup. The method offers 7% extraction efficiency by diffusion of molecules into the extraction buffer. The authors show downstream analysis of extracted mRNA and multiple time point sampling of usually several cells.

The biophotonic laser-assisted surgery tool (BLAST)²³ is based on a similar principle; however, focusses on the delivery of particles and cells into multiple cultured cells. Again, the cells are cultivated over a porous SiO₂ membrane that separates the cargo storage buffer below from the cell culture medium on top. The pores of the membrane are coated with a thin titanium membrane that can be stimulated for bubble formation similar to the photothermal nanoblade described above. Reminiscent of the electroporation protocol of Nanostraw injection, this opens up small pores into the cells cultivated on top. Pressure driven flow subsequently drives particles kept in the storage buffer below into the cells' cytoplasm. The authors show efficient delivery of *Listeria monocytogenes* and *Francisella novicida* bacterial cells into cultured mammalian cells.

All tools for single cell analysis and manipulation described above show different strengths and weaknesses. Miniaturized probes generally allow high precision in time and space and preserve cell viability but are limited in throughput because only one cell can be probed at a time and automation is limited. Additionally, narrow apertures and thin fluidic channels (~50- 200 nm in diameter) are generally susceptible to clogging. Microfluidic-embedded substrates offer higher throughput at the cost of spatial resolution and the extracted molecules are hard to analyze because they are diluted by several orders of magnitude from femtoliters (10⁻¹⁵ l) to microliters

(10^{-6} l). The inability to control extracted and injected volumes together with a narrow working range of each individual technique is limiting their connection to downstream analyses.

Fluidic force microscopy (FluidFM)

Fluidic force microscopy⁹ is a technique that enables control over the amount of liquid extracted or injected into single cells (fL to pL)^{24,25}. The setup falls into the class miniaturized probes used for serial processing of cultured cells. FluidFM combines atomic force microscopy (AFM) with microfluidics (Fig. 3), creating a tool that adds two tunable parameters to the

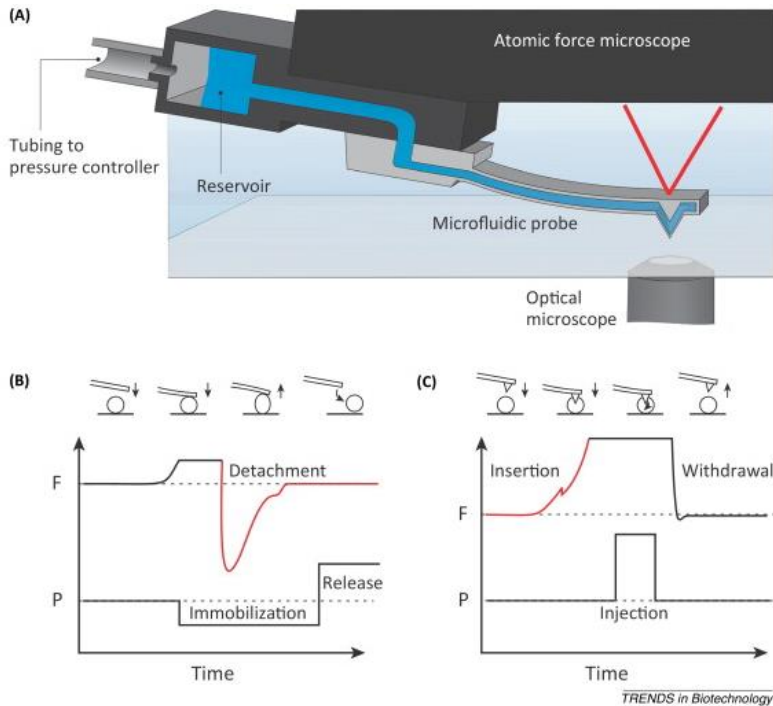


Figure 3: The fluidic force microscopy (FluidFM). (A) Schematic of a FluidFM system, which combines an atomic force microscope with a microfluidic probe on top of an inverted optical microscope; the watertight pipeline from the pressure controller to the probe aperture enables operation in liquid. (B) Force (F) and pressure (P) progress during a cell adhesion measurement by FluidFM. (C) Force (F) and pressure (P) progress during an intracellular injection by FluidFM. (Figure and description taken from Guillaume-Gentil et al.¹⁴⁸)

miniaturized probes used for single cell sampling and injection described above: The first parameter is the capability of atomic force microscope. AFM was first published in 1985²⁶, it is based on directly measuring the inclination of a probe, termed cantilever, upon its interaction with a given substrate. The technique quickly moved from high vacuum conditions to physiological experiments conducted in aqueous solution (1989)²⁷ paving the way for its use to study and manipulate biological systems *in situ*. The technique allows precise control of five dimensions within an experiment, piezo-driven positioning of the cantilever in time, space (x-y-z) and force, enabled by monitoring the tip-surface interaction using deflection of a laser beam reflected on the probe surface. The laser deflection (d) can be translated to forces (F), knowing the spring constant (k) of the used probe: $F = k \times d$. This fifth dimension of force is used for direct readout of sample properties such as stiffness or adhesion- and to control the probe position in the z dimension in ‘force spectroscopy’ via direct force measurement – and force-feedback of the piezoelectric element. Force spectroscopy is also used to drive the FluidFM cantilever into the nucleus or cytoplasmic compartment of cultured cells without comprising their viability and allowing for minute positioning of the probe in respect to the upper- and lower cell membrane²⁵. Beyond time, space and force, the hydrodynamic pressure within the hollow FluidFM cantilevers can be controlled with millibar resolution. FluidFM uses a standard external pressure controller to set the pressure within the microfluidic system within a range of -800 to +1000 mbar. Pressure control is used to locally dispense agents²⁸, repeatedly immobilize and release small objects like cells or beads for isolation²⁹ or for cell adhesion measurements combined with force sensing³⁰⁻³². The exerted pressure also has direct effect on the injection or extraction process modulating volume flow over time and exerting hydrodynamic forces in dependence of aperture area following:

$$F = p \times A$$

$F = \text{magnitude of normal force}$
 $p = \text{pressure}$
 $A = \text{aperture area}$

However, pressure control alone is not sufficient to quantify injected-or extracted volumes, as they vary from cell to cell. Therefore, simultaneous optical control is crucial. Coupling of FluidFM with an optical microscope allows for real-time observations and tuning of the injection-and extraction process. Thus, the injection process can be manually adjusted to inject a range of volumes into mammalian cells²⁵, e.g. observing accumulation of a fluorophore during injection- or by monitoring injection-induced bleb formation on the outer cell membrane.

Extracted volumes can be monitored by using immiscible mineral oil as the liquid phase inside the cantilever, since the refractive index of the oil differs from the index of water, thus creating two visibly separated phases during cell extraction^{24,33}. The low-impact of probe positioning and the ability to extract, quantify and dispense- or inject a wide range (fL - pL) of volumes increases the working range of FluidFM compared to the tools introduced above. FluidFM cantilevers used for single cell injection and extraction comprise a pyramidal apex comprising a triangular aperture with a height-and width of 400 nm²⁵. Other concepts for cantilever fabrication allow the creation of novel cantilever geometries, offering a possible angle for novelties³⁴. Furthermore, the cantilever design and aperture size can be further refined using focused ion beam (FIB) technology³⁵. This leaves room for further improvement and expansion of the range of exerted hydrodynamic and mechanical forces by the FluidFM technology.

Molecule delivery into fungal cells

Fungi represent a vast range of eukaryotic organisms that group in the eukaryotic taxon of ‘Amorpha’, together with animals³⁶. Fungal cells and organisms are very diverse in terms of genetics- and cell structure, ranging from purely single celled yeasts to large filamentous organisms expanding over several hectares³⁷. Fungi harbor a huge potential for industry and fundamental research³⁸, requiring the need for chemical and genetic manipulation. However all fungi are protected by a cell wall, acting as a structural barrier maintaining cell shape- and shielding against unwanted physical stimuli. The cell wall composition of fungi is composed mainly of chitin or cellulose microfibrils, varying greatly in cross-linking and chemical composition³⁹. The wide range of cell wall composition is hindering unified protocols for transformation, especially for filamentous fungi⁴⁰. All available transformation protocols provide means to loosen the cell wall integrity in order to facilitate delivery of substances.

Molecule delivery methods usually rely on the formation of fungal protoplasts⁴¹. Protoplasts are commonly created by the use of lytic enzymes⁴². Due to the diverse chemical composition of fungal cell walls, protocols for cell wall degradation via one or several lytic enzymes need to be established separately for each organism. In 1978, Hinnen and coworkers showed that a leucine auxotrophic strain *Saccharomyces cerevisiae* protoplasts could be readily transformed into a prototroph, when protoplasts were incubated in presence of plasmidic wild-type DNA and CaCl₂⁴³. In the following years, similar transformation protocols were established for other fungal species⁴⁴. Protoplasts were also used in combination with the addition of polyethylene glycol (PEG) to introduce larger structures into yeast cells such as whole genomes⁴⁵ or isolated mitochondria⁴⁶.

Effective transfer of DNA into yeast cells has also been shown to function after the addition of monovalent cations, particularly Li^{+47} . The transformation efficiency was highest in combination with PEG and heat shock at 42°C . The use of Li^{+} was later expanded further fungal species such as *Pichia pastoris* and *Schizosaccharomyces pombe*⁴⁸. Another prominent DNA transfer method is electroporation, having a similar ability to introduce DNA and even macromolecules such as dextran into *S. pombe* cells⁴⁹.

From a purely mechanical standpoint, fungal cell walls vary in stiffness between species and even within individual cells^{50,51}, within a defined window⁵². This fact is exploited by a range of methods, including the use of shear forces and shock-waves for protoplast formation⁴⁰. Partida-Martinez et al. showed transformation induced by outer membrane damage via a laser beam. The protocol facilitated the incorporation of fluorescently labelled bacteria into *Rhizopus microsporus* hyphae. However the correlation between the laser-beam induced membrane damage and the bacterial host-invasion remains vague⁵³. In 2015, *S. pombe* cells were successfully immobilized on microstructures and subsequently subjected to mechanical shear-stress induced by a micropipette, damaging the cell wall and membrane and allowing some of the simultaneously released dye to enter the fungal cell⁵⁴. These methods, relying on non-enzymatic cell perturbation, show promising results, but have not been investigated further, leaving much to be desired in terms of efficiency and throughput. The use of miniaturized probes is problematic for the injection of fungal cells, because it requires prior immobilization on a substrate or microstructure and weakly immobilized cells are prone to evade the probe via lateral movement, making probe insertion impossible. FluidFM has the technical benefit of force-feedback during probe positioning, allowing a controlled establishment of probe-cell contact. Furthermore, AFM probes approach the sample from a 90° angle, which limits the probability of the cell to evade the strain via lateral evasion. Together with the possibility to produce stiff cantilevers that are able to exert high forces ($>5 \mu\text{N}$), FluidFM is a promising tool for the injection into fungal cells.

Controlled manipulation of organelle structures within single cells

Eukaryotic cells harbor numerous organelles that form a highly dynamic ensemble⁵⁵⁻⁵⁷. Organelles subdivide eukaryotic cells into dedicated compartments separated by biological membranes. Each compartment being unique in its cellular task and chemical composition. Their intertwined relationships complicate the study of individual tasks of organelles. To date, sampling methods rely on purification protocols from bulks of cells, connected to various downstream analyses⁵⁸. Cell biological studies usually perturb the state of the cell as a whole e.g. via drug-treatments or genetic perturbations, not achieving local perturbation of individual parts

of the cell. Defined tools for the study of mechanical responses of ‘whole’ cells include a wide range of methods, e.g. AFM⁵⁹, microfluidic tools⁶⁰, micropipette aspiration⁶¹ and optical tweezers⁶². These techniques fostered the knowledge on cell responses to mechanical stimuli in mammalian cells, which initially could not be connected to molecular mechanisms. Engler et al (2006) showed that substrate stiffness impacts stem cell differentiation⁶³ and a mammalian mechanoreceptor, Piezo1, was discovered in 2014⁶⁴. Later, mechanical strain was directly connected with calcium gating, ‘mechanogating’, by Piezo1⁶⁵. These findings boosted the young field of mechanobiology. Mechanical perturbation of whole cells can be linked to mechanistic insights using techniques facilitating single-cell readouts: Aragona et al. establish a connection between cell-stretching and skin expansion due to transcriptomic changes using a combination of a self-inflating hydrogel with microscopy and single cell RNA sequencing⁶⁶.

Studies focusing on the perturbations of individual cell compartments are rare. To perturb individual organelles, optogenetic tools were developed to locally affect organelle positioning, while inducing mechanical shear-forces created by motor-proteins⁶⁷. This was shown to effect axon outgrowth in hippocampal neurons, which could be connected to local positioning of recycling endosomes. Elevated local concentration of endosomes enhanced growth, while removal of endosomes reversibly suppressed axon growth.

Local damage can be caused using optically induced photosensitizers, who generate cytotoxic reactive oxygen species (ROS) when illuminated. The laser-induced catalysis of ROS was used to locally damage mitochondria, showing a localized degradation of damaged mitochondria^{68,69}.

Apart from optogenetics, AFM studies show localized measurements of organelles, usually in the cell periphery, or are able to exert local mechanical forces while simultaneously following organelle responses^{50,70,71}. Mitochondria undergo constant rearrangement within mammalian cells and are able to switch between morphological states, either forming a large connected network, or many isolated spheres⁷². This dynamic behavior puts the focus on regulatory mechanisms of mitochondrial shape. An influence of mechanical forces and dynamic mitochondrial fission was speculated^{73,74} and later experimentally established⁷⁵, using a combination of mechanical perturbation via AFM and motile intracellular bacteria.

Genetic manipulation of mitochondria

Within the ensemble of membrane compartments mitochondria hold a special place: they are at the heart of energy conversion of most eukaryotic cells and link cellular metabolism to signaling pathways and cell fate decision⁷⁶. Furthermore, mitochondria in extant eukaryotes are the remainder of an ancient endosymbiosis that led to the emergence of eukaryotes⁷⁷. The

presence of a DNA pool outside of the nucleus, which is distributed and propagated within the mitochondrial network is one of the cornerstones of endosymbiotic theory⁷⁸. The mitochondrial genome of humans is a circular, double stranded molecule containing 37 genes, with a separate set of repair mechanisms, compared to nuclear DNA⁷⁹. Each mammalian cell preserves a pool of mitochondrial DNA (mtDNA) molecules comprising different variants, usually differing in single nucleotide polymorphisms (SNPs), and varying copy numbers. The heteroplasmic nature of mitochondrial genomes and the high mutation rate exacerbates genotype to phenotype correlations as well as the study of mtDNA inheritance⁸⁰. The mitochondrial genome is prone to accumulation of erroneous mutations, associated with to a number of inherited diseases and aging in humans⁸¹⁻⁸³; however, depending on the type of mutation, a threshold value of over 25 - 90% of mutant mtDNA is required in order to show a phenotype⁸⁴. To deplete such defective mitochondrial DNA sequence variants *in vivo*, genetic tools have been employed successfully^{85,86}. These genetic approaches utilize the nature of mtDNA repair mechanisms: DNA strands experiencing a double strand break are rapidly degraded⁸⁷. This knowledge was exploited by targeting pathogenic mtDNA variants and inducing double-strand breaks using transcription activator-like effector nucleases targeted to mitochondria (mitoTALENs), leading degradation of said mtDNA⁸⁸. While the removal and study of present mtDNA variants is feasible, approaches for the introduction of novel mtDNA sequences remain challenging^{89,90}. In order to be propagated within a new host cell, mtDNA has to be surrounded by a double membrane that is either able to facilitate protein import from a new host cell, or is able to fuse with the host mitochondrial network. Furthermore, it needs to be recognized and propagated by the host cells' mtDNA replication machinery.

Early studies show that mtDNA sequences carrying resistance markers can be introduced by mitochondrial transformation under selective pressure, showing a possibility for non-specific uptake of mtDNA sequences in cultured cells⁹¹. This protocol was later refined using centrifugal force to elevate transfer efficiency, still relying on non-specific mitochondrial uptake of mitochondria and mtDNA⁹². Cytoplasmic cell-cell fusion approaches show creation of cybrid (cytoplasmic hybrid) cells based on chemically assisted cell fusion. This technique allows creation of cells with mixed mitochondrial content, when fusing a cell with a enucleated cell, or of cells having a fully exchanged mitochondrial content when fusing a enucleated cell with a cell previously depleted of their mtDNA (rho0-cell)⁹³. Enucleated cells can be artificially created, or blood platelet cells, naturally devoid of a nucleus, can be used. Cybrid cells were used to investigate whether mitochondria from primates are able to re-establish functional oxidative phosphorylation in human rho0-cells, showing that mtDNA from closely related primates (chimpanzee, pigmy chimp and gorilla) shows compatibility with human nuclear DNA in 'xenomitochondrial hybrids'⁹⁴.

Introduction of mtDNA variants via injection into oocytes or embryonic stages of *Drosophila* was established in the 1980's: Microinjection techniques were developed to create trans-mitochondrial flies⁹⁵. The generated mitochondrial hybrids were used to study selection on mitochondrial genomes within the germline, showing that mitochondrial fragmentation is not only necessary, but even sufficient to trigger selection on defective mtDNA variants in other tissues⁹⁶. Similar microinjection approaches were used to follow the fate of injected mitochondria into mouse oocytes and modes of mitochondrial selection in early embryo development⁹⁷.

Using a modified microcapillary pipet²¹ or microfluidic-embedded substrate⁹⁸, a delivery of mitochondria into somatic rho0-cells was achieved, with an efficiency of mtDNA delivery to about 2 to 25 % of the targeted cells respectively. Although mitochondria can be introduced into cells, the rate of successful transfer of individual mitochondria into cultured single cells is still low and therefore requires subsequent selection of successfully transformed cells. This limits mitochondrial transplantation and inheritance of introduced mtDNA under nonselective conditions.

Koob and colleagues focus on another layer of mtDNA manipulation: cloning and engineering of entire mitochondrial genomes⁹⁹. While mtDNA molecules can be technically manipulated and cloned outside of mitochondria, their functional re-introduction into cells difficult. Several attempts were made to introduce plasmids into mitochondria via electroporation⁹⁹ or bacterial conjugation¹⁰⁰ and the authors showed active transcription of the introduced plasmids *in vitro*. Unfortunately, the mitochondria were not functional when introduced into human cells. Later, introduction and maintenance of mammalian mitochondrial genomes into the yeast mitochondrial network⁹⁰ of rho0-cells was shown but functional transfer is still lacking.

Mitochondrial quality control

Mitochondria are a hub in cell metabolism, playing a central role in fatty acid metabolism, synthesis of iron sulfur clusters, amino acid synthesis and generation of ATP. Generation of the cellular 'energy currency' is based on functional oxidative phosphorylation complexes I – V and their ability to generate a membrane potential across the inner mitochondrial membrane and to use it, converting ADP + Pi to ATP. Components of these complexes are encoded in the mitochondrial genome (see above). This process carries the risk of creating reactive oxygen species (ROS), damaging mitochondria¹⁰¹. To protect mitochondria from excessive damage, ROS can be locally detoxified to H₂O₂ by the nuclear encoded superoxide dismutase and later to O₂ and H₂O. However, damaging events are inevitable, potentially threatening cell function and

survival, because mitochondria are also central players in apoptosis activation¹⁰². ROS-induced damage and the high mutation rate of mtDNA require an active machinery to keep mitochondrial quality in check and to selectively remove damaged mitochondria in order to maintain eukaryotic cell function. Genetic studies suggest that unfavorable mtDNA haplotypes are selected against in humans, influencing mitochondrial genome diversity¹⁰³. These selection processes may occur on several levels¹⁰⁴: Local repair and exchange of damaged proteins, cytosolic mitochondrial degradation, cell death or competitive removal of cells from tissues, control of mitochondrial subpopulations and rescue via mitochondrial transfer. The named processes are discussed below.

Local repair of mitochondria: Mitochondria often form a large syncytium allowing rapid exchange and diffusion of most mitochondrial content. This buffering capacity of an enlarged mitochondrial network offers an explanation how relatively high loads of pathogenic mutations are managed by individual cells before detrimental effects, usually defects in OXPHOS, affect viability⁸⁰. Mitochondria additionally have a high natural protein turnover, in which case damaged proteins are degraded and newly synthesized or imported from the cytosol¹⁰⁵. For protein degradation separate elaborate systems exist, acting on different mitochondrial compartments and protein types. The serine protease Lon has been studied in detail. It is present in the mitochondrial matrix and acts on soluble matrix proteins. Lon is also capable of binding mtDNA and plays a role in its maintenance¹⁰⁶. Besides degradation of damaged or misfolded proteins, protein refolding is another available repair mechanism, aided by the heat shock proteins Hsp22, Hsp60 and Hsp70¹⁰⁷. These mitochondrial chaperones are upregulated in response to the mitochondrial unfolded protein response, which is activated upon a high load of misfolded proteins inside mitochondria. At the amino acid level, the methionine sulfide reductase

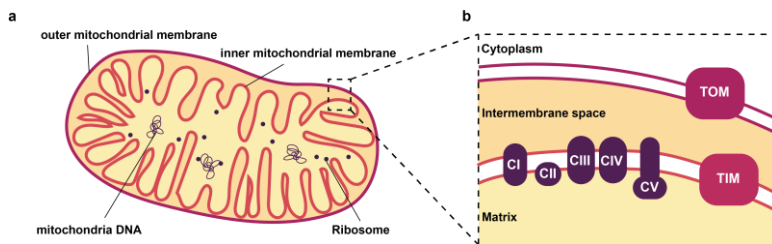


Figure 4: Mitochondrial Structure. **a**, Schematic cross section of a mitochondrion. Mitochondria contain two membranes; the outer mitochondrial membrane isolates the intermembrane space from the cell cytoplasm and the inner mitochondrial membrane delimits the mitochondrial matrix from the intermembrane space. The mitochondrial matrix contains mtDNA and mitochondrial ribosomes. **b**, Enlarged section of inner -and outer mitochondrial membrane. The inner mitochondrial membrane houses the oxidative phosphorylation complexes I-IV (CI-CIV) and the F_1F_0 -ATPase, complex V. Protein translocation into the mitochondrion is organized by the translocase of the outer membrane (TOM) complex and the translocase of the inner membrane (TIM) complex.

system MsrA/MsrB system is facilitating repair of oxidative damage directly by reducing oxidized methionine moieties¹⁰⁸.

Mitochondrial degradation: Mitochondria, can be fully degraded via a type of selective autophagy, mitophagy. Depending on the model system and inducer of mitophagy, several pathways are in place to recruit the autophagic machinery via different cascades of adaptor proteins¹⁰⁹. The best described pathway is induced via PINK1 / Parkin. In healthy mitochondria, PINK1 is imported into mitochondria and degraded. Impaired mitochondria show defects in protein import. Subsequently, PINK1 accumulates on the outer mitochondrial membrane, where it facilitates recruitment of the E3 ubiquitin ligase Parkin. Parkin in turn conjugates ubiquitin to proteins resident on the outer mitochondrial membrane. Ubiquitin then signals recruitment of the autophagosomal machinery¹¹⁰⁻¹¹². The most prominent trigger of this form of mitophagy is loss of membrane potential, providing a means for integration of several possible malfunctions such as a non-functional OXPHOS cascade or a damaged membrane towards the same outcome: mitophagy. In vitro, this pathway is artificially induced via treatment of uncoupling agents like CCCP¹¹³.

Other pathways have been described to act after induction of Ivermectin¹¹⁴, ischemia / glucose deprivation¹¹⁵ or in cancer cells lacking functional parkin expression¹¹⁶. Further, a body of literature hints towards yet another way of degrading parts of mitochondria based on the creation of mitochondria derived vesicles that were shown to directly fuse to late endosomal structures. The content of these vesicles can either be limited to mitochondrial outer membrane structures or can include outer, inner-and matrix components. These vesicles actively bud off of mitochondria in a PINK/Parkin dependent fashion¹¹⁷⁻¹¹⁹. Degradation and selection of mitochondrial content and quality is likely part of the development of multicellular eukaryotes: Competition amongst different mtDNA haplotypes existing within individual cells was shown in mice embryo development¹²⁰ and in the drosophila germline⁹⁶, influenced by genes responsible for mitochondrial fission.

Cell death and removal of cells from tissues: Mitochondrial damage is an inducer of apoptosis in eukaryotic cells¹⁰². Apoptosis is conserved in eukaryotes and centers around the activation of caspases, a certain type of protease¹²¹. The best studied apoptotic pathway activates cytosolic caspases via mitochondria in response to Bak and Bax. Bax is located mostly cytosolic and undergoes constant retrotranslocation from mitochondria to the cytosol, while Bak is a transmembrane protein residing to a large fraction in the outer mitochondrial membrane. Both proteins, when activated by apoptotic stimuli, oligomerize on the outer mitochondrial membrane, causing permeabilization and release of pro-apoptotic factors including cytochrome c¹²². Cytochrome c, once in the cytosol, triggers caspase activity and cell death¹⁰². Since release of mitochondrial material into the cytosol induces cell death, structural integrity of mitochondria is

key for cell survival and excessive mtDNA damage is associated with apoptosis¹²³. Calcium overload and oxidative stress in mitochondria induce formation of the mitochondrial permeability transition pore (MPTP), a nonspecific pore in the inner mitochondrial membrane, resulting in uncoupling of the OXPHOS chain. Formation of the MPTP also induces oligomerization of Bak/Bax on the outer mitochondrial membrane resulting in necrotic cell death¹²⁴⁻¹²⁶. Mitochondria induced apoptosis can be seen as a last resort when cell and mitochondrial damage accumulate. Active selection processes against unfavorable mitochondrial quality may act on an intra-cellular selection process as described above, but also on the level of cell-cell competition: Lima et al. show a possible mechanism for cell selection during murine development. Based on mitochondrial performance, cells are either eliminated via induction of cell apoptosis, or are able to progress¹²⁷.

Control of mitochondrial subpopulations: In eukaryotic cell division, the distribution of organelles to the offspring cells is a directed process. In symmetric cell division, the two daughter cells receive equal mitochondrial quality and amounts. In asymmetric cell division however, several studies show non-uniform organelle segregation in yeast and mammalian cells¹²⁸⁻¹³⁰. Directed inheritance of mitochondrial subpopulations provides another level of quality control. Katajisto et al. showed that mammary stem-like cells partition 'aged' mitochondria and 'young' or newly synthesized mitochondria into different daughter cells. The cell receiving young mitochondria retains stem-like properties while the other cell is more likely to differentiate¹³¹. New mechanisms for directed mitochondrial transport into dedicated daughter cells were elucidated recently¹³².

Cell rescue via mitochondrial transfer: Cell-cell competition and selection and degradation of unfavorable mitochondrial content are important factors in the regulation of mitochondrial quality. Yet, another possible scenario presents itself in multicellular eukaryotes. Cell populations in tissues may drift towards a state in which they cannot revitalize their own mitochondrial pool via cycles of selection, yet cell death is not an option because the cells are needed in order to maintain tissue function. In that case, the only escape might be aid from other cell types maintaining a higher mitochondrial quality. Cytoplasmic transfer between different cell types has been shown to occur *in vivo*¹³³ and several mechanisms for mitochondrial transfer exist such as non-specific uptake, extracellular vesicles or tunneling nanotubes^{91,134,135}. Intercellular mitochondrial exchange has been associated with adipose tissue homeostasis¹³⁶, cancer cell growth¹³⁷ and cell survival after ischemia¹³⁸. These studies show clear phenotype correlations between cytoplasmic mitochondrial uptake and cell behavior; however, mechanistic insights and dose-response relationships are still missing.

Synthetic minimal systems in Symbiogenesis

Symbiogenesis describes the role of endosymbiosis in crucial evolutionary inventions. The term is generally used in connection with Eukaryogenesis or the transition of eukaryotes to photosynthetic organisms¹³⁹. However, there are many other examples for emerging (endo-) symbioses. The boundary conditions for the initiation of symbiogenesis remain highly speculative and are in principle impossible to reenact, which leaves only the study of naturally existing systems in nature^{140,141}. A multitude of host-endosymbiont pairs were found between the eukaryotic and bacterial domain: Plants and nitrogen fixing bacteria show various stages of host-endosymbiont relationships¹⁴², and associations between single celled protists and bacteria are speculated to undergo organellogenesis, the transition from an endosymbiont towards an organelle¹⁴³. The study of endosymbiosis in nature is promoted by new technologies, which manage to retrieve and allocate complex information from either host, endosymbiont or both, for example utilizing ‘omics’ technologies: For instance Smith et al. use transcriptomics to study dynamic responses of both, host and endosymbiont during increasing endosymbiont loads within the symbiotic relationship between aphids and *Buchnera*, providing evidence for joint anabolism of host and symbiont in cobiosynthesis of adenine¹⁴⁴. Nanometer-scale resolution secondary ion mass spectrometry (nano-SIMS) was utilized by Bublitz et al. to unravel protein exchange within the complex endosymbiosis of *Moranella* residing in *Tremblaya* within *Planococcus citri* bacteriocytes, offering high spatial resolution necessary to show exchange of metabolites between host and endosymbiont¹⁴⁵. Research conducted on established endosymbiotic systems provides snapshots of individual evolutionary trajectories. The nature and individual starting points are highly diverse, impeding deduction of common predispositions and circumstances under which two organisms form stable host-endosymbiont mergers. Furthermore, the long timescales in which they develop into stable entities make it challenging to reconstruct individual evolutionary paths. While symbiogenesis itself is seemingly a prevailing evolutionary pattern in eukaryotes, it is unclear whether deeper patterns within the process itself can be reconstituted from individual paths. Metabolite allocation, genome reduction and horizontal gene transfer for instance are common themes that are well described^{77,146}, but mechanistic knowledge is limited.

To provide insights into early symbiogenesis, artificial or synthetic endosymbiotic systems step into the spotlight, aiming to create designer host-endosymbiont pairs. Synthetic biology projects usually try to expand and reinvent systems by building on previously established rules in order to foster and exploit established knowledge (‘What I cannot create, I do not understand’ – R. Feynman). Since there is no set of rules for a defined starting point for the establishment host-endosymbiont pairs, the requirements on synthetic biology are more challenging and fundamental in this case (‘Learning by building’). Nonetheless, fully accessible model systems

provide a promising starting point for the study of symbiogenesis, because all steps required to form stable cell mergers can be monitored and constantly rearranged. Additionally, common patterns of stable endosymbiosis like genome reduction and horizontal gene transfer can be artificially induced, accelerated and engineered. Mehta et al. provide a first possible framework for the development of an artificial endosymbiosis, by introducing engineered *E. coli* bacterial cells into yeast eukaryotic cells¹⁴⁷. However, the promising system leaves important questions regarding stability, growth and metabolite exchange open. The surface of possible pairings for synthetic host-endosymbiont pairs is hardly scratched and provides an open playground for the creation of novel cell mergers.

Aims and outline of this thesis

This work aims to build an experimental platform for the analysis and perturbation of single cells. A special focus lay on expansion of the FluidFM platform by creating new cantilever designs by fine-tuning aperture positions and sizes. To facilitate visualization and readout of the perturbed cells, optical- and computational tools based on confocal spinning disc microscopy were created. The created designs were applied in the background of different biological systems.

In chapter II, we showed that FluidFM cantilevers harboring a cylindrical apex can facilitate enclosed connection to the cytoplasm of various fungi. This allowed direct delivery of molecules via intracellular injection into uni- and multicellular fungi while sustaining cell viability and growth. A fluorescently labelled histone H1, which is actively transported to the nucleus of viable eukaryotic cells, was injected into unicellular *S. cerevisiae* cells and *C. cinerea* hyphae. The fluorescent stain showed accumulation in the cell nucleus. Additionally, we showed extraction of cytoplasm from *C. cinerea* hyphal cells. As a biological proof of principle, nematode feeding on hyphal cells was simulated using cytoplasmic via using FluidFM on a *C. cinerea* reporter strain.

In chapter III, we expanded the FluidFM platform towards the manipulation of organelle structures of mammalian cells. We designed a new set of pyramidal cantilevers harboring enlarged apertures as well as a new type of cantilever containing slanted cylindrical apices. Enlarged apertures increased exerted hydrodynamic forces while limiting steric limitation, which enabled extraction of organelles from cell cytoplasm, while preserving their viability. We establish protocols for the extraction of exclusively endoplasmic reticulum or mitochondria including endoplasmic reticulum. Exerted hydrodynamic flow induced mitochondrial shape transition towards a pearls-on-a-string phenotype, which was independent from calcium signaling. Subsequently, we showed that mitochondria, either isolated using standard protocols or extracted via FluidFM could be transplanted into recipient cultured cells. We followed the uptake behavior of cancer cells and primary keratinocytes of transplanted mitochondria via fluorescence microscopy and found that mitochondria were mostly integrated into the host cell network. Subsequently, the transfer of mitochondrial genomes along with the mitochondrial transplant was quantified; comparing non-specific mitochondrial uptake from the culture medium, injection of mitochondria isolated using standard protocols and mitochondrial transplantation via the cell-to-cell approach.

In chapter IV, protocols for the injection of bacteria into cultured mammalian cells were established. Cytoplasmic growth of fluorescently labelled bacteria was verified and an image analysis platform was written to extract growth speed data of intracellularly growing bacteria.

Furthermore, the impacts of mammalian cell mutant strains affected in amino acid uptake and synthesis as well as nucleotide synthesis on intracellular growth speed of *E. coli* were evaluated.

In chapter V, general conclusions, and future perspectives in relation to this work are discussed.

References

1. Darwin, C. *On the Origin of Species by Means of Natural Selection, or the Preservation of Favoured Races in the Struggle for Life*. (1859).
2. Novick, A. & Szilard, L. Experiments With the Chemostat on Spontaneous Mutations of Bacteria. *Proc. Natl. Acad. Sci* **36**, 708–719 (1950).
3. Griffith, L. G. & Swartz, M. A. Capturing complex 3D tissue physiology in vitro. *Nat. Rev. Mol. Cell Biol.* **7**, 211–224 (2006).
4. Yu, J., Xiao, J., Ren, X., Lao, K. & Xie, X. S. Probing gene expression in live cells, one protein molecule at a time. *Science (80-.)*. **311**, 1600–1603 (2006).
5. Carlo, Dino De & Lee, L. P. Dynamic single cell analysis for Quantitative Biology. *Anal. Chem.* **78**, 7918–7925 (2006).
6. Guillaume-Gentil, O. *et al.* Single-Cell Mass Spectrometry of Metabolites Extracted from Live Cells by Fluidic Force Microscopy. *Anal. Chem.* **89**, 5017–5023 (2017).
7. Actis, P. Sampling from Single Cells. *small* **1700300**, 1–11 (2018).
8. Zhu, H. *et al.* Metabolomic profiling of single enlarged lysosomes. *Nat. Methods* **18**, (2021).
9. Meister, A. *et al.* FluidFM: Combining atomic force microscopy and nanofluidics in a universal liquid delivery system for single cell applications and beyond. *Nano Lett.* **9**, 2501–2507 (2009).
10. Actis, P. Sampling from Single Cells. *Small Methods* **2**, 1700300 (2018).
11. Higgins, S. G. & Stevens, M. M. Extracting the contents of living cells. *Science (80-.)*. **356**, 379–380 (2017).
12. Steffen, F. & Paweletz, N. Erythrocyte Ghost-Mediated Microinjection into cells in monolayer culture: A highly efficient and low toxic technique. *Cell Biol. Int. Reports*, **11**, 5241–5244 (1987).
13. Yasuyuki, K. & Yanagimachi, R. Intracytoplasmic Sperm Injection in the Mouse. *Biol. Reprod.* **52**, 709–720 (1995).
14. Actis, P. *et al.* Compartmental genomics in living cells revealed by single-cell nanobiopsy. *ACS Nano* **8**, 546–553 (2014).
15. Nadappuram, B. P. *et al.* Nanoscale tweezers for single-cell biopsies. *Nat.*

- Nanotechnol.* **14**, 80–88 (2019).
16. Krochev, Y. E., Bashford, C. L., Milovanovic, M., Vodyanoy, I. & Lab, M. J. Scanning ion conductance microscopy of living cells. *Biophys. J.* **73**, 653–658 (1997).
 17. Actis, P. *et al.* Compartmental Genomics in Living Cells Revealed by Single-Cell Nanobiopsy. *ACS Nano* **9**, 1–14 (2010).
 18. Tóth, E. N. *et al.* Single-cell nanobiopsy reveals compartmentalization of mRNAs within neuronal cells. *J. Biol. Chem.* **293**, 4940–4951 (2018).
 19. Singhal, R. *et al.* Multifunctional carbon-nanotube cellular endoscopes. *Nat. Nanotechnol.* **6**, 57–64 (2011).
 20. Wu, T. *et al.* Photothermal Nanoblade for Large Cargo Delivery into Mammalian. *Anal. Chem.* **83**, 1321–1327 (2011).
 21. Wu, T. *et al.* Mitochondrial Transfer by Photothermal Nanoblade Restores Metabolite Profile in Mammalian Cells. *Cell Metab.* **23**, 921–929 (2016).
 22. Cao, Y. *et al.* Nondestructive nanostraw intracellular sampling for longitudinal cell monitoring. *Proc. Natl. Acad. Sci. U. S. A.* **114**, E1866–E1874 (2017).
 23. Wu, Y.-C. *et al.* Massively parallel delivery of large cargo into mammalian cells with light pulses. *Nat Meth* **12**, 439–444 (2015).
 24. Guillaume-Gentil, O. *et al.* Tunable Single-Cell Extraction for Molecular Analyses. *Cell* **166**, 506–517 (2016).
 25. Guillaume-Gentil, O. *et al.* Force-controlled fluidic injection into single cell nuclei. *Small* **9**, 1904–1907 (2013).
 26. G. Binnig, C.F. Quate, C. G. Atomic Force Microscope. *Phys. Rev. Lett.* **56**, 930–934 (1985).
 27. B Drake, CB Prater, AL Weisenhorn, SA Gould, TR Albrecht, CF Quate, DS Cannell, HG Hansma, P. H. Imaging crystals, polymers, and processes in water with the atomic force microscope. *Science (80-)*. **243**, 1586–1589 (1989).
 28. Stiefel, P. *et al.* Cooperative vaccinia infection demonstrated at the single-cell level using FluidFM. *Nano Lett.* **12**, 4219–4227 (2012).
 29. Guillaume-Gentil, O., Zambelli, T. & Vorholt, J. A. Isolation of single mammalian cells from adherent cultures by fluidic force microscopy. *Lab Chip* **14**, 402–414 (2014).
 30. Potthoff, E., Ossola, D., Zambelli, T. & Vorholt, J. A. Bacterial adhesion force quantification by fluidic force microscopy. *Nanoscale* **7**, 4070–4079 (2015).
 31. Potthoff, E. *et al.* Rapid and Serial Quantification of Adhesion Forces of Yeast and Mammalian Cells. *PLoS One* **7**, (2012).

32. Mittelviehhaus, M., Müller, D. B., Zambelli, T. & Vorholt, J. A. A modular atomic force microscopy approach reveals a large range of hydrophobic adhesion forces among bacterial members of the leaf microbiota. *ISME J.* **13**, 1878–1882 (2019).
33. Guillaume-Gentil, O. *et al.* Single-Cell Mass Spectrometry of Metabolites Extracted from Live Cells by Fluidic Force Microscopy. *Anal. Chem.* **89**, 5017–5023 (2017).
34. Martinez, V. *et al.* SU-8 hollow cantilevers for AFM cell adhesion studies. *J. Micromechanics Microengineering* **26**, (2016).
35. Hodges, A. R., Bussmann, K. M. & Hoh, J. H. Improved atomic force microscope cantilever performance by ion beam modification. *Rev. Sci. Instrum.* **72**, 3880–3883 (2001).
36. Burki, F., Roger, A. J., Brown, M. W. & Simpson, A. G. B. The New Tree of Eukaryotes. *Trends Ecol. Evol.* **35**, 43–55 (2020).
37. Smith, M. L., Bruhn, J. N. & Anderson, J. B. The fungus *Armillaria bulbosa* is among the largest and oldest living organisms. *Nature* **356**, 428–431 (1992).
38. Hyde, K. D. *et al.* The amazing potential of fungi: 50 ways we can exploit fungi industrially. *Fungal Divers.* **97**, 1–136 (2019).
39. PJ, Kuhn; APJ, Trinci, MJ, Jung, MW, Goosey, LG, C. *Biochemistry of cell walls and membranes in fungi.* **37**, (1990).
40. Li, D., Tang, Y., Lin, J. & Cai, W. Methods for genetic transformation of filamentous fungi. *Microb. Cell Fact.* **16**, 1–13 (2017).
41. Peberdy, J. F. Fungal protoplasts: isolation, reversion, and fusion. *Annu. Rev. Microbiol.* **33**, 21–39 (1979).
42. Hamlyn, P. F. *et al.* Efficient protoplast isolation from fungi using commercial enzymes. *Enzyme Microb. Technol.* **3**, 321–325 (1981).
43. Hinnen, Albert, JAMES B. HICKS, A. G. R. F. Transformation of yeast. *Spring* **75**, 1929–1933 (1978).
44. Fincham, J. R. S. Transformation in fungi. *Microbiol. Rev.* **53**, 148–170 (1989).
45. Karas, B. J. *et al.* Transferring whole genomes from bacteria to yeast spheroplasts using entire bacterial cells to reduce DNA shearing. *Nat. Protoc.* **9**, 743–750 (2014).
46. Sulo, P., Griač, P., Klobučníková, V. & Kováč, L. A method for the efficient transfer of isolated mitochondria into yeast protoplasts. *Curr. Genet.* **15**, 1–6 (1989).
47. Ito, H., Fukuda, Y., Murata, K. & Kimura, A. Transformation of intact yeast cells treated with alkali cations. *J. Bacteriol.* **153**, 163–168 (1983).
48. Kawai, S., Hashimoto, W. & Murata, K. Transformation of *Saccharomyces cerevisiae* and other fungi: methods and possible underlying mechanism. *Bioeng. Bugs* **1**, 395–403 (2010).

49. Weaver, J. C., Harrison, G. I., Bliss, J. G., Mourant, J. R. & Powell, K. T. Electroporation: High frequency of occurrence of a transient high-permeability state in erythrocytes and intact yeast. *FEBS Lett.* **229**, 30–34 (1988).
50. Kasas, S., Longo, G. & Dietler, G. Mechanical properties of biological specimens explored by atomic force microscopy. *J. Phys. D. Appl. Phys.* **46**, (2013).
51. Touhami, A., Nysten, B. & Dufrène, Y. F. Nanoscale mapping of the elasticity of microbial cells by atomic force microscopy. *Langmuir* **19**, 4539–4543 (2003).
52. Zhao, L. *et al.* Elastic properties of aspergillus nidulans studied with atomic force microscopy. *Biotechnol Prog.* **21**, 292–299 (2005).
53. Partida-Martinez, L. P., Monajembashi, S., Greulich, K. O. & Hertweck, C. Endosymbiont-Dependent Host Reproduction Maintains Bacterial-Fungal Mutualism. *Curr. Biol.* **17**, 773–777 (2007).
54. Riveline, D. & Nurse, P. ‘Injecting’ yeast. *Nat. Methods* **6**, 513–514 (2009).
55. Murley, A. & Nunnari, J. The Emerging Network of Mitochondria-Organelle Contacts. *Mol. Cell* **61**, 648–653 (2016).
56. Schaffer, S. & Suleiman, M. *Mitochondria: the dynamic organelle. Advances in Biochemistry in health and disease* (Springer Science+Business Media, LLC, 2007). doi:10.1007/978-0-387-69945-5
57. Woodson, J. D. & Chory, J. Coordination of gene expression between organellar and nuclear genomes. *Nat. Rev. Genet.* **9**, 383–395 (2008).
58. Satori, C. P. *et al.* Bioanalysis of Eukaryotic Organelles. *Chem. Rev.* **113**, 2733–2811 (2013).
59. Micoulet, A., Spatz, J. P. & Ott, A. Mechanical response analysis and power generation by single-cell stretching. *ChemPhysChem* **6**, 663–670 (2005).
60. Zheng, Y., Nguyen, J., Wei, Y. & Sun, Y. Recent advances in microfluidic techniques for single-cell biophysical characterization. *Lab Chip* **13**, 2464–2483 (2013).
61. Lee, L. M. & Liu, A. P. The application of micropipette aspiration in molecular mechanics of single cells. *J. Nanotechnol. Eng. Med.* **5**, 1–6 (2015).
62. Zhang, H. & Liu, K. K. Optical tweezers for single cells. *J. R. Soc. Interface* **5**, 671–690 (2008).
63. Engler, A. J., Sen, S., Sweeney, H. L. & Discher, D. E. Matrix Elasticity Directs Stem Cell Lineage Specification. *Cell* **126**, 677–689 (2006).
64. Li, J. *et al.* Piezo1 integration of vascular architecture with physiological force. *Nature* **515**, 279–282 (2014).
65. Zhao, Q. *et al.* Structure and mechanogating mechanism of the Piezo1 channel.

- Nature* **554**, 487–492 (2018).
66. Aragona, M. *et al.* Mechanisms of stretch-mediated skin expansion at single-cell resolution. *Nature* **584**, (Springer US, 2020).
 67. Van Bergeijk, P., Adrian, M., Hoogenraad, C. C. & Kapitein, L. C. Optogenetic control of organelle transport and positioning. *Nature* **518**, 111–114 (2015).
 68. Hsieh, C. W., Chu, C. H., Lee, H. M. & Yuan Yang, W. Triggering mitophagy with far-red fluorescent photosensitizers. *Sci. Rep.* **5**, 1–13 (2015).
 69. Wang, Y., Nartiss, Y., Steipe, B., McQuibban, G. A. & Kim, P. K. ROS-induced mitochondrial depolarization initiates PARK2/PARKIN-dependent mitochondrial degradation by autophagy. *Autophagy* **8**, 1462–1476 (2012).
 70. Kasas, S. & Dietler, G. Probing nanomechanical properties from biomolecules to living cells. *Pflugers Arch. Eur. J. Physiol.* **456**, 13–27 (2008).
 71. Pelling, Y. R. S. and A. E. Quantification of Intracellular Mitochondrial Displacements in Response to Nanomechanical Forces. *Methods Mol. Biol.* **991**, 185–192 (2013).
 72. Mishra, P. & Chan, D. C. Mitochondrial dynamics and inheritance during cell division, development and disease. *Nat. Rev. Mol. Cell Biol.* **15**, 634–646 (2014).
 73. Gonzalez-Rodriguez, D. *et al.* Elastocapillary Instability in Mitochondrial Fission. *Phys. Rev. Lett.* **115**, 1–5 (2015).
 74. Mahecic, D. *et al.* Mitochondrial membrane tension governs fission. *Cell Rep.* **35**, (2021).
 75. Helle, S. C. J. *et al.* Mechanical force induces mitochondrial fission. *Elife* **6**, 1–26 (2017).
 76. Buck, M. D. D. *et al.* Mitochondrial Dynamics Controls T Cell Fate through Metabolic Programming. *Cell* **166**, 63–76 (2016).
 77. Ku, C. *et al.* Endosymbiotic origin and differential loss of eukaryotic genes. (2015). doi:10.1038/nature14963
 78. Margulis, L. On the origin of mitosing cells. *J. Theor. Biol.* **14**, 255–74 (1967).
 79. Taanman, J. W. The mitochondrial genome: Structure, transcription, translation and replication. *Biochim. Biophys. Acta - Bioenerg.* **1410**, 103–123 (1999).
 80. Aryaman, J., Johnston, I. G. & Jones, N. S. Mitochondrial heterogeneity. *Front. Genet.* **10**, 1–16 (2019).
 81. Sun, N., Youle, R. J. & Finkel, T. The Mitochondrial Basis of Aging. *Mol. Cell Biol.* **61**, 654–666 (2016).
 82. Kaupilla, T. E. S., Kaupilla, J. H. K. & Larsson, N. G. Mammalian Mitochondria and Aging: An Update. *Cell Metab.* **25**, 57–71 (2017).

83. Archer, S. L. Mitochondrial dynamics - Mitochondrial fission and fusion in human diseases. *N. Engl. J. Med.* **369**, 2236–2251 (2013).
84. Sacconi, S. *et al.* A functionally dominant mitochondrial DNA mutation. **17**, 1814–1820 (2018).
85. Patananan, A. N., Wu, T. H., Chiou, P. Y. & Teitell, M. A. Modifying the Mitochondrial Genome. *Cell Metab.* **23**, 785–796 (2016).
86. Gammage, P. A. *et al.* Genome editing in mitochondria corrects a pathogenic mtDNA mutation in vivo. *Nat. Med.* **24**, 1691–1695 (2018).
87. Bayona-Bafaluy, M. P., Blits, B., Battersby, B. J., Shoubridge, E. A. & Moraes, C. T. Rapid directional shift of mitochondrial DNA heteroplasmy in animal tissues by a mitochondrially targeted restriction endonuclease. *Proc. Natl. Acad. Sci. U. S. A.* **102**, 14392–14397 (2005).
88. Hashimoto, M. *et al.* MitoTALEN: A General Approach to Reduce Mutant mtDNA Loads and Restore Oxidative Phosphorylation Function in Mitochondrial Diseases. *Mol. Ther.* **23**, 1592–1599 (2015).
89. Yang, Y.-W. & Koob, M. D. Transferring isolated mitochondria into tissue culture cells. *Nucleic Acids Res.* **40**, e148 (2012).
90. Yoon, Y. G. & Koob, M. D. Intramitochondrial transfer and engineering of mammalian mitochondrial genomes in yeast. *Mitochondrion* **46**, 15–21 (2019).
91. Clark, M. A. & Shay, J. W. Mitochondrial transformation of mammalian cells. *Nature* **295**, 605–607 (1982).
92. Caicedo, A. *et al.* MitoCeption as a new tool to assess the effects of mesenchymal stem/stromal cell mitochondria on cancer cell metabolism and function. *Sci. Rep.* **5**, 1–10 (2015).
93. Wilkins, H. M., Carl, S. M. & Swerdlow, R. H. Cytoplasmic hybrid (cybrid) cell lines as a practical model for mitochondrialriopathies. *Redox Biol.* **2**, 619–631 (2014).
94. Kenyon, L. & Moraes, C. T. Expanding the functional human mitochondrial DNA database by the establishment of primate xenomitochondrial cybrids. *Proc. Natl. Acad. Sci. U. S. A.* **94**, 9131–9135 (1997).
95. Illmensee, K. & Mahowald, A. P. Transplantation of posterior polar plasm in *Drosophila*. Induction of germ cells at the anterior pole of the egg. *Proc. Natl. Acad. Sci. U. S. A.* **71**, 1016–1020 (1974).
96. Lieber, T., Jeedigunta, S. P., Palozzi, J. M., Lehmann, R. & Hurd, T. R. Mitochondrial fragmentation drives selective removal of deleterious mtDNA in the germline. *Nature* **570**, 380–384 (2019).
97. Cummins, J. M., Wakayama, T. & Yanagimachi, R. Fate of microinjected spermatid

- mitochondria in the mouse oocyte and embryo. *Zygote* **6**, 213–222 (1998).
98. Sercel, A. J. *et al.* Stable transplantation of human mitochondrial DNA by high-throughput, pressurized isolated mitochondrial delivery. *Elife* **10**, 1–45 (2021).
99. Yoon, Y. G. & Koob, M. D. Efficient cloning and engineering of entire mitochondrial genomes in *Escherichia coli* and transfer into transcriptionally active mitochondria. *Nucleic Acids Res.* **31**, 1407–1415 (2003).
100. Yoon, Y. G. & Koob, M. D. Transformation of isolated mammalian mitochondria by bacterial conjugation. *Nucleic Acids Res.* **33**, 1–8 (2005).
101. Brand, M. D. The sites and topology of mitochondrial superoxide production. *Exp. Gerontol.* **45**, 466–472 (2010).
102. Wang, C. & Youle, R. J. The role of mitochondria in apoptosis. *Annu. Rev. Genet.* **43**, 95–118 (2009).
103. Wei, W. *et al.* Germline selection shapes human mitochondrial DNA diversity. *Science (80-.)*. **364**, (2019).
104. Rand, D. M. The units of selection on mitochondrial DNA. *Annu. Rev. Ecol. Syst.* **32**, 415–448 (2001).
105. Chan, X. C. Y., Black, C. M., Lin, A. J., Ping, P. & Lau, E. Mitochondrial protein turnover: Methods to measure turnover rates on a large scale. *J. Mol. Cell. Cardiol.* **78**, 54–61 (2015).
106. Lu, B. *et al.* Roles for the human ATP-dependent Lon protease in mitochondrial DNA maintenance. *J. Biol. Chem.* **282**, 17363–17374 (2007).
107. Fischer, F., Hamann, A. & Osiewacz, H. D. Mitochondrial quality control: An integrated network of pathways. *Trends Biochem. Sci.* **37**, 284–292 (2012).
108. Lee, B. C., Dikiy, A., Kim, H. Y. & Gladyshev, V. N. Functions and evolution of selenoprotein methionine sulfoxide reductases. *Biochim. Biophys. Acta - Gen. Subj.* **1790**, 1471–1477 (2009).
109. Zachari, M. & Ktistakis, N. T. Mammalian Mitophagosome Formation: A Focus on the Early Signals and Steps. *Front. Cell Dev. Biol.* **8**, 1–11 (2020).
110. Youle, R. J. & Narendra, D. P. Mechanisms of mitophagy. *Nat. Rev. Mol. Cell Biol.* **12**, 9–14 (2011).
111. Narendra, D., Tanaka, A., Suen, D. F. & Youle, R. J. Parkin is recruited selectively to impaired mitochondria and promotes their autophagy. *J. Cell Biol.* **183**, 795–803 (2008).
112. Narendra, D. P. *et al.* PINK1 is selectively stabilized on impaired mitochondria to activate Parkin. *PLoS Biol.* **8**, (2010).
113. Ishihara, N., Jofuku, A., Eura, Y. & Mihara, K. Regulation of mitochondrial

- morphology by membrane potential, and DRP1-dependent division and FZO1-dependent fusion reaction in mammalian cells. *Biochem. Biophys. Res. Commun.* **301**, 891–898 (2003).
114. Zachari, M. *et al.* Selective Autophagy of Mitochondria on a Ubiquitin-Endoplasmic-Reticulum Platform. *Dev. Cell* **50**, 627-643.e5 (2019).
115. Saito, T. *et al.* An alternative mitophagy pathway mediated by Rab9 protects the heart against ischemia. *J. Clin. Invest.* **129**, 802–819 (2019).
116. Villa, E., Marchetti, S. & Ricci, J. E. No Parkin Zone: Mitophagy without Parkin. *Trends Cell Biol.* **28**, 882–895 (2018).
117. McLelland, G. L., Soubannier, V., Chen, C. X., McBride, H. M. & Fon, E. A. Parkin and PINK1 function in a vesicular trafficking pathway regulating mitochondrial quality control. *EMBO J.* **33**, 282–295 (2014).
118. Sugiura, A., McLelland, G., Fon, E. A. & McBride, H. M. A new pathway for mitochondrial quality control: mitochondrial-derived vesicles. *EMBO J.* **33**, 2142–2156 (2014).
119. Soubannier, V. *et al.* A vesicular transport pathway shuttles cargo from mitochondria to lysosomes. *Curr. Biol.* **22**, 135–141 (2012).
120. Latorre-Pellicer, A. *et al.* Regulation of Mother-to-Offspring Transmission of mtDNA Heteroplasmy. *Cell Metab.* **30**, 1120-1130.e5 (2019).
121. Salvesen, G. S. & Dixit, V. M. Caspases: Intracellular Minireview Signaling by Proteolysis of the protein, sometimes in inactivation, but never in degradation since their substrate specificity distinguishes the caspases as among the most restricted of. *Cell* **91**, 443–446 (1997).
122. Kluck, R. M., Bossy-Wetzel, E., Green, D. R. & Newmeyer, D. D. The release of cytochrome c from mitochondria: A primary site for Bcl-2 regulation of apoptosis. *Science (80-.)*. **275**, 1132–1136 (1997).
123. Kim, J. *et al.* Mitochondrial DNA damage is involved in apoptosis caused by pro-inflammatory cytokines in human OA chondrocytes. *Osteoarthr. Cartil.* **18**, 424–432 (2010).
124. Narita, M. *et al.* Bax interacts with the permeability transition pore to induce permeability transition and cytochrome c release in isolated mitochondria. *Proc. Natl. Acad. Sci. U. S. A.* **95**, 14681–14686 (1998).
125. Karch, J. *et al.* Bax and Bak function as the outer membrane component of the mitochondrial permeability pore in regulating necrotic cell death in mice. *Elife* **2**, 1–21 (2013).
126. Halestrap, A. P. What is the mitochondrial permeability transition pore? *J. Mol. Cell.*

- Cardiol.* **46**, 821–831 (2009).
127. Lima, A. *et al.* Cell competition acts as a purifying selection to eliminate cells with mitochondrial defects during early mouse development. *Nat. Metab.* (2021). doi:10.1038/s42255-021-00422-7
 128. Lai, C. Y., Jaruga, E., Borghouts, C. & Michal Jazwinski, S. A mutation in the ATP2 gene abrogates the age asymmetry between mother and daughter cells of the yeast *Saccharomyces cerevisiae*. *Genetics* **162**, 73–87 (2002).
 129. Rivolta, M. N. & Holley, M. C. Asymmetric segregation of mitochondria and mortalin correlates with the multi-lineage potential of inner ear sensory cell progenitors in vitro. *Dev. Brain Res.* **133**, 49–56 (2002).
 130. Ouellet, J. & Barral, Y. Organelle segregation during mitosis: Lessons from asymmetrically dividing cells. *J. Cell Biol.* **196**, 305–313 (2012).
 131. Katajisto, P. *et al.* Asymmetric apportioning of aged mitochondria between daughter cells is required for stemness. *Science (80-.)*. **348**, 340–343 (2015).
 132. Moore, A. S. *et al.* Actin cables and comet tails organize mitochondrial networks in mitosis. *Nature* **591**, (Springer US, 2021).
 133. Santos-Ferreira, T. *et al.* Retinal transplantation of photoreceptors results in donor-host cytoplasmic exchange. *Nat. Commun.* **7**, 1–7 (2016).
 134. Rustom, A., Saffrich, R., Markovic, I., Walther, P. & Gerdes, H. H. Nanotubular Highways for Intercellular Organelle Transport. *Science (80-.)*. **303**, 1007–1010 (2004).
 135. Liu, D. *et al.* Intercellular mitochondrial transfer as a means of tissue revitalization. *Signal Transduct. Target. Ther.* **6**, (2021).
 136. Brestoff, J. R. *et al.* Intercellular Mitochondria Transfer to Macrophages Regulates White Adipose Tissue Homeostasis and Is Impaired in Obesity. *Cell Metab.* **33**, 270-282.e8 (2021).
 137. Chang, J. C. *et al.* Mitochondrial transplantation regulates antitumour activity, chemoresistance and mitochondrial dynamics in breast cancer. *J. Exp. Clin. Cancer Res.* **38**, 1–16 (2019).
 138. Hayakawa, K. *et al.* Transfer of mitochondria from astrocytes to neurons after stroke. *Nature* **535**, 551–555 (2016).
 139. Aanen, D. K. & Eggleton, P. Symbiogenesis: Beyond the endosymbiosis theory? *J. Theor. Biol.* **434**, 99–103 (2017).
 140. Martin, W. F., Garg, S., Zimorski, V. & Martin, W. F. Endosymbiotic theories for eukaryote origin. (2015).
 141. Williams, T. a, Foster, P. G., Cox, C. J. & Embley, T. M. An archaeal origin of

- eukaryotes supports only two primary domains of life. *Nature* **504**, 231–6 (2013).
142. Kneip, C., Lockhart, P., Voß, C. & Maier, U. G. Nitrogen fixation in eukaryotes - New models for symbiosis. *BMC Evol. Biol.* **7**, 1–12 (2007).
143. Marin, B., Nowack, E. C. M. & Melkonian, M. A Plastid in the Making : Evidence for a Second Primary Endosymbiosis. **156**, 425–432 (2005).
144. Smith, T. E. & Moran, N. A. Coordination of host and symbiont gene expression reveals a metabolic tug-of-war between aphids and Buchnera. *Proc. Natl. Acad. Sci. U. S. A.* **117**, 2113–2121 (2020).
145. Bublitz, D. A. C. *et al.* Peptidoglycan Production by an Insect-Bacterial Mosaic. *Cell* **179**, 703-712.e7 (2019).
146. Wernegreen, J. J. Genome evolution in bacterial endosymbionts of insects. *Nat. Rev. Genet.* **3**, 850–861 (2002).
147. Mehta, A. P. *et al.* Engineering yeast endosymbionts as a step toward the evolution of mitochondria. *Proc. Natl. Acad. Sci.* **115**, 11796–11801 (2018).
148. Guillaume-Gentil, O. *et al.* Force-controlled manipulation of single cells: From AFM to FluidFM. *Trends Biotechnol.* **32**, 381–388 (2014).

II Injection into and extraction from single fungal cells

Orane Guillaume-Gentil,^{1*} Christoph G. Gäbelein,¹ Stefanie Schmieder,^{1,3} Vincent Martinez,² Tomaso Zambelli,² Markus Künzler,¹ Julia A. Vorholt^{1*}

¹Institute of Microbiology, ETH Zurich, 8093 Zurich, Switzerland; ²Institute for Biomedical Engineering, ETH Zurich, 8092 Zurich, Switzerland

³current address: Division of Gastroenterology, Boston Children's Hospital, Boston MA 02115

*Correspondence: gorane@ethz.ch, jvorholt@ethz.ch

Abstract

The direct delivery of molecules and the sampling of endogenous compounds into and from living cells provide powerful means to modulate and study cellular functions. Intracellular injection and extraction remain challenging for fungal cells that possess a cell wall. The most common methods for intracellular delivery into fungi rely on the initial degradation of the cell wall to generate protoplasts, a step that represents a major bottleneck in terms of time, efficiency, standardization, and cell viability. Here, we show that fluidic force microscopy enables the injection of solutions and cytoplasmic fluid extraction into and out of individual fungal cells, including unicellular model yeasts and multicellular filamentous fungi. The approach is strain- and cargo-independent and opens new opportunities for manipulating and analyzing fungi. We also perturb individual hyphal compartments within intact mycelial networks to study the cellular response at the single cell level.

Introduction

Fungi play pivotal ecological and economical roles in nature, agriculture, medicine, and for industrial applications, from the degradation of dead organic material to their beneficial role in plant growth and the production of many drugs and food products.¹⁻⁵ In addition, numerous plant and animal pathogenic fungi are known, many of which are difficult to combat.⁶ They are also important model organisms in biological research to study the molecular biology of eukaryotes. The manipulation of fungi is thus crucial to deepen our understanding of fungal biology in general and to optimize their use in agriculture and bioproduction. However, in practice, the development of such manipulation techniques faces many obstacles. These are mainly due their complex cell wall structure, acting as a physical barrier, and to the enormous diversity of fungal species and thus the difficulty in developing universally applicable protocols.

A crucial aspect in fungal cell biology is the ability to deliver exogenous materials into living cells e.g. of DNA for transformation. Other cargos of interest include RNA, proteins, peptides, and small (anti) metabolites, as well as synthetic nanomaterials such as quantum dots or nanoparticles.⁷⁻⁹ While effective delivery methods are available for animal cells, introducing exogenous materials into fungal cells has proven challenging, especially for filamentous fungi.⁷ Bulk transformation approaches include protoplast-mediated or *Agrobacterium tumefaciens*-mediated transformation, electroporation, biolistics, and shock waves. However, most of these approaches show relatively poor efficiency.¹ Although fungal protoplasts are most widely used for transformation, cell wall removal requires dedicated protocols for each fungal species because they differ in cell wall composition and structure, and remains a challenge for most fungi. In addition, the formation of protoplast leads to a dramatic decrease in cell viability.¹

A promising alternative for efficient intracellular delivery relies on the use of nanopipettes to directly access the interior of an individual cell.¹⁰ As a general concept, a fluidic nanoprobe is inserted into a cell to create a channel across the cell membrane, and molecules loaded in the probe are released into the cell. The approach also allows molecules to be captured from the cell into the nanoprobe. Thus, these technologies not only provide a straightforward universal approach for intracellular delivery, but also enable the sampling of endogenous molecules, offering a powerful means of analysing animal cells.¹¹ Fluidic force microscopy (FluidFM) has shown a great potential in this area. The FluidFM technology is a force-sensitive nanopipette that enables pressure-driven fluid handling in the femto- to pico-litre range.^{12, 13} We have previously demonstrated FluidFM-based injection of exogenous molecules into mammalian cells,¹⁴ as well as the extraction of cytoplasmic or nuclear biopsies from living cells for molecular analyses.^{15, 16}

However, the use of nanopipettes with fungi has shown only limited success so far, mostly hindered by the high rigidity of the cell wall, the difficulty to immobilizing the cell to prevent its lateral displacement during manipulation, as well as their relatively small cell size.¹⁷ Riveline *et al.* trapped *Schizosaccharomyces pombe* in microstructures, and shear-damaged their cell wall locally while releasing solution with the same pipette, which resulted in some of the solution reaching the cell interior.¹⁸

Here, we introduce a quantitative FluidFM-based method for injection into and extraction from fungi, including filamentous fungi and unicellular yeasts, that is widely applicable (Figure 1a).

Results

Technological developments

Fungi are characterized by a large diversity of life forms. In order to establish a broadly applicable platform for their manipulation, we selected four model organisms that cover their main distinctive morphological features: the unicellular fungi *Saccharomyces cerevisiae* and *Schizosaccharomyces pombe*, which are the two major models for budding and fission yeasts, respectively; the dimorphic yeast *Candida albicans*, an opportunistic pathogen that can switch from a unicellular budding growth to a multicellular mycelial growth under specific environmental conditions; and *Coprinopsis cinerea*, a multicellular filamentous fungus and model organism for studying fungal development and the evolution of multicellular fungi. *S. cerevisiae*, *S. pombe* and *C. albicans* belong to the phylum Ascomycota whereas *C. cinerea* is a representative of the phylum Basidiomycota of the kingdom Fungi.¹⁹

The general workflow for injecting or extracting fluid into and from living cells using FluidFM consists of the following steps: 1) positioning the pyramidal FluidFM tip above a selected cell; 2) driving the tip through the cell wall and membrane using force spectroscopy; 3) maintaining the tip in the cell at a constant force while applying over- or underpressure for injection or extraction, respectively; 4) withdrawing the tip from the cell. (Supplementary Figure 1) This approach works reliably with mammalian cells.¹⁴ However, it is not readily applicable to fungal cells due to their unique physical properties, particularly the rigid cell wall.

The insertion of the FluidFM tip into a cell requires that the cell is immobilized on a hard substrate. While most animal cells spread and adhere to solid substrates, the adhesion of fungal cells is comparatively weak.²⁰⁻²² Therefore, we first evaluated whether fungal cells maintained a fixed position upon indentation as a prerequisite for injection. On flat substrates, the spherical

yeast *S. cerevisiae* and the rod-shaped yeast *S. pombe* were laterally displaced upon contact with the FluidFM tip. We therefore designed microstructured substrates and could show that the yeast cells were spatially constrained (see Methods for a description of the microstructured substrates). In contrast, the hyphae of the dimorphic yeast *C. albicans* and of the filamentous fungi *C. cinerea* adhered sufficiently on glass and plastic polystyrene, respectively, to prevent cell displacement upon tip insertion.

Furthermore, the cell wall surrounding fungal cells results in a drastically increased cell rigidity, causing an increase in the forces required to insert a probe into the cells compared to animal cells. The high stiffnesses of fungal cells were reflected in the force-distance curves obtained by indentation and eventual insertion of the probe inside fungal and animal cells (Figure 1b). For effective probe insertion into a typical adherent mammalian cell (e.g. HeLa), the maximal force was set such that the tip crossed the entire cell to the underlying substrate, which typically required forces up to 200 nN.¹⁴ In comparison, the force-distance curves on fungal cells showed that, while the indentation distances were similar or shorter than for HeLa cells, the forces required for maximal indentation were 10 times larger, i.e. up to 2 μ N. FluidFM probes were thus re-designed, optimizing their length and thickness to increase their stiffness to $\sim 2.3 \pm 0.5$ N/m, so that forces up to several micro-Newtons could be exerted.

Finally, cell size also represents a crucial aspect for the development of an injection protocol for fungal cells. It determines the upper injectable volumes, especially due to the cell wall, which provides a physical barrier to cell expansion. We estimated the cell volumes of the four selected fungi, in comparison to human HeLa cells (Figure 1c). The mean (SD) cell volumes of the yeasts *C. albicans*, *S. pombe* and *S. cerevisiae* were 75 (50), 105 (25) and 80 (55) fL, respectively. The average volume of hyphal compartments of the mushroom *C. cinerea* was 360 (290) fL. In comparison, HeLa cells had a mean volume of 2500 (950) fL, approximately ten- to thirtyfold larger. Because the volumes injected into animal cells were typically on the order of hundreds of femtoliters,¹⁴ we anticipated that volumes injectable into fungal cells will be on the order of tens of femtoliters. Cell size is also relevant in the context of proper probe insertion, as the probe aperture must be sufficiently narrow and close to the pyramid apex to be fully within the cell just upon puncturing. Yet, at the same time, the aperture area should be large enough for sufficient flow. We thus shaped probe apertures with focused ion beam embracing two of the four sides of the tip, with aperture sizes down to 200 nm in height and width (Figure 1d).

Fluorescent tracer injection

To assess the ability to cross the cell wall and inject solutions into fungal cells and to adjust the injection parameters, we first used the membrane-impermeable fluorescent tracer Lucifer

yellow (LY). We performed force spectroscopy on the fungal cells and subsequently monitored LY fluorescence in real time during and after applying a pressure difference of +1000 mbar for several minutes. Using a fluorescent probe allowed detection of both cell staining resulting from a successful injection and extracellular leakage in the event of a compromised tip insertion (Supplementary Figure 2). Consistent with the force-distance curves (Figure 1b), the application of a force of $2.0 \pm 0.1 \mu\text{N}$ resulted in 100% successful injection of the dye into fungal cells without apparent leakage (N=9), indicating full insertion of the probe aperture into the cell (Figure 2). Of note, when we tested the injection with lower forces, i.e. $1.0 \pm 0.1 \mu\text{N}$ and $1.5 \pm 0.1 \mu\text{N}$, this resulted in intracellular staining, but with concomitant leakage of the fluorophore into the extracellular environment in 100% of the cases (N=11), and 83 % (N=18), respectively. The simultaneous release of LY both inside the cell and in the extracellular environment indicated effective cell wall pervasion but incomplete insertion of the probe aperture. With applied forces lower than $1.0 \pm 0.1 \mu\text{N}$, the cell wall was not pierced, and the fluorophore was released entirely in the extracellular medium. These results highlight the need to apply sufficient force for robust injection into fungal cells, which we achieve with $2 \mu\text{N}$ and represents an important step from earlier studies.¹⁸

Following injection, the unicellular yeasts *S. pombe* and *S. cerevisiae* were uniformly labeled, whereas neighboring yeasts remained unlabeled (Figure 2a and 2b). Although homogenous staining may also result from extracellular binding of the fluorophore to the cell wall, the selective labeling of the targeted but not the neighboring yeasts indicated successful delivery of the fluorophore inside the cell.

Unequivocal intracellular targeting of the fluorophore was achieved by injection of hyphal and pseudohyphal cells of *C. albicans* (Figure 2c). While single cells of the dimorphic yeast are similar in size to *S. pombe* and *S. cerevisiae* (see Figure 1c), *C. albicans* forms multicellular structures under certain environmental conditions. Upon injection of hyphal germ tubes, a homogenous staining of the entire structure was observed, as expected. In fact, germ tubes are hyphal projections that develop in the first cell cycle, before septation. When injecting hyphal compartments, the released fluorophore selectively stained the targeted compartments and did not cross the mature septa. In addition, injection of pseudo-hyphae resulted in labelling of some but not all compartments, in agreement with the dye passing through primary but not mature septa. In addition, vacuoles in the injected compartments remained unlabeled, validating the cytoplasmic location of the injected fluorescent tracer.

Similarly, in *C. cinerea* mycelia, the injected fluorophore dispersed throughout the targeted hyphal compartments, included their branches, but did not pass through the septa delimiting the cells, indicating effective intracellular injection (Figure 2d). The intracellular delivery of LY was

further validated by injecting vacuolated hyphal compartments, whereby the injected dye clearly located in the cytoplasmic fluid and was excluded from the vacuoles (Figure 2d, right panels).

Next, we estimated the volumes of solution that we injected based on the fluorescence intensities of the injected cells. The volumes were similar for the four organisms and ranged between 1 and 100 femtoliters (Supplementary Figure 3). We note here that eventual extracellular staining of the cell wall may result in additional fluorescence and the injected volumes may thus be slightly overestimated. For comparison, volumes up to 900 fL were injected in HeLa cells.¹⁴ The estimated injected volumes were thus consistent with the respective sizes of fungal and animal cells described above.

Regarding the pressure pulse applied to release the fluorophore solution in the cell, we applied a pressure difference up to more than 1000 mbar, during several minutes. In mammalian cells, such pressure pulses resulted in injection volumes larger than 1 pL, which led to inflation, membrane rupture and cell death. In the fungal cells, no cell deformation was observed, consistent with the rigid cell wall maintaining cell shape and the high internal pressure of the cells.

Post-injection cell viability

The results described above showed that injection into fungal cells is indeed feasible. The next set of experiments was aimed to assess whether the method preserves cell viability. We therefore monitored the growth of the fungi following injection. In addition, we used a fluorescently-labeled histone H1 (H1-AF488) injected into *S. cerevisiae* and *C. cinerea*. When the exogenous nuclear protein is delivered into the cell, it is expected to be actively transported to the nucleus in fully functional cells.

In the unicellular *S. cerevisiae*, the injected histone protein effectively accumulated in the nuclei, while a diffuse fluorescence signal was observed in the cytoplasm and cell wall; moreover, the fluorescent protein was excluded from vacuoles (Figure 3a). After injection of a budding mother cell, the labeled histone was transported into the nucleus of the mother and the daughter cells, with a lower fluorescence intensity in the daughter cell (Figure 3b). Monitoring of the injected yeasts by time-lapse microscopy showed that the injected cells were moving, and continued to produce a daughter cell in the hours following injection (Figure 3c). After the budding event, the labelled histone was observed in both nuclei of the mother and daughter cells (Figure 3d).

Similarly, in the filamentous fungi *C. cinerea*, the injected histone proteins were effectively transported into the nuclei, while slightly labeling the walls of the cells (Figure 4a). The homokaryon strain of *C. cinerea* most frequently contains two nuclei per hyphal segment.²³ Consistent with this, we mostly observed the staining of two nuclei per injected hyphal compartments, with a weaker stain for the nucleus most distant from the injection site (Figure 4a). Vegetative mycelia of *C. cinerea* grow by apical extension of hyphae and the formation of subapical branches, each of which becomes an apically elongating hypha. To evaluate post-injection growth, we injected hyphal tip cells and subsequently monitored them by time-lapse microscopy (Figure 4b). Apical growth was observed for all injected hyphal tip cells, with a similar elongation rate as for non-injected hyphae. Upon mycelial growth, the injected H1-AF488 remained in its location and observable for at least 2 days.

The observation that the injected histone protein accumulated in nuclei not only validated the successful intracellular injections, in both uni- and multicellular fungi, but also demonstrated the short-term preservation of cellular functions. Further monitoring of fungal growth after injection confirmed the absence of significant adverse effect on cell viability.

Extraction

Next, we evaluated the ability to extract cellular fluid from fungal cells. We used an oil-filled FluidFM probe to allow confinement and visualization of cytoplasmic fluid extracted into the probe. Tip insertion into *C. cinerea* hyphal compartments was performed as for injection, but instead of applying overpressure, we applied underpressure for the suction of the cell content. When exerting underpressure, we effectively observed the collection of fluid in the cantilever probe (Figure 5a, inserts). When targeting a hyphal tip cell, continued growth of the hypha was observed after tip insertion, but stopped after aspiration of the cytoplasmic fluid into the probe (Figure 5a, blue arrows). The extraction was accompanied by the appearance of vacuoles in the targeted hyphal compartment. No morphological changes were observed in the adjacent hyphal compartments (Figure 5a). These observations indicated successful extraction of cytoplasmic fluid.

Examining single cells within a multicellular fungus

After demonstrating extraction from individual hyphal cells, we applied this method to address an open question in *C. cinerea* research. The filamentous fungus represents a prey for fungivorous nematodes, such as *Aphelenchus avenae*.²⁴ It has been shown that *A. avenae* feeds

on *C. cinerea* by perforation of the cell wall with its stylet and suction of the cellular fluid.²⁵ This attack in turn triggers a defense response of *C. cinerea* that involves the expression of the defense gene *cgl2*.^{25, 26} Previous results suggest that the physical cue of penetration and suction is necessary to trigger *cgl2* expression but it remained unclear whether it is sufficient or whether chemical cues, such as the concomitant release of molecules by the fungivorous nematode, are needed.²⁷ We hypothesized that extraction with the FluidFM could mimic nematode feeding and thus, allow us to test whether hyphal content removal is sufficient to induce the fungal defense response. To address this question, we used a reporter strain of *C. cinerea* carrying a dTomato expression cassette driven by the promoter of the *cgl2* gene.²⁵ Volumes ranging from 210 fL up to 1750 fL were extracted from different hyphal compartments, and the mycelia was then monitored overnight for the expression of the fluorescent reporter. Time-lapse fluorescence microscopy after extraction showed an increasing dTomato signal, selectively in the hyphal compartments that had been extracted (Figure 5b). Quantitative measurements of the fluorescent reporter confirmed a steady increase of the reporter fluorescence over time within hyphal compartments that had been extracted, whereas neighboring cells, which did not undergo extraction, did not express the fluorescent reporter (Figure 5c). This suggests that the suction of cytoplasm was sufficient to induce a defense response in *C. cinerea*. As pointed out above, we had observed that single hyphal cell extraction resulted in growth arrest. It is thus interesting to note that the cells remained viable and maintained the capacity to express the fluorescent reporter protein, despite the important loss of cytoplasmic fluid. A previous study revealed that upon localized challenge with nematodes, the fungal defense response was generally confined to the site of predation, but it propagated over several millimeters in a distinct subset of specialized hyphae, characterized by a large diameter.²⁵ While such “trunk” hyphae were not targeted in the present study, the FluidFM extraction approach will provide an attractive tool to investigate the propagation of the fungal defense response at the single-cell resolution.

Discussion

The method developed in this work allows traversing the cell wall of living fungi with a nano-fluidic probe and either delivering a solution into individual fungal cells or extracting cytoplasmic fluid. It provides a straightforward universal technique for intracellular delivery that is adapted to virtually any natural or synthetic molecules that can be dispersed in solution as well as to the diversity of fungal species. We demonstrated proof-of-concept delivery of a fluorescent dye and a labeled protein into uni- and multi-cellular fungi, and further showed sustained cell viability and growth after the injection. Numerous applications are conceivable in which the

injected cargo enables either monitoring or interfering a particular endogenous molecular process in living single cells or multicellular networks. A relatively large cell-to-cell variation in the injected volumes was observed, similar to what has been reported for injections into mammalian cells.^{14,31} The determination of the volumes injected can thus only be achieved post-injection, using fluorescence measurements. If the molecule of interest has no fluorescence, it can be co-injected together with a fluorescent marker. In contrast to mammalian cells, direct injection into fungi nuclei was not possible, as those are too small for insertion of the FluidFM tip. In addition to intracellular delivery, the method also enables extraction of cytoplasmic fluid from single fungal cells. In this work, we applied this technique to mimic nematode feeding and study the fungal defense response to this predation. This proof-of-concept study illustrates the ability to manipulate and analyze hyphal cells within intact mycelial networks at single-cell resolution, opening new avenues for studying cell-cell communication and organization in filamentous fungi. Furthermore, with emergent developments in bioanalytics, it will also be possible to use the approach to analyze the molecular content of individual fungal cells, similar to studies emerging for mammalian cells.¹¹

Methods

Fungi strains and media

Yeast extract-peptone-dextrose (YPD) medium was prepared with 1 % (w/v) yeast extract (Oxoid), 2 % (w/v) bacto peptone (BD) and 2 % (w/v) glucose (Sigma). Yeast maltose and glucose (YMG) medium was prepared with 0.4 % (w/v) yeast extract (Oxoid), 1.0 % (w/v) malt extract, and 0.4 % (w/v) glucose (Sigma). Defined synthetic dextrose (SD) medium was prepared with 0.19 % (w/v) yeast nitrogen base without amino acids and ammonium sulfate (ForMedium), 0.082 % (w/v) complete supplement mixture of amino acids (ForMedium), and 2 % (w/v) glucose (Sigma). Phosphate-buffered saline (PBS) was prepared with 0.8 % (w/v) NaCl (Merck), 0.02 % (w/v) KCl (Sigma), 0.144 % (w/v) Na₂HPO₄ (Sigma) and 0.024 % (w/v) KH₂PO₄ (Sigma), adjusted to pH 7.4.

Wild-type *Schizosaccharomyces pombe* and *Saccharomyces cerevisiae* (W303) were grown in YPD medium. For injection experiments, 5 mL cultures were grown overnight at 180 rpm and a temperature of 28 °C. A 100 µL of the cell suspension was seeded onto the microstructured substrates. For initial experiments (fluorophore injection), 5 mL of PBS were added. For later experiments (cell viability), 5 mL of SD medium were added. The cells were let sediment onto the substrate for at least 15 minutes.

Wild-type *Candida albicans* (SC5314) were grown in YPD medium. For injection experiments, 5 mL cultures were grown overnight at 180 rpm and a temperature of 28°C. To

induce yeast-to-hyphal transition, 1 mL of the cell suspension was then resuspended in 4 mL PBS and supplemented with 1 mL foetal bovine serum (Chemie Brunschwig AG). The cells were then cultured for about 5 hours at 37 °C and 180 rpm. 500 µL of the cell suspension was then seeded onto a 50 mm glass bottom dish (low side wall, WillCo Well B.V.) and 5 mL PBS were added.

Vegetative mycelia of *Coprinopsis cinerea* wildtype strain (A43mutB43mut; homodikaryon) and of the reporter strain A43mutB43mut cgl2p-dTom (expression of cytoplasmic dTomato under control of cgl2p) were cultivated on YMG agar plates at 37 °C in the dark. Samples for injection and extraction experiments were prepared as follow: a plug was inoculated onto the cover (~low side wall) of a 50mm-petri dish. 2 mL of YMG liquid medium were added and the fungi were let grown at 37 °C in the dark for 4 to 5 days. Fresh medium was added every 1-2 days. Shortly prior to the experiment, 4 mL low-fluorescence SD medium was added to the dish.

Reagents for injection

HEPES-2 buffer was prepared with 4-(2-hydroxyethyl) piperazine-1-ethanesulfonic acid (HEPES, 10 mM), supplemented with sodium chloride (150 mM) in Millipore water, with a pH adjusted to 7.4 using NaOH (6 M). Lucifer Yellow CH dipotassium salt (LY, Sigma-Aldrich Chemie GmbH), and Alexa488-labeled histone H1 (Invitrogen) were used at concentrations ranging from 0.5 to 2.0 mg/mL in HEPES-2 buffer. All solutions were filtered through 0.2 µm pore size filters before use.

Micro-structured substrates

Atomic force microscopy studies (AFM) of microorganisms require their immobilization on the substrates, otherwise they roll away as soon as the AFM tip enters in contact with their cell wall.^{28, 29} Immobilization strategies were pioneered by the Dufrêne's group taking advantage of porous polymer membranes.³⁰ For this study, we designed substrates with micro-structures of different lateral and height dimensions and assayed their efficacy for the immobilization of unicellular yeasts upon indentation with a FluidFM probe. The micro-structured substrates were produced by Wunderlichips GmbH, and were made of Kraton A1536 polymer, with the microstructures laying on a 40 ± 5 µm thick bottom layer. Successful immobilization of *S. cerevisiae* was obtained with circular and oval micro-wells, with a depth of 5 µm, and lateral dimensions ranging from 5 to 12 µm. Successful immobilization of *S. pombe* was obtained using trenches or rectangle micro-wells, with a depth of 3µm, a width of 4 to 5 µm, and a length of 12 µm or longer. 1 cm × 1 cm arrays of microstructures were laid on a drop of 100 % ethanol onto

a 50mm glass bottom dish (Willco Well B.V.). The overall thickness of the sample allowed the use of objectives with high numerical apertures.

Optical microscopy

We used an inverted AxioObserver microscope equipped with a temperature-controlled incubation chamber (Zeiss), and coupled to a spinning disc confocal microscope (Visitron) with a Yokogawa CSU-W1 confocal unit and an EMCCD camera system (Andor). Phase-contrast and fluorescence images were acquired using 10×, 40× (0.6 na), and 63× (1.4 na, oil) objectives and a 2× lens switcher using VisiView software (Visitron).

Lucifer yellow CH and Alexa Fluor 488-Histone H1 were imaged using a 488 nm laser and a 525/50 emission filter. The dTomato fluorescent reporter was imaged using a 561 nm laser and a 609/54 nm emission filter.

Microscopy images were analyzed using the AxioVision and Fiji softwares. When indicated (Figure caption), fluorescence images were created by summing the slices of a Z-stack (maximum intensity projection) in Fiji.

FluidFM setup

We used a FluidFM system composed of a FlexAFM-NIR scan head and a C3000 controller driven by the EasyScan2 software (Nanosurf), and a digital pressure controller unit (ranging from -800 to + 1000 mbar) operated by a digital controller software (Cytosurge). A syringe pressure kit with a three-way valve (Cytosurge) was used in addition to the digital pressure controller to apply larger pressure differences.

FluidFM Rapid Prototyping probes made of silicon nitride were obtained from Cytosurge. The probes were coated with an 18 nm carbon layer using a CCU-010 Carbon Coater (Safematic), and the aperture was milled using a FIB-SEM Nvision 40 device (Zeiss) equipped with a gallium ion source using the Atlas software (Zeiss). The front face of the pyramidal probe was aligned perpendicularly to the FIB-beam, and the aperture, extending on two faces of the pyramidal tip, was milled (see figure 1d) with an acceleration voltage of 30 kV at 10 pA (100 nm thick silicon nitride layer at the aperture region). The processed probes were then mounted onto a cytoclip holder by Cytosurge.

For experiments with *S. cerevisiae*, *S. pombe*, and *C. cinerea*, the FluidFM probes were plasma treated for 1 min (PDG-32G, Harrick Plasma) and coated with the hydrophobic, anti-fouling SL2 Sigmacote (Sigma-Aldrich) on the inside and outside with heat stabilization for \geq 45 min at 100 °C prior to use (see ¹⁵ for a detailed protocol), before filling the probe with the solution to inject.

For experiment with *C. albicans*, the probes were filled with the solution to inject, and then coated with hydrophilic, anti-fouling polymer as follows: the probes were plasma treated for 1

min (PDG-32G, Harrick Plasma), and subsequently immersed for at least 45 minutes in a solution of poly(L-lysine)-graft-(polyethylene glycol) (PLL-*g*-PEG, with a PLL backbone chain of 20 kDa, 2 kDa PEG side chains and a grafting ratio of 3.5, obtained from SurfaceSolutionS GmbH) at 0.5 mg/mL in Millipore water. The probe was then immersed for at least 5 minutes in Millipore water for rinsing. was obtained from; the non-fouling polymer was used in Millipore water (0.5 mg mL⁻¹).

Estimation of fungal cell volumes

All cell dimensions were measured in the AxioVision software, using brightfield images acquired with a 40× objective. HeLa cells were dissociated by trypsinization before imaging.

The cell volumes were calculated from the measured cell diameters, assuming a spherical shape for HeLa cells and *S. cerevisiae*, and from the measured length and width, assuming a tubular shape for *S. pombe* and for the hyphal compartments of *C. albicans* and *C. cinerea*.

Injection experiments

Cantilever spring constant was measured using a software-implemented calibration module (Nanosurf), with the resonance frequencies and quality factors obtained from thermal noise spectrum acquired in air, before filling of the probe microchannel. The solution to inject was loaded in the probe reservoir, and the probe was then connected to the pressure controller unit

to apply an overpressure Δp of 1000 mbar to flow the solution from the reservoir into the microchannel. The cantilever sensitivity was then calibrated in the sample experimental medium (PBS or SD medium).

The cell to be injected was visualized by phase contrast microscopy, and the FluidFM probe was approached on the substrate in the vicinity of the targeted cell with a force set point of 20 nN and retracted with the Z-piezo. The probe was then laterally displaced above the desired point of insertion, under observation by phase contrast microscopy. The tip of the probe was then inserted into the cell through a forward force spectroscopy routine driven by the Z-piezo with a velocity of 1000 nm s⁻¹. The forward force spectroscopy was set to stop when reaching a maximal force (F_{max}) of up to 2000 nN. The probe was then maintained in the cell interior at constant F_{max} for 1 up to 30 min. During this pause, an overpressure pulse Δp of 1000 mbar or higher was applied to deliver the solution. The probe was then retracted through a backward force spectroscopy with a velocity of 1000 nm s⁻¹. The entire injection process was monitored by phase contrast and fluorescence microscopy, and force spectroscopy. All injection experiments were conducted in low-fluorescence media. The initial experiments with the injection of LY were performed in PBS, at room temperature. To allow for viability assessment, the later experiments with the injection of AF488-H1 were performed in rich SD medium, at 30 °C for *S. cerevisiae*, and at 28 °C or 37 °C for *C. cinerea*.

Quantification of the injected volumes

Fluorescence images acquired through a 40× objective were analyzed in Fiji. A sample region of interest (ROI) and a non-overlapping background ROI were defined, and their area and mean fluorescence intensity were measured. The total fluorescence intensity was calculated by multiplying the sample area by the mean fluorescence intensity of the sample to which the mean fluorescence intensity of the background was subtracted. The obtained total fluorescence intensities were normed to an exposure time of 1 s.

A calibration curve to define the fluorescence intensity per volume was obtained by measuring the total fluorescence intensities of areas of different sizes of the FluidFM cantilever probe, with a known channel height of 800 nm. The fluorescent intensities were plotted against their respective volume, and the amount of fluorescence for a given volume was then obtained by linear regression.

For injected cells, the net fluorescence was obtained by subtracting the total fluorescence intensity before the injection from the one after injection.

Extraction

The reporter strain A43mutB43mut *cgl2p*-dTom, which expresses cytoplasmic dTomato under control of the *cgl2* gene promoter, was used. The probes were coated with Sigmacote (see above). Following spring constant calibration ($k = 2.3 \pm 0.5$ N/m), the microchannel of the FluidFM probe was filled with mineral oil by application of overpressure. The probe was then immersed in the SD medium, and the probe sensitivity was calibrated ($\beta = 66 \pm 3$ nm/V). A hyphal cell was selected under the optical microscope, and the probe was positioned next to the cell for conducting a force-controlled approach in contact-mode and retraction to 9 μm above the substrate. The tip of the probe was then moved above the hyphal cell and AFM force spectroscopy was initiated with a preset force of 2000 nN at 1.0 $\mu\text{m/s}$. Once inserted, the tip was maintained inside the cell by maintaining a constant force for 10 to 20 min. Maximum underpressure was applied to extract cytoplasmic fluid into the probe. The pressure was then switched back to zero, and the probe was retracted out of the cell. Extraction experiments were conducted at room temperature (24 ± 1 °C).

Quantification of *cgl2p*-dTomato expression

Following the extractions ($N = 5$), the area of the mycelium that comprised the extracted hyphal compartments was monitored at room temperature (24 ± 1 °C) with a 10x objective and a 2x lens, in brightfield and with the 561 laser for the dTomato reporter. Z-stacks (200 slices, 300 nm) were acquired at 120 min intervals during 18 h. For each time-point, an image was created by summing the slices of the acquired dTomato Z-stacks in Fiji. dTomato fluorescence

intensities were then measured as described above (Quantification of the injected volumes). Boundaries of individual hyphal compartments and backgrounds were all manually defined, and background intensities were measured for each time point and subtracted from all intensity values. We analyzed 5 extracted and 5 unperturbed hyphal compartments.

Acknowledgments

This work was supported by a grant from the Volkswagen foundation (Initiative "Life") to J.A.V., a European Research Council Advanced Grant (no. 883077) to J.A.V., and the Swiss National Science Foundation (Grant No. 31003A_173097) to M.K.

Author contributions

O.G., T.Z., M.K., and J.A.V. designed the study. O.G., V.M., and S.S. designed, performed and analyzed the experiments. C.G.G. designed and manufactured the FluidFM-probes. O.G. and J.A.V. wrote the manuscript with input from all authors.

Competing interests

The authors declare no competing interests.

References

1. Hyde, K.D. et al. The amazing potential of fungi: 50 ways we can exploit fungi industrially. *Fungal Diversity* 97, 1-136 (2019).
2. Manganyi, M.C. & Ateba, C.N. Untapped Potentials of Endophytic Fungi: A Review of Novel Bioactive Compounds with Biological Applications. *Microorganisms* 8 (2020).
3. Hossain, M.M., Sultana, F. & Islam, S. in Plant-Microbe Interactions in Agro-Ecological Perspectives: Volume 2: Microbial Interactions and Agro-Ecological Impacts. (eds. D.P. Singh, H.B. Singh & R. Prabha) 135-191 (Springer Singapore, Singapore; 2017).
4. Tedersoo, L., Bahram, M. & Zobel, M. How mycorrhizal associations drive plant population and community biology. *Science* 367 (2020).
5. Kiers, E.T. et al. Reciprocal rewards stabilize cooperation in the mycorrhizal symbiosis. *Science* 333, 880-882 (2011).
6. Fisher, M.C. et al. Emerging fungal threats to animal, plant and ecosystem health. *Nature* 484, 186-194 (2012).
7. Li, D., Tang, Y., Lin, J. & Cai, W. Methods for genetic transformation of filamentous fungi. *Microbial Cell Factories* 16, 168 (2017).
8. Rivera, A.L., Magana-Ortiz, D., Gomez-Lim, M., Fernandez, F. & Loske, A.M. Physical methods for genetic transformation of fungi and yeast. *Phys Life Rev* 11, 184-203 (2014).
9. Stewart, M.P., Langer, R. & Jensen, K.F. Intracellular Delivery by Membrane Disruption: Mechanisms, Strategies, and Concepts. *Chem Rev* 118, 7409-7531 (2018).
10. Chau, C., Actis, P. & Hewitt, E. Methods for protein delivery into cells: from current approaches to future perspectives. *Biochem Soc Trans* 48, 357-365 (2020).
11. Higgins, S.G. & Stevens, M.M. Extracting the contents of living cells. *Science* 356, 379-380 (2017).
12. Meister, A. et al. FluidFM: combining atomic force microscopy and nanofluidics in a universal liquid delivery system for single cell applications and beyond. *Nano Lett* 9, 2501-2507 (2009).
13. Guillaume-Gentil, O. et al. Force-controlled manipulation of single cells: from AFM to FluidFM. *Trends Biotechnol* 32, 381-388 (2014).
14. Guillaume-Gentil, O. et al. Force-controlled fluidic injection into single cell nuclei. *Small* 9, 1904-1907 (2013).

15. Guillaume-Gentil, O. et al. Tunable Single-Cell Extraction for Molecular Analyses. *Cell* 166, 506-516 (2016).
16. Guillaume-Gentil, O. et al. Single-Cell Mass Spectrometry of Metabolites Extracted from Live Cells by Fluidic Force Microscopy. *Anal Chem* 89, 5017-5023 (2017).
17. Shen, Y. et al. Single Cell Injection using Nano Pipette via Nanorobotic Manipulation System inside E-SEM. *2009 9th Ieee Conference on Nanotechnology (Ieee-Nano)*, 518-521 (2009).
18. Riveline, D. & Nurse, P. 'Injecting' yeast. *Nature Methods* 6, 513-514 (2009).
19. Spatafora, J.W. et al. The Fungal Tree of Life: from Molecular Systematics to Genome-Scale Phylogenies. *Microbiol Spectr* 5 (2017).
20. Potthoff, E. et al. Rapid and serial quantification of adhesion forces of yeast and Mammalian cells. *PLoS One* 7, e52712 (2012).
21. El-Kirat-Chatel, S. & Dufrêne, Y.F. Nanoscale adhesion forces between the fungal pathogen *Candida albicans* and macrophages. *Nanoscale Horizons* 1, 69-74 (2016).
22. Sancho, A., Vandersmissen, I., Craps, S., Lutun, A. & Groll, J. A new strategy to measure intercellular adhesion forces in mature cell-cell contacts. *Sci Rep* 7, 46152 (2017).
23. Kues, U. Life history and developmental processes in the basidiomycete *Coprinus cinereus*. *Microbiol Mol Biol Rev* 64, 316-353 (2000).
24. Tayyrov, A., Stanley, C.E., Azevedo, S. & Kunzler, M. Combining microfluidics and RNA-sequencing to assess the inducible defensome of a mushroom against nematodes. *BMC Genomics* 20, 243 (2019).
25. Schmieder, S.S. et al. Bidirectional Propagation of Signals and Nutrients in Fungal Networks via Specialized Hyphae. *Curr Biol* 29, 217-228 e214 (2019).
26. Bleuler-Martinez, S. et al. A lectin-mediated resistance of higher fungi against predators and parasites. *Mol Ecol* 20, 3056-3070 (2011).
27. Plaza, D.F., Schmieder, S.S., Lipzen, A., Lindquist, E. & Kunzler, M. Identification of a Novel Nematotoxic Protein by Challenging the Model Mushroom *Coprinopsis cinerea* with a Fungivorous Nematode. *G3 (Bethesda)* 6, 87-98 (2015).
28. Dufrêne, Y.F. Towards nanomicrobiology using atomic force microscopy. *Nature Reviews Microbiology* 6, 674-680 (2008).
29. Dufrêne, Y.F. Atomic force microscopy in microbiology: new structural and functional insights into the microbial cell surface. *mBio* 5, e01363-01314 (2014).
30. Dufrêne, Y.F., Boonaert, C.J., Gerin, P.A., Asther, M. & Rouxhet, P.G. Direct probing of the surface ultrastructure and molecular interactions of dormant and

germinating spores of *Phanerochaete chrysosporium*. *J Bacteriol* 181, 5350-5354 (1999).

31. Minaschek, G. et al. Quantitation of the volume of liquid injected into cells by means of pressure. *Exp Cell Res* 183 (2), 434-442 (1989).

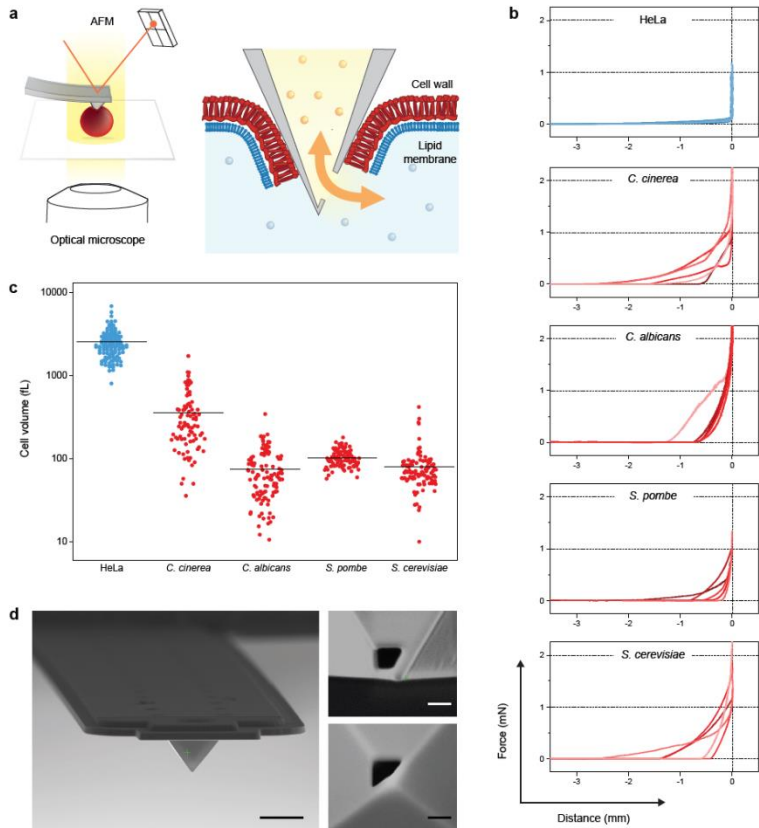


Figure 1. Technological developments. a) Scheme of FluidFM-based injection/extraction of fungi. A microfluidic probe operated with an atomic force microscope (AFM) is inserted through the hard cell wall, allowing for a pressure-driven exchange of liquids between the probe microchannel and the cell interior. The FluidFM is mounted on an optical microscope that allows *in situ* monitoring of the manipulation. b) Representative force-distance curves obtained upon probe insertion in the different organisms. Each plot features 5 curves recorded with different cells. c) Estimated cell volumes, as measured from 2D microscopy images assuming tubular and spherical cell geometries, for (dissociated) HeLa cells (N=132), *C. cinerea* (N=88), *C. albicans* hyphal compartments (N=116), *S. pombe* (N=100) and *S. cerevisiae* (N=105). d) Scanning electron microscopy images of FluidFM probes with a custom-designed tip aperture for fungal injection. Left: Front view of the hollow cantilever with a pyramidal tip. Scale bar: 5 μm . Right: side- (top) and bottom- (down) views of the aperture on the pyramidal tip. Scale bars: 200 nm.

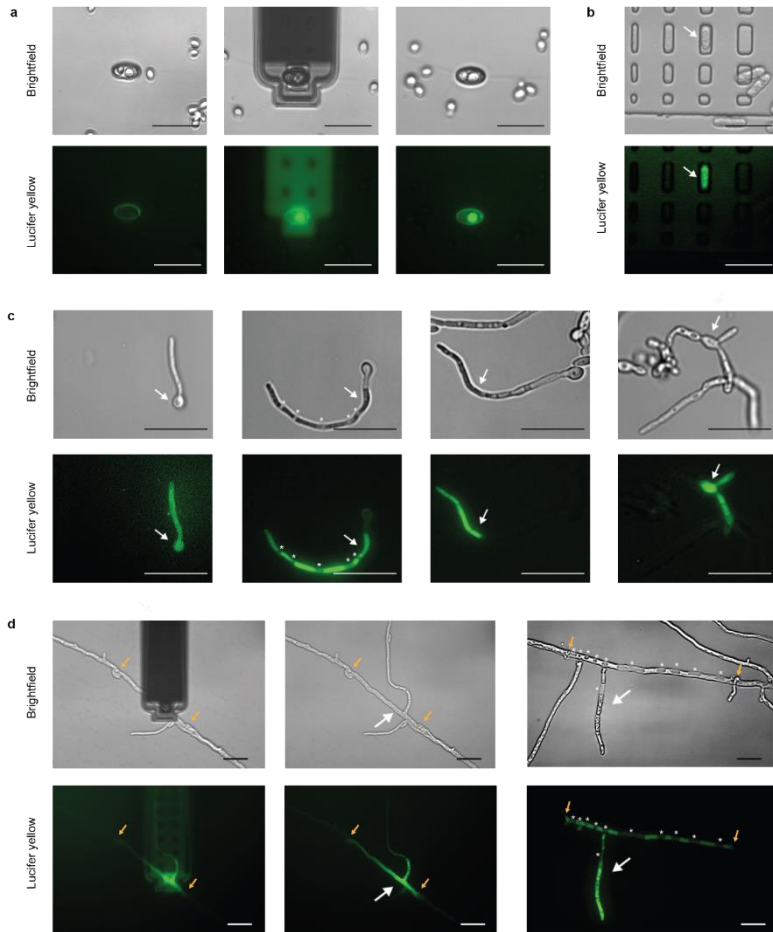


Figure 2. Fluorophore injection. a) Brightfield and fluorescence images of lucifer yellow (LY) injection in *S. cerevisiae*, before, during, and after the injection. The images show a single oval microwell (in the center) containing two yeasts; the right yeast in the microwell was injected and got labeled, whereas the neighboring yeast on its left was not injected and remained unlabeled. b) *S. pombe* injected with LY. c) Germ tube (left), hyphae (center left, center right), and pseudo-hyphae (right) of *C. albicans* injected with LY. d) LY injections in *C. cinerea* hyphal compartments. The white arrows in b), c), and d) indicate the injection sites. The asterisks in c) and d) indicate the vacuoles. The orange arrows in d) indicate the septa of the injected hyphal compartment. Scale bars are 20 μ m.

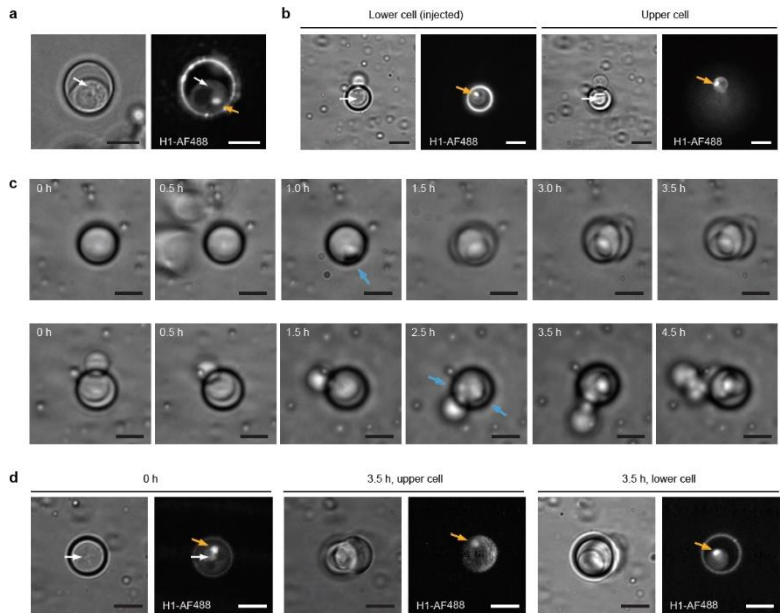


Figure 3. Post-injection viability of *S. cerevisiae*. a) H1-AF488 injected in *S. cerevisiae* accumulated in the cell nucleus (orange arrow), and was excluded from the vacuole (darker). The white arrow shows the injection site. b) Following injection of a budding *S. cerevisiae* (lower cell), the labelled histone accumulated in both the lower and the upper cell nuclei (orange arrows). The white arrows show the injection site. c) Time-lapse brightfield images of *S. cerevisiae* after injection. The first row shows the growth post-injection of a single yeast. Budding was observed 1 h after the injection (blue arrow), and 2 cells were then observed on the following time frames. The second row shows the growth of a yeast that was budding at the time of injection (same cell as in b). The injected yeast continued its growth, budding ~2.5 h after injection (blue arrows), and resulting in 4 cells at later time frames. d) After division of an injected single cell, the labelled histone was found in the nuclei of both the mother and the daughter cells. The white arrows show the injection site, the orange arrows show the labelled nuclei. All the images were created by summing the slices of a Z-stack. Scale bar: 5 μm .

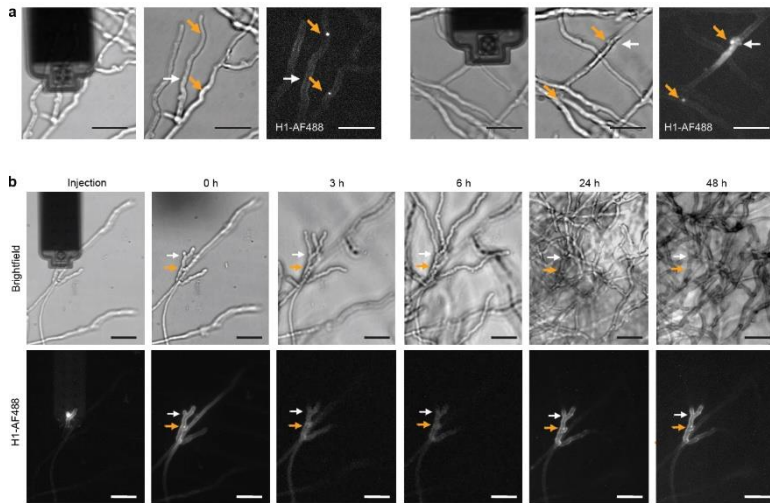


Figure 4. Post-injection viability of *C. cinerea*. a) H1-AF488 injected in *C. cinerea* accumulated in the cell nuclei (orange arrows). Two representative injections are shown. The white arrow shows the injection sites. b) Following injection of a hyphal tip, time-lapse monitoring showed the growth of the injected cell, similar to the surrounding hyphae. The injected H1-AF488 remained at its location along the whole time-course. The fluorescence images in a), and the brightfield and fluorescence images at 0, 24, and 48 h in b) are summed slices of Z-stacks. Scale bar: 20 μm .

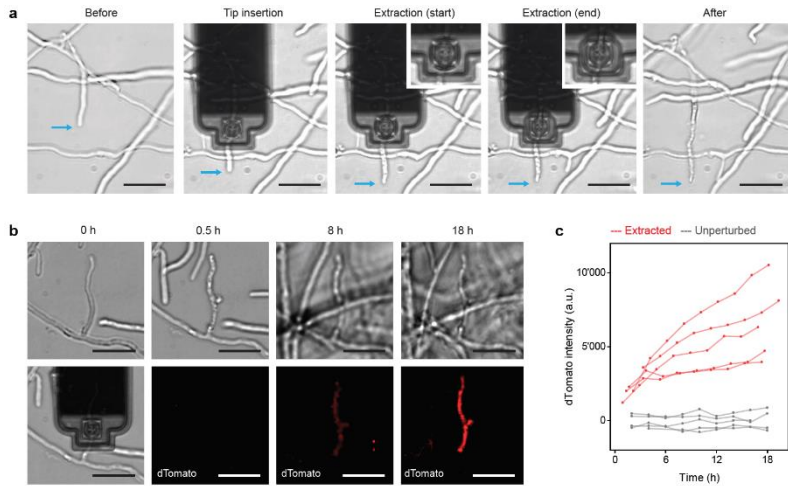


Figure 5. Cytoplasmic fluid extraction from *C. cinerea*. a) Brightfield images showing the extraction of cytoplasmic fluid from *C. cinerea*. Upon application of suction, the cellular fluid is collected in the front of the FluidFM probe (inserts). The targeted hyphae was growing until suction was applied for extraction (blue arrows). Vacuoles are visible after the extraction, exclusively within the targeted compartment. b) Extraction (0 h) and subsequent monitoring of the dTomato fluorescent reporter. c) Quantified dTomato fluorescence intensity of individual hyphal compartments over time after extraction. Red curves profiles were obtained from extracted hyphal compartments (N=5). Grey curves are dTomato expression profile from control, non-perturbed hyphal compartments within the same mycelia (N=5). Scale bars: 20 μ m.

Supplementary Information

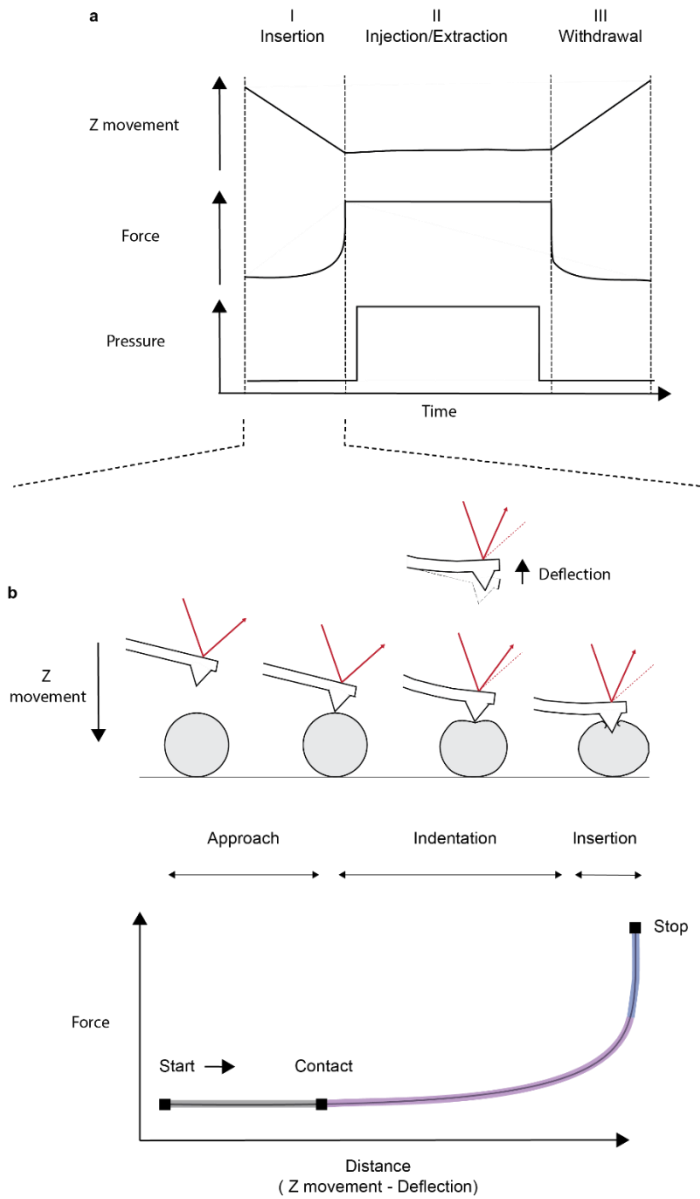
Injection into and extraction from single fungal cells

Orane Guillaume-Gentil,^{1*} Christoph G. Gäbelein,¹ Stefanie Schmieder,^{1,3} Vincent Martinez,² Tomaso Zambelli,² Markus Künzler,¹ Julia A. Vorholt^{1*}

¹Institute of Microbiology, ETH Zurich, 8093 Zurich, Switzerland; ²Institute for Biomedical Engineering, ETH Zurich, 8092 Zurich, Switzerland

³current address: Division of Gastroenterology, Boston Children's Hospital, Boston MA 02115

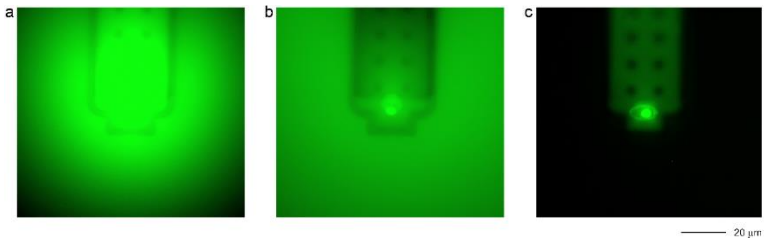
*Correspondence: gorane@ethz.ch, jvorholt@ethz.ch



Supplementary Figure 1. Automated force spectroscopy approach for injection and extraction of fungi.

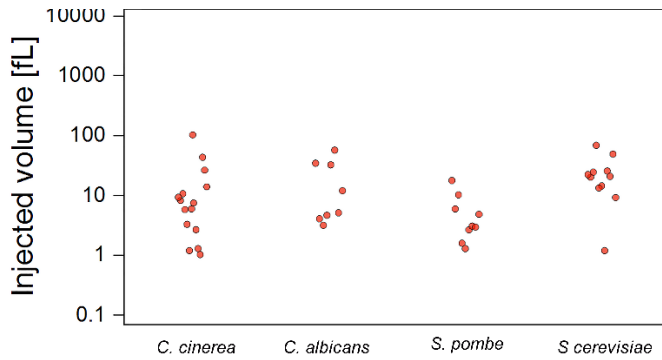
a) The routine consists in 3 successive phases. In the first phase, the probe is first driven down at constant speed (1000 nm s^{-1}) while the force sensed at the tip is recorded; the probe movement is stopped when a pre-defined force set-point is reached (maximal force, up to 2000 nN); no pressure is applied through the microchannel; phase I lasts less than 10 s. In the second phase, the force is kept constant at the pre-set maximal force, and vertical movement of the probe allows for compensating eventual drifts; shortly after stabilization of the tip inside the cell, a positive pressure difference is applied through the microchannel for injection; injection is stopped by switching the pressure back to zero; this second phase lasts several minutes. In the third phase, the probe is withdrawn out of the cell at constant speed; the force is recorded, and no pressure is applied; the phase lasts less than 10 s.

b) Probe insertion. Force-Distance profiles are obtained from phase I, in which the measured force is plotted against the Z-movement of the probe (down) to which the probe deflection (up) is subtracted. When the probe is driven towards the selected cell, the force sensed by the tip is zero until it contacts the cell; the force then start to gradually increase as the tip is pushed further down, indenting the cell; pushing further down, the tip crosses through the cell wall and membrane. The cell wall rupture events are not detected, due to the high stiffness of the probe.



Supplementary Figure 2. *In situ* fluorescence imaging upon injection of *S. cerevisiae*.

Extracellular leakage of the fluorophore is readily observed in cases where the probe aperture is not inserted (a), or only partially inserted (b) in the cell interior. Upon complete insertion of the probe aperture inside the cell, cell staining but no leakage are observed (c).



Supplementary Figure 3. Injected volumes as measured from intracellular fluorescence of Lucifer yellow in *C. cinerea* (N=15), *C. albicans* (N=8), *S. pombe* (N=9) and *S. cerevisiae* (N=11).

III Mitochondria transplantation between living cells

Christoph G. Gäbelein¹, Qian Feng², Edin Sarajlic³, Tomaso Zambelli⁴, Orane Guillaume-Gentil¹,
Benoît Kornmann^{2,5}, Julia A. Vorholt^{1*}

¹Institute of Microbiology, ETH Zurich, 8093 Zurich, Switzerland

²Institute of Biochemistry, ETH Zurich, 8093 Zurich, Switzerland

³SmartTip BV, 7500 AH Enschede, The Netherlands

⁴Institute for Biomedical Engineering, ETH Zurich, 8092 Zurich, Switzerland.

⁵Department of Biochemistry, University of Oxford, Oxford OX1 3QU, United Kingdom

*e-mail: jvorholt@ethz.ch

Abstract

Mitochondria and the complex endomembrane system are hallmarks of eukaryotic cells. To date, it has been difficult to manipulate organelle structures within single live cells. We developed a FluidFM-based approach to extract, inject and transplant organelles directly from and into living cells with subcellular spatial resolution. The approach enabled the transfer of controlled quantities of mitochondria into cells while maintaining their viability and monitoring their fate in new host cells. Transplantation of healthy and drug-impaired mitochondria into primary keratinocytes allowed real-time tracking of mitochondrial subpopulation rescue. Fusion with the mitochondrial network of recipient cells occurred as early as 20 min after transplantation and continued for over 16 hours. After transfer of mitochondria into somatic cells and cell propagation over generations, we show that donor mtDNA was replicated in recipient cells without the need for selection pressure. The approach opens new prospects for the study of organelle physiology and homeostasis, but also for mechanobiology, synthetic biology, and therapy.

Introduction

Single-cell surgery approaches promise minimally invasive perturbation, i.e. removal or introduction of cellular compartments without compromising cell viability. Manipulation of mitochondria receives special emphasis due to their central cellular role: they are at the heart of energy conversion and link cellular metabolism to signaling pathways and cell fate decision¹. Mitochondria harbor their own genetic content (mtDNA), which is prone to accumulating erroneous, disease causing mutations²⁻⁴ and are subject to quality control^{5,6}. Although mitochondria are generally inherited strictly vertically to daughter cells, exchange of larger cellular components including mitochondria has also been observed in tissues of multicellular organisms⁷⁻¹⁰. To reconstitute such transfer events, therapy approaches involve the grafting of purified mitochondria into a damaged area of a tissue or their intravenous injection¹¹. However the fate of these mitochondria is unknown¹².

With limited means to study and quantify the transfer of mitochondria into cells and without ways to analyze dose-response relationships experimentally, it is difficult to gain mechanistic insight on the actual impact of cytoplasmic and mitochondrial transmissions under healthy or diseased cellular states. Extraction and injection of organelles from and into single cells is technically demanding. Miniaturized probes have a high potential to manipulate and sample individual cells within their microenvironment at high spatiotemporal resolution¹³. Nano-scaled pipettes and nanotweezers allow sampling and trapping of individual charged molecules and single mitochondria^{14,15} and have been combined with -omics methods, enabling compartment-resolved single cell studies^{16,17}. Other specialized microfluidic devices for microinjection into cultured cells have been introduced¹⁸. Using a modified microcapillary pipet, mitochondria injection was achieved¹⁹. However, the success rate of transferring mitochondria into single cultured cells has been low and requires use of cells artificially depleted of mtDNA with subsequent selection of transformed cells. This limits the approach to selective conditions and, in particular, it has prevented studies on the dynamic behavior of mitochondrial subpopulations to this point.

Despite all these crucial developments in single-cell technologies, functional transfer, i.e. transplantation of organelles from cell to cell, has not yet been achieved with exception of much larger oocytes.

FluidFM²⁰ unites the high-precision force-regulated approach of an atomic force microscope (AFM, pN to μ N) with the volumetric dispensing of nano-scale pipets (fL to pL) under optical inspection, providing the forces and volume control relevant for single-cell manipulation²¹. These features are pivotal for driving the probe into the cytosolic compartment in a minimally invasive manner when delivering and extracting molecules (including plasmids, RNAs, and

proteins) into- and from viable cells^{22,23}. In this study, we established FluidFM as a single-cell technology for intra- and intercellular micromanipulation of organelles in living eukaryotic cells (Fig. 1a-c). The fluidic handling of subcellular compartments poses a challenge for miniaturized probes because endomembrane structures are relatively large (mitochondria: 300-800 nm in diameter²⁴) and form interconnected networks. Organelle manipulation also bears a higher risk of rupturing the cytoplasmic membrane compared to the few nm opening of probes used for molecule injection and extraction in prior work^{22,23}. Organelle extraction and injection achieved here required dedicated fabrication of tips with customized aperture area (A), to both overcome steric constraints and increase the range of applicable suction forces (F_{max}) at the aperture via the fluidic pressure (Δp) in accordance to $F_{max} = \Delta p \times A$. We adapted the size and geometry of the aperture and microchannel of the FluidFM probes, and used the tips in combination with force control for membrane insertion via automated AFM and exertion of suction (i.e. tensile) forces via automated pressure controller. We simultaneously inspected target cells and the transplant inside the transparent cantilever (via phase contrast and fluorescence microscopy, Supplementary Fig. 1). We demonstrate the establishment of a robust and maximally efficient method for the extraction of mitochondria from living cells and for functional transplantation between individual cells. The gentle mode of probe insertion and extraction ensures cell viability and allows monitoring of mitochondrial dynamics in real time and across cell generations, and tracking mitochondrial variants and fate in native cells.

Results

Tunable organelle extraction from live cells

To enable organelle manipulations, in particular their unconstrained flow through the probe, we manufactured FluidFM-probes with a channel height of 1.7 μm and drilled apertures up to 1100 nm \times 1100 nm ($A = 1.2 \mu\text{m}^2$) with focused ion beam (FIB) (Fig. 1b). In addition, we designed and fabricated dedicated probes with a cylindrical tip to facilitate minimally invasive cell entry. These were sharpened by FIB milling to resemble a hollow needle to facilitate membrane insertion (Fig. 1b, Supplementary Fig. 1). These probes had an aperture area of $A = 1.6 \mu\text{m}^2$, further minimizing steric limitations and increasing the range of applicable hydrodynamic forces spanning from a few pN to over 100 nN, while showing great robustness towards mechanical stress (Supplementary Fig. 2). The general workflow for the manipulation of intracellular membrane enclosed compartments involves positioning the FluidFM probe above a selected subcellular location and their insertion by AFM force spectroscopy, followed by either extraction of material from the cell by exerting negative pressure (Fig. 1a) or injection into the cell by positive pressure (Fig. 1c). Exclusion of large organelles is achieved by fine-tuning the aperture size (A) and the strength of the applied negative pressure ($-\Delta p$). The extraction of cytoplasmic material is monitored in real time and the extract is inspected inside the FluidFM channel by optical microscopy after relieving the pressure ($\Delta p = 0$) and retracting the probe (Fig. 2a and b, right). The sampled material can be dispensed subsequently for downstream analyses or transplanted directly into a recipient cell (Fig. 1a). To examine the capabilities of the newly fabricated FluidFM probes for organelle sampling from single cells, we monitored the endoplasmic reticulum (ER) and mitochondria. We used human osteosarcoma epithelial (U2OS) cells and visualized in parallel the ER by expression of GFP fused to the resident protein Sec61 β (sec61-GFP) and mitochondria by expression of BFP targeted to the mitochondrial matrix (su9-BFP). When utilizing pyramidal probes with an aperture size of $A = 0.5 \mu\text{m}^2$ and low pressure offsets, $\Delta p < 20$ mbar, we accumulated ER in the cantilever, which was accompanied by disappearance of GFP-signal in the cell (Fig. 2a). During extraction, the ER was pulled towards the cantilever tip and we observed a general conversion of cisternal to tubular ER, in both U2OS cells and a similarly labelled kidney cell line (COS7, Supplementary Fig. 3, Supplementary Movies 1 and 2). Notably, under these conditions, the mitochondrial network remained unperturbed and mitochondria were not extracted.

Next, we aimed at extracting mitochondria using pyramidal probes with a larger aperture size ($A = 1.2 \mu\text{m}^2$) and newly developed, slanted cylindrical probes ($A = 1.6 \mu\text{m}^2$) (Fig. 1b). Tunable extraction of mitochondria was achieved using both kinds of probes, thus enabling aspiration of individual mitochondria or sampling of larger quantities of the mitochondrial

network (Fig. 2b, c; Supplementary Movies 3 and 4). Monitoring mitochondrial extraction, we noticed that mitochondrial tubules exposed to tensile forces (negative pressure) underwent a shape transition reminiscent of a ‘pearls-on-a-string phenotype’²⁵ inside the cytoplasm of the target cells. This phenotype was characterized by discrete spheres of mitochondrial matrix, connected by thin and elongated membrane stretches (Fig. 2d). These globular structures eventually pinched off upon further exertion of a pulling force and resulted in spherical shaped mitochondria in the cantilever (Fig. 2b, c).

Because mitochondria changed shape upon extraction and the integrity of mitochondria is a key requirement to ensure functionality, we investigated whether both mitochondrial membranes remained intact during the process. To this aim, we used U2OS cells and performed time-lapse microscopy during extraction of mitochondria in which both the matrix (su9-BFP) and the outer mitochondrial membrane (Fis1TM-mCherry) were labelled. Consistent with the observations described above (Fig. 2b, c), we observed the morphological change of mitochondrial tubules exclusively under direct fluid flow at the cantilever aperture and thus exertion of tensile forces, but not upon probe insertion without fluid flow (Fig. 2d, e, Supplementary Movie 4 and 5). Our data further show that the force-induced shape transition propagated over tens of micrometers along the mitochondrial tubules in the millisecond to second range after negative pressure was applied with FluidFM (Fig. 2e and Supplementary Movie 5). The shape transition of the matrix compartment propagated homogeneously along connected mitochondrial tubules, while the outer mitochondrial membrane (OMM) between the matrix foci initially remained intact. When traction was maintained for a few seconds, the OMM separated at one or more constriction sites between previously formed ‘pearls’, which resulted in isolated spherical mitochondria, while the remainder of the tubular structure relaxed and recovered (Supplementary Fig. 5a and Supplementary Movie 5). Furthermore, we demonstrate that the observed scission process of ‘pearling’ mitochondria (Fig 2e, Movie 5) succeeds recruitment of the fission machinery protein GTPase dynamin-related protein 1 (Drp1)²⁶ to the constricted sites (Supplementary Text and Supplementary Fig. 5).

We examined cell viability upon subcellular manipulation of ER and mitochondria and did not find it compromised (>95% cell viability) (Supplementary Fig. 4). To further ensure that our extraction protocol does not damage the cytoplasmic membrane upon probe insertion, we conducted a dedicated set of experiments and monitored potentially occurring Ca²⁺ influx from the cell culture medium using a fluorescent probe (mito-R-GECO1²⁷). Our experiments confirmed that there was no ion influx during and after manipulation, indicating integrity of the cytoplasmic membrane during organelle extraction (Supplementary text on Force-induced mitochondrial fission for details on fluorescent probes, conditions and controls, Supplementary Fig. 5 and 6, Movies 6-7). In addition, we were able to show that the shape transition towards

the pearls-on-a-string phenotype and subsequent mitochondrial fission inside the cytoplasm was calcium-independent (Supplementary Fig. 6, Movies 6-9).

Mitochondrial transplantation into cultured cells

Our next goal was to demonstrate the functional delivery of mitochondria into new host cells and to achieve cell-to-cell organelle transplantation. In contrast to mitochondria extraction, for which both pyramidal probes and cylindrical probes could be used (Fig. 1b; Supplementary Fig. 2), injection of mitochondria was possible only with the latter, newly developed probes. FluidFM offers two possibilities for mitochondrial transfer: transplanting mitochondria from a donor cell to a recipient cell by coupling mitochondrial extraction with re-injection of the extract into a new host cell, or back-filling FluidFM probes with mitochondria purified by subcellular fractionation, followed by injection (Fig. 3 a - d). Working with bulk-isolated mitochondria allows for a higher throughput of cells injected in series with one cantilever (> 1 cell per minute). However, such a protocol might be accompanied by reduced mitochondrial quality caused by the preceding purification process. We compared both approaches, the cell-to-cell approach (Fig. 3a) and the injection of purified mitochondria (Fig. 3c), with respect to the delivery of mitochondria into the cytoplasm of individual cultured HeLa cells. To visualize the transfer of mitochondria, we used donor and acceptor cells with a differentially labelled mitochondrial matrix (Fig. 3e, f; su9-mCherry and su9-BFP respectively). When transplanting mitochondria directly from cell to cell using FluidFM, we achieved successful transfer of mitochondria into the cytosol of the recipient cells in 95% of all cases, while maintaining cell viability (Fig. 3g, 39 out of 41 transplanted cells). Upon injection of purified mitochondria, we observed mitochondrial transfer and preserved cell viability in 46% of cases (19 of 41) (Fig. 3g, Supplementary Fig. 7). Quantification of the transplant showed that the number of transplanted mitochondria for these experiments varied from 3 to 15 mitochondria per cell (Fig. 3h). The different success rates between the two alternative protocols can be explained by differences in mitochondrial condition. Mitochondria quickly lose their membrane potential, undergo rupture of their outer membranes or accumulate adherent cytochrome *c* on their membranes under non physiological conditions²⁸. Irreversible damage of mitochondria leads to targeted degradation inside cells (mitophagy) and potentially apoptosis. While cell-to-cell transplantation of mitochondria reduces throughput, it has the advantage that the extracellular time is short (< 1 min) and that mitochondria sampled by FluidFM are maximally concentrated in native cytoplasmic fluid, bypassing the use of artificial buffers altogether. We ensured that the extract remained near the aperture during extraction by filling the probes with immiscible perfluorooctane before extraction and transplantation. Therefore, only small volumes (0.5 – 2 pL) are injected into the host cells (Fig. 3b), up to the

volume previously extracted from the donor cell (injection of larger volumes is automatically prevented due to inherent flow resistance properties of the pre-filled fluorocarbon liquid). Labeling mitochondria of the recipient cell (su9-BFP) in addition to labeling donor cell mitochondria (su9-mCherry) allowed us to survey the state of the mitochondrial network in the transplanted cell. In both transfer approaches described above (transplantation and purification followed by injection), the tubular, interconnected phenotype of the host-mitochondrial network remained unaltered by the injection process. In addition, labeling allowed us to monitor the fate of the transplanted mitochondria. We observed mitochondrial acceptance, defined by fusion of the transplant with the host mitochondria network, and thus overlap of both fluorescent signals- and mitochondrial degradation, marked by further fragmentation of the transplant and segregation into presumptive mitophagosomal structures (Fig. 3i - k). These processes were observed irrespective of the transfer method, cell-to-cell (Fig. 3i), or injection of purified mitochondria (Fig. 3j). We followed the fate of the transplant over time in 22 cells: 18 cells showed full mitochondrial fusion of the transplant and 4 cells showed mitochondrial degradation. Fusion events were first observed within 30 minutes post transplantation in the majority of cases (14 of 18 cells).

As indicated above, the high cell-to-cell transplant efficiency allows for direct observation of the fate of individually transplanted mitochondria. To showcase this, we transplanted labelled mitochondria (su9-mCherry) from HeLa cells into differentially labelled U2OS cells (su9-BFP), regularly used for studies of dynamic mitochondrial behavior. The strong label together with a highly sensitive EMCCD-camera (Andor) enables tracing of individual mitochondria within a recipient cell over time (Fig. 3l, Supplementary Movie 10). In this particular case, we observed rapid spread of the fluorescent mitochondrial matrix label after the initial fusion event to the network 23 minutes post transplantation.

In summary, we established two methods for mitochondria transfer into single cultured cells. One involves bulk purification of mitochondria and their injection into recipient cells. The injection protocol is rather rapid but inevitably compromises mitochondrial and cellular function. The second consists in cell-to-cell transplantation. Evaluation of cell viability and transplant fate showed an efficient protocol that allows observation of the dynamic behavior of transplanted mitochondria after transfer.

Fate of transplanted mitochondria in primary cells

Having developed an efficient protocol for cell-to-cell transplantation of mitochondria, we sought to test whether primary cells show similar uptake behavior as the tested cancer cells and, if so, what are the dynamics of integration of foreign mitochondria. We considered these particular experiments important because quality control mechanisms are impaired in cancer cell

lines²⁹ and to demonstrate the broad applicability of the established protocol. In addition, several studies link naturally occurring mitochondrial transfer events with short-term benefits for individual cells and tissues, for example in adipose tissue³⁰ or in neurons³¹. However, to the best of our knowledge, the fate of mitochondria or dose-response relationships have not been studied, and appropriate technologies of mitochondrial transfer that preserve cell viability have been lacking.

We used primary human endothelial keratinocytes (HEKa), a skin cell type that is generally susceptible to radiation damage and aging³². In standard culture conditions, the mitochondrial network of HEKa cells is mostly tubular, forming a large connected network (Supplementary Fig. 8) similar to HeLa cells studied above, indicating an active mitochondrial fusion machinery³³. Notably, cell-to-cell transplantation of mitochondria into HEKa cells showed no impact on their viability, allowing analysis of all injected cells. We conducted time-lapse experiments of transplanted labelled mitochondria (su9-mCherry) from HeLa cells into HEKa cells, focusing on the fluorescent signal of the transplant and its dynamic behavior over time (Fig. 4a, b and c Supplementary Movie 11). The analysis revealed the rate of transplant fusion with the host mitochondrial network and its movement inside the cytosol. In contrast to the findings described above for HeLa-to-HeLa transplantations, i.e. host cells either accepting or degrading mitochondria (Supplementary Fig. 9, 10), we observed a third, intermediate scenario in which single cells both fused-and degraded parts of the transplant. To further define the transplant uptake mechanisms in HEKa cells, we classified the transplanted mitochondria as primary particles – mitochondria that retain their original shape and fluorescence intensity, indicating that they have neither fused with the host network, nor been targeted to degradation –, secondary particles – mitochondria that retain their fluorescence but are distinctively smaller in size, suggesting fragmentation for degradation –, and tertiary particles – mitochondria fused with the host network, showing a characteristic decrease of transplant specific fluorescence (> 10 fold), due to dilution into the host mitochondrial network (Fig. 4d, e, Supplementary Movie 11). Shape transition of the transplant from discrete spheres towards tubules, was observed exclusively in the context of fusion of the transplant to the existing host network. Emergence of secondary particles hinted towards rearrangement of the transplant into parts recognized as ‘viable’ mitochondria, designated for fusion to the network, while another part was targeted for degradation. Tracing this process within an individual cell, we counted the number of ‘primary’ and ‘secondary’ particles over 14 h (Fig. 4f). In the first 3 h post injection, we observed an increase in ‘primary’- and ‘secondary particles’, which subsequently lost their high fluorescent signature while the fraction of fluorescent mitochondrial network increased over time (Fig. 4b, c). To test whether restructuring of the transplant into sub-particles was common in cells that showed emergence of secondary particles, we counted the number of primary and secondary

particles immediately after transplantation- and 3 h after in cells that showed both degradation and integration of the transplant (Fig. 4g; n = 10). The results indicated variance in the absolute extent of rearrangement; however, all cells showed an increased particle number by a factor of 1.7 ± 0.4 .

In this first set of transplantation experiments from HeLa cells to HEK293 cells, 12 cells showed complete uptake of the transplant, 6 showed both uptake and degradation of the transplant, and 4 fully degraded the transplant (Fig. 4h).

In the experiments described above, the first fusion or degradation events occurred 20 minutes post transplantation and continued for more than 16 hours. Remarkably, the speed at which the primary transplant was processed was independent of transplant sizes. Fusion or degradation of large transplants, >40 mitochondria per cell, advanced at similar rate as smaller transplants, <8 mitochondria per cell (Supplementary Movie 10, Supplementary Fig. 11).

As outlined above, the established cell-to-cell transplantation protocol is minimally invasive with regard to the integrity of the mitochondria themselves when using "healthy" donor cells, and cells receiving transplants from unperturbed donor cells showed mostly uptake of the transplant (Fig. 4h). Next, we wondered whether the acceptance of mitochondria by host cells was altered, if the quality of the transplant was impaired by prior drug treatment of the donor cell. Such treatments are commonly used to study the pathways that control the maintenance of the mitochondrial network. However, drugs have been applied to the entire cell so far, likely interfering with regulatory processes of cells as a whole. In consequence, the here established cell-to-cell transplantation of mitochondria provided an opportunity to follow the fate of damaged mitochondrial sub-populations in the context of an otherwise intact cell. *In vitro*, the chemical triggers used to study mitophagy are uncoupling agents, inhibitors of the respiratory chain or combinations thereof, robustly causing changes of membrane potential and simulating low mitochondrial quality³⁴. To investigate how otherwise healthy cells respond to impaired mitochondrial subpopulations, we treated transplant-donor cells with the proton ionophore CCCP (Supplementary Fig 8) and transplanted the depolarized mitochondria into HEK293 cells. The majority of cells, 14 of 22, showed fusion of initially depolarized mitochondria to the network, while 8 cells degraded the transplant (Fig. 4h). This reaction was similar to the previous condition tested, the transplantation of untreated mitochondria, which was unexpected, because literature suggests rapid mitochondrial degradation of mitochondria having lost their membrane potential³⁵. However, the membrane potential can potentially recover quickly, if a functional ATPase is present, as expected in our study. Next, we tested the influence of Doxycycline, an antibiotic, inhibiting protein synthesis of the mitochondrial ribosome, which induces fractionation of the mitochondrial network in HeLa cells after 24 h (Supplementary Fig. 8), putatively due to non-functional mitochondrial OXPHOS protein complexes³⁶. The reaction of

the host cells was similar as towards depolarized and untreated mitochondria: 15 show full fusion, 4 show both fusion and degradation and 3 show full degradation of the transplant. We then treated donor cells with H₂O₂, which damages proteins and induces double strand breaks in mtDNA. The fraction of mtDNA containing double strand breaks in H₂O₂ treated cells was reported to remain high for several hours post treatment³⁷ and the donor cells showed a fragmented mitochondrial network after 3 h (Supplementary Fig. 8). However, even upon H₂O₂ treatment, and even upon application of all drugs simultaneously to donor cells, mitochondrial acceptance in healthy recipient background was still comparable to all other conditions, indicating the potential of cells to cope with highly damaged mitochondria when occurring as isolated events (Fig. 4h, Supplementary Fig 12).

Since the tested conditions for drug-impaired mitochondria did not show an impact on mitochondrial uptake behavior, we wondered whether the amount of injected mitochondria might have an impact on transplantation outcome. Across all conditions, we transplanted 1117 mitochondria (Fig. 4i) and followed their fate in more than 100 individual primary cells after transplantation of 1 up to 53 mitochondria (Supplementary Fig. 12). Pooling uptake data of cross-tested conditions (n = 135 cells), we distributed the number of injected mitochondria per cell to bins of roughly equal cell numbers of 1, 2-5, 6-10 and >10 injected mitochondria per cell. We did not find any correlation between the number of transferred mitochondria per cell and their uptake behavior (Fig. 4j).

Overall, transplantations were successful in all experiments and cells remained viable, irrespective of the amount of transplant received. We demonstrated that primary HEKa cells incorporate a majority of transplanted mitochondria into their network via mitochondrial fusion. A subset of transplanted cells showed individualized responses, with one fraction of mitochondria fusing with the mitochondrial network and another subpopulation undergoing rearrangement associated with particle formation, while a third fraction was subjected to mitophagy. This behavior highlights the presence of quality control mechanisms that are in place to sort each mitochondrion and exemplifies the potential of the FluidFM approach to transplant mitochondria into new host cells to study their fate and host cell response with single mitochondria resolution.

Mitochondria transplantation and transfer of mitochondrial genomes

After demonstrating the short-term response of cells to mitochondrial transplantation, we focused on the long-term effects of mitochondrial transfer over generations of host cells. Mitochondria differ from other membrane compartments in that they carry their own genome, which is propagated within the cell's inherent mitochondrial pool. It has been shown that mtDNA can be transferred into somatic cells via miniaturized probes under selective pressure, either by

transfer into cells artificially rendered free of mitochondrial DNA (rho-zero cells)^{38,39} (2-25% efficiency), or by selection using antibiotics (< 0.01% efficiency)⁷. Therefore, the introduction of new mtDNA sequences into functional somatic cells remains a challenge^{40,41}. Before demonstrating the transfer of mtDNA into host cells upon transplantation, we first wondered whether the FluidFM-extracted mitochondria contain mitochondrial DNA, which is organized in discrete complexes termed mitochondrial nucleoids, because the extraction process leads to rapid fragmentation of the network. To visualize the behavior of mitochondrial nucleoids during mitochondrial extraction using FluidFM, we expressed a fluorescently tagged version of p55 (p55-GFP), a polymerase- γ subunit that co-localizes with mitochondrial nucleoids and appears in discrete speckles scattered throughout the mitochondrial matrix⁴² (Fig. 5a). We evaluated time-lapse experiments upon mitochondrial extraction with labelled nucleoids and counted mitochondrial fragments either containing labelled nucleoids, or being devoid of their fluorescent signal (Fig. 5b and Supplementary Fig. 13). We observed p55-GFP in > 90% of formed mitochondrial spheres (n = 18), indicating that most transplanted mitochondria contained mtDNA.

Next, we applied genomics to quantify uptake and maintenance of mtDNA after mitochondria transplantation (Fig. 5c). We compared two methods of mitochondrial transfer, using U2OS cells as mitochondria donors and HeLa cells as acceptors: direct cell-to-cell transplantation of mitochondria with FluidFM and FluidFM-injection of purified mitochondria. In addition, to control for non-specific uptake of mitochondria or otherwise unspecific mtDNA carryover, we seeded cells into a culture-dish and mixed them with extracted mitochondria from donor cells. All experiments were executed in biological triplicates and cells were passaged onto a fresh culture dish, for a more detailed description of the experimental procedure and conditions, see Supplementary information. Subsequently, we extracted DNA, then amplified and sequenced part of the variable D-loop region of the mitochondrial genome. Four single nucleotide polymorphisms⁴³ allowed the detection of transplanted mtDNA. The percentage of transplant mtDNA propagation was highest in samples from cell-to-cell mitochondria transplantation (mean 2 %), followed by FluidFM injection of purified mitochondria (mean 0.5%), whereas mtDNA transfer by non-specific uptake was below the detection limit (Fig. 5d and Supplementary Table 1 & 2). The obtained amount of mtDNA was well in line with our expectations considering the amount of mtDNA copies per cell (~1100)⁴⁴ and mtDNA copy number per nucleoid (3.2)⁴⁵, and the quantity of mitochondria we transplanted within this experimental series (Fig. 3k, median = 6).

In summary, we showed efficient transplantation of mitochondrial DNA into somatic cells without the need for selective pressure. These results indicate that HeLa cells show little or no

selection for mitochondrial DNA variants of another cell line, here U2OS cells, under standard culture conditions.

Discussion

The technology developed here allows the manipulation of intracellular compartments using FluidFM. We show the removal and injection of organelles from and into single cells without compromising organelle integrity nor cell viability. Subcellular sampling of organelles allows molecular downstream analyses, which are increasingly feasible thanks to the improving sensitivity of 'omics' technologies⁴⁶. Samplings can be performed at one time point, but also repeatedly from one cell to unravel the dynamic behavior within individual cells. We demonstrate the application of FluidFM to exert localized fluidic forces within single cells and thus expand the possibilities for subcellular sampling as well as the study of organelle mechanobiology^{14,23}. It has been proposed that mechanical forces and membrane constriction affect mitochondrial shape and dynamics^{47,48}, but with the previously established tools it has been difficult to test such a hypothesis without perturbing the cellular state as a whole. While the application of compressive force can be controlled in time and space⁴⁹, application of controlled tensile force has been impossible to date. Here, we demonstrate that mechanical force can be a driver for mitochondrial shape transition that is strictly localized to sites of tensile force application and propagates along membrane-connected mitochondrial tubes. Here, the purely mechanical nature of FluidFM presents itself as a strength, because it allows dissection from complex physiological stimuli, often involving calcium-influx, from isolated exertion of (hydrodynamic) pulling forces. Our experimental data are in-line with theoretical considerations^{50,51} that link mitochondrial shape to membrane tension (amongst other factors). An increase in membrane tension results in 'pearling', recruitment of Drp1 and fission, a process that we showed to be Ca²⁺-independent. The transition into the pearls-on-a-string phenotype appears to be an elegant solution that protects cells against membrane leakage during mechanical stress.

Transplantation of mitochondria at a high efficiency allowed us to track organelle fate over time in new genetic and physiological cell backgrounds. Similar to organ transplants that are accepted or rejected by new hosts, here we show rescue or failure of organelles within single cells after transplantation. We show that transplantation is highly efficient (95% success rate) when mitochondria are transplanted directly between living cells rather than using isolation protocols prior to transfer. The FluidFM-based approach of efficient mitochondria transplantation permitted us to evaluate mitochondrial quality control in primary cells by transplanting healthy

and compromised mitochondria and observing their fate. We show that individual cells generally differentiate between individual mitochondria, but do not display apparent responses to mitochondria previously exposed to the tested stresses. Across conditions, we observe that the majority of mitochondria become integrated into the host network and that transplanted mitochondria give rise to secondary mitochondrial particles. Such particles are reminiscent of mitochondrial-derived vesicles that take part in mitochondrial quality control^{52,53}. This indicates that the extent of mitochondrial quality control may depend on the general cellular state rather than the actual quality of the mitochondrial network. The study of mitochondrial quality control is of great interest, and the approach introduced here has the potential to significantly contribute further to this field by allowing defective mitochondria to be introduced locally in an otherwise functional cellular background. In addition, it will be interesting to study the impact of mitochondrial transplantation to the host cells considering metabolic activity and signaling responses. The manipulation and observation of mitochondrial subpopulations within a cell is important to drive discoveries in the dynamics e.g. of asymmetric cell division^{54,55}. We show here that subcellular manipulation using FluidFM extends the scope of such studies beyond the application of optogenetic tools and enables the transplantation and observation of mitochondrial subpopulations in single cells.

We tracked the short term-fate of mitochondrial subpopulations using fluorescent microscopy, but our protocol also allows for the study of the long-term impacts of mitochondrial transfer by showing the introduction of novel mtDNA variants into cell populations. While mitochondrial transfer into oocytes has been demonstrated^{56,57}, there are only few mechanistic insights into mtDNA selection in eukaryotic cells, with recent notable exceptions^{58,59}. Heteroplasmic cells were generated by injection of isolated mitochondria into large oocytes, reaching levels of 7%⁵⁹ of transplanted mtDNA under nonselective conditions, which is comparable with our method for somatic cells (up to 2.5%). With a spread from one up to about 50 transplanted mitochondria per cell and the opportunity to inject individual cells repeatedly, higher shares of heteroplasmic variants could be achieved. FluidFM thus represents a promising way to decipher modes of mtDNA selection in cell culture models. It will enable the identification of metabolic and genetic factors that impact shifts in mtDNA heteroplasmy and nuclear-mitochondrial crosstalk. Recently, mtDNA polymorphisms have been used to track cells *in vivo*⁶⁰. The FluidFM approach can directly introduce such polymorphisms, providing a genetic marker to track mtDNA within cells in complex settings.

In the future, the technique introduced here will stimulate applications in additional research areas, for example, the rejuvenation of cells with low metabolic activity in stem cell therapies² or as an alternative strategy in mitochondrial replacement therapy approaches. Beyond, it offers

new perspectives to address fundamental questions in cell biology, mechanobiology and cell engineering.

Acknowledgements

We thank Maximilian Mittelviehhaus (ETH Zurich), Patrick Frederix (Nanosurf AG, Switzerland), Pablo Dörig, and Dario Ossola (Cytosurge AG, Switzerland) for their support, as well as Stephen Wheeler (ETH Zurich) and the personnel of ETH ScopeM facility and the Functional Genomics Center Zurich for technical assistance. We thank Sean Munro for plasmids. This work was supported by a grant from the Volkswagen foundation (Initiative "Life" to J.A.V.), a European Research Council Advanced Grant (no. 883077 to J.A.V.), a European Research Commission Starting Grant (no. 337906 to B.K.), and the EUROSTARS project grant E!11644 "SOUL" (to E.S. and T.Z.).

Author Contributions

C.G.G., B.K. and J.A.V. designed the study. C.G.G. and J.A.V. wrote the manuscript with input from all authors. C.G.G. and Q.F. designed, executed and analyzed the experiments. C.G.G., O.G.G., E.S. and T.Z. designed and manufactured FluidFM-probes.

Supplementary material

Supplementary Fig. 1-13; Supplementary Movies 1-11, Supplementary Tables 1 & 2

Data Availability

Data to understand and assess the conclusion of this research are available in the main text, raw data sets will be made available upon request.

Code Availability

Matlab code used for image analysis and mitochondrial particle distribution will be made available upon request.

References

1. Buck, M. D. D. *et al.* Mitochondrial dynamics controls T cell fate through metabolic programming. *Cell* **166**, 63–76 (2016).
2. Sun, N., Youle, R. J. & Finkel, T. The mitochondrial basis of aging. *Mol. Cell* **61**, 654–666 (2016).
3. Kauppila, T. E. S., Kauppila, J. H. K. & Larsson, N. G. Mammalian mitochondria and aging: An update. *Cell Metab.* **25**, 57–71 (2017).
4. Archer, S. L. Mitochondrial dynamics - Mitochondrial fission and fusion in human diseases. *N. Engl. J. Med.* **369**, 2236–2251 (2013).
5. Mishra, P. & Chan, D. C. Mitochondrial dynamics and inheritance during cell division, development and disease. *Nat. Rev. Mol. Cell Biol.* **15**, 634–646 (2014).
6. Vevea, J. D., Swayne, T. C., Boldogh, I. R. & Pon, L. A. Inheritance of the fittest mitochondria in yeast. *Trends Cell Biol.* **24**, 53–60 (2014).
7. Clark, M. A. & Shay, J. W. Mitochondrial transformation of mammalian cells. *Nature* **295**, 605–607 (1982).
8. Liu, D. *et al.* Intercellular mitochondrial transfer as a means of tissue revitalization. *Signal Transduct. Target. Ther.* **6**, (2021).
9. Santos-Ferreira, T. *et al.* Retinal transplantation of photoreceptors results in donor-host cytoplasmic exchange. *Nat. Commun.* **7**, 1–7 (2016).
10. Rustom, A., Saffrich, R., Markovic, I., Walther, P. & Gerdes, H. H. Nanotubular Highways for Intercellular Organelle Transport. *Science (80-.).* **303**, 1007–1010 (2004).
11. Caicedo, A., Aponte, P. M., Cabrera, F., Hidalgo, C. & Khoury, M. Artificial mitochondria transfer: Current challenges, advances, and future applications. *Stem Cells Int.* **2017**, (2017).
12. Chernyak, B. V. Mitochondrial transplantation: A critical analysis. *Biochem.* **85**, 636–641 (2020).
13. Actis, P. Sampling from Single Cells. *Small* **1700300**, 1–11 (2018).
14. Nadappuram, B. P. *et al.* Nanoscale tweezers for single-cell biopsies. *Nat.*

- Nanotechnol.* **14**, 80–88 (2019).
15. Tóth, E. N. *et al.* Single-cell nanobiopsy reveals compartmentalization of mRNAs within neuronal cells. *J. Biol. Chem.* **293**, 4940–4951 (2018).
 16. Guillaume-Gentil, O. *et al.* Single-Cell mass spectrometry of metabolites extracted from live cells by Fluidic Force Microscopy. *Anal. Chem.* **89**, 5017–5023 (2017).
 17. Zhu, H. *et al.* Metabolomic profiling of single enlarged lysosomes. *Nat. Methods* **18**, (2021).
 18. Wu, T. *et al.* Photothermal nanoblade for large cargo delivery into mammalian cells. *Anal. Chem.* **83**, 1321–1327 (2011)
 19. Kang, E. *et al.* Mitochondrial replacement in human oocytes carrying pathogenic mitochondrial DNA mutations. *Nature* **540**, 270–275 (2016).
 20. Meister, A. *et al.* FluidFM: Combining atomic force microscopy and nanofluidics in a universal liquid delivery system for single cell applications and beyond. *Nano Lett.* **9**, 2501–2507 (2009).
 21. Guillaume-Gentil, O. *et al.* Force-controlled manipulation of single cells: From AFM to FluidFM. *Trends Biotechnol.* **32**, 381–388 (2014).
 22. Guillaume-Gentil, O. *et al.* Force-controlled fluidic injection into single cell nuclei. *Small* **9**, 1904–1907 (2013).
 23. Guillaume-Gentil, O. *et al.* Tunable single-cell extraction for molecular analyses. *Cell* **166**, 506–517 (2016).
 24. Milo, R., Jorgensen, P., Moran, U., Weber, G. & Springer, M. BioNumbers The database of key numbers in molecular and cell biology. *Nucleic Acids Res.* **38**, 750–753 (2009).
 25. Barbara Stolz, J. B. Sequestration of iontophoretically injected calcium by living endothelial cells. *Cell Calcium* **8**, 103–121 (1987).
 26. Smirnova, E., Shurland, D. L., Ryazantsev, S. N. & Van Der Blik, A. M. A human dynamin-related protein controls the distribution of mitochondria. *J. Cell Biol.* **143**, 351–358 (1998).
 27. Wu, J. *et al.* Improved orange and red Ca²⁺ indicators and photophysical

- considerations for optogenetic applications. *ACS Chem. Neurosci.* **4**, 963–972 (2013).
28. Rendon, D. A. Important methodological aspects that should be taken into account during the research of isolated mitochondria. *Anal. Biochem.* **589**, 113492 (2020).
 29. Denison, S. R. *et al.* Alterations in the common fragile site gene Parkin in ovarian and other cancers. *Oncogene* **22**, 8370–8378 (2003).
 30. Brestoff, J. R. *et al.* Intercellular mitochondria transfer to macrophages regulates white adipose tissue homeostasis and is impaired in obesity. *Cell Metab.* **33**, 270–282 (2021).
 31. Hayakawa, K. *et al.* Transfer of mitochondria from astrocytes to neurons after stroke. *Nature* **535**, 551–555 (2016).
 32. Yaar, M. & Gilchrist, B. A. Ageing and photoageing of keratinocytes and melanocytes. *Clin. Exp. Dermatol.* **26**, 583–591 (2001).
 33. van der Bliek, A. M., Shen, Q. & Kawajiri, S. Mechanisms of mitochondrial fission and fusion. *Cold Spring Harb. Perspect. Biol.* **5**, (2013).
 34. Zachari, M. & Ktistakis, N. T. Mammalian mitophagosome formation: A focus on the early signals and steps. *Front. Cell Dev. Biol.* **8**, 1–11 (2020).
 35. Narendra, D., Tanaka, A., Suen, D. F. & Youle, R. J. Parkin is recruited selectively to impaired mitochondria and promotes their autophagy. *J. Cell Biol.* **183**, 795–803 (2008).
 36. Moullan, N. *et al.* Tetracyclines disturb mitochondrial function across eukaryotic models: A call for caution in biomedical research. *Cell Rep.* **10**, 1681–1691 (2015).
 37. Yang, M. *et al.* Human OXR1 maintains mitochondrial DNA integrity and counteracts hydrogen peroxide-induced oxidative stress by regulating antioxidant pathways involving p21. *Free Radic. Biol. Med.* **77**, 41–48 (2014).
 38. Wu, T. *et al.* Mitochondrial Transfer by Photothermal Nanoblade Restores Metabolite Profile in Mammalian Cells. *Cell Metab.* **23**, 921–929 (2016).
 39. Sercel, A. J. *et al.* Stable transplantation of human mitochondrial DNA by high-throughput, pressurized isolated mitochondrial delivery. *Elife* **10**, 1–45 (2021).

40. Yang, Y.-W. & Koob, M. D. Transferring isolated mitochondria into tissue culture cells. *Nucleic Acids Res.* **40**, e148 (2012).
41. Yoon, Y. G. & Koob, M. D. Intramitochondrial transfer and engineering of mammalian mitochondrial genomes in yeast. *Mitochondrion* **46**, 15–21 (2019).
42. Kaguni, L. S. DNA polymerase γ , the mitochondrial replicase. *Annu. Rev. Biochem.* **73**, 293–320 (2004).
43. Lott, M. T. *et al.* MtDNA variation and analysis using Mitomap and Mitomaster. *Curr. Protoc. Bioinforma.* **44**, 1–26 (2013).
44. Bogenhagen, D. & Clayton, D. A. The number of mitochondrial deoxyribonucleic acid genomes in mouse L and human HeLa cells. Quantitative isolation of mitochondrial deoxyribonucleic acid. *J. Biol. Chem.* **249**, 7991–7995 (1974).
45. Satoh, M. & Kuroiwa, T. Organization of multiple nucleoids and DNA molecules in mitochondria of a human cell. *Exp. Cell Res.* **196**, 137–140 (1991).
46. Chen, W. *et al.* Single Cell Omics: From Assay Design to Biomedical Application. *Biotechnol. J.* **15**, 1–10 (2020).
47. Helle, S. C. J. *et al.* Mechanical force induces mitochondrial fission. *Elife* **6**, 1–26 (2017).
48. Friedman, J. R. *et al.* ER tubules mark sites of mitochondrial division. *Science* **334**, 358–362 (2011).
49. Li, Q. S., Lee, G. Y. H., Ong, C. N. & Lim, C. T. AFM indentation study of breast cancer cells. *Biochem. Biophys. Res. Commun.* **374**, 609–613 (2008).
50. Gonzalez-Rodriguez, D. *et al.* Elastocapillary Instability in Mitochondrial Fission. *Phys. Rev. Lett.* **115**, 1–5 (2015).
51. Carlini, L., Mahecic, D., Kleele, T., Roux, A. & Manley, S. Membrane bending energy and tension govern mitochondrial division. *BioRxiv* 1–34 (2018). doi:10.1101/255356
52. Cadete, V. J. J. *et al.* Formation of mitochondrial-derived vesicles is an active and physiologically relevant mitochondrial quality control process in the cardiac system. *J. Physiol.* **594**, 5343–5362 (2016).

53. Sugiura, A., McLelland, G., Fon, E. A. & McBride, H. M. A new pathway for mitochondrial quality control: mitochondrial-derived vesicles. *EMBO J.* **33**, 2142–2156 (2014).
54. Katajisto, P. *et al.* Asymmetric apportioning of aged mitochondria between daughter cells is required for stemness. *Science* **348**, 340–343 (2015).
55. Moore, A. S. *et al.* Actin cables and comet tails organize mitochondrial networks in mitosis. *Nature* **591**, 659–664 (2021).
56. Mobarak, H. *et al.* Autologous mitochondrial microinjection; A strategy to improve the oocyte quality and subsequent reproductive outcome during aging. *Cell Biosci.* **9**, 1–15 (2019).
57. Reznichenko, A. S., Huyser, C. & Pepper, M. S. Mitochondrial transfer: Implications for assisted reproductive technologies. *Appl. Transl. Genomics* **11**, 40–47 (2016).
58. Floros, V. I. *et al.* Segregation of mitochondrial DNA heteroplasmy through a developmental genetic bottleneck in human embryos. *Nat. Cell Biol.* **20**, 144–151 (2018).
59. Lieber, T., Jeedigunta, S. P., Palozzi, J. M., Lehmann, R. & Hurd, T. R. Mitochondrial fragmentation drives selective removal of deleterious mtDNA in the germline. *Nature* **570**, 380–384 (2019).
60. Ludwig, L. S. *et al.* Lineage Tracing in Humans Enabled by Mitochondrial Mutations and Single-Cell Genomics. *Cell* **176**, 1325–1339 (2019).

Figures

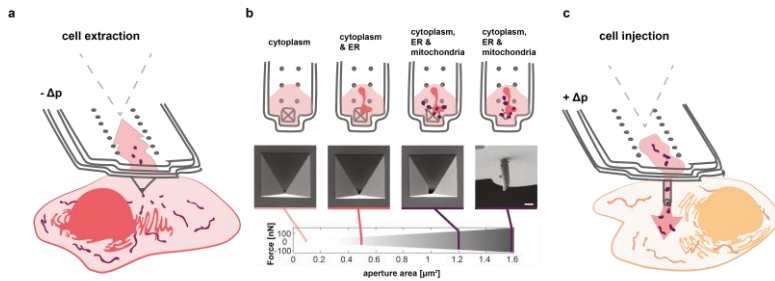


Fig. 1: **a**, Schematic of organelle extraction using FluidFM. Extraction volumes are tuned by applying negative pressure ($-\Delta p$). Probe prefilling with octadecafluorooctane allows for optical and physical separation of the extract within the cantilever. **b**, Selective extraction of organelle components by tuning the aperture size and thus the applicable range of applied fluidic forces. Top row: Schematic view of extracted cell components inside the cantilever. Middle row: scanning electron microscopy images of cantilever apertures with different apertures. Bottom row: Range of applicable fluidic forces with adapted FluidFM cantilevers. Scale bar. $2 \mu\text{m}$. **c**, Schematic of mitochondria injection into single cells by applying positive pressure ($+\Delta p$) once the cantilever was inserted into the recipient cell.

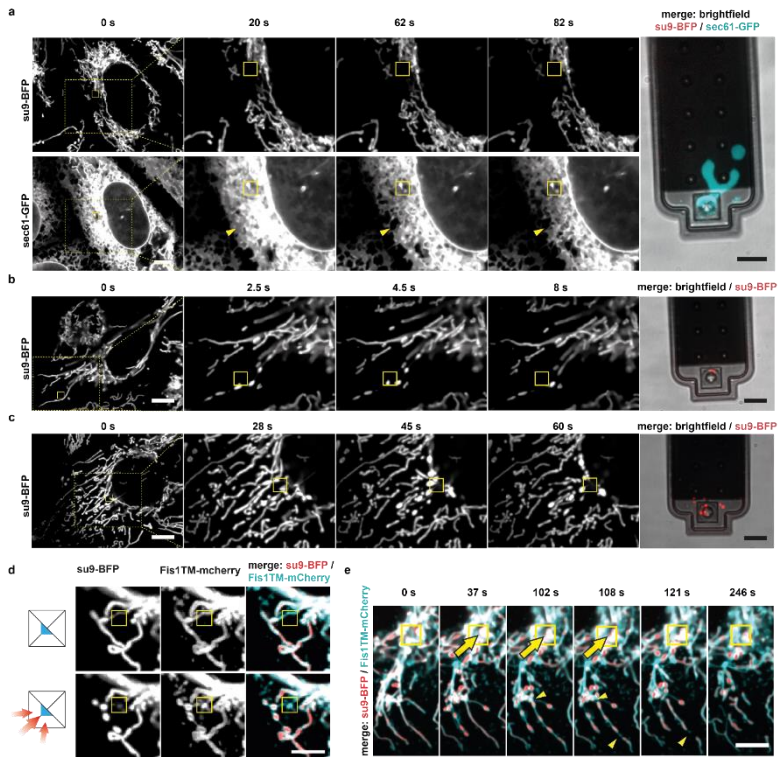


Fig. 2: Organelle extraction. Time-lapse images of live-cell compartment extractions and z-stacks of pyramidal cantilevers post-extraction. Yellow boxes indicate position of the cantilever apex inside the cell. **a**, U2OS cell expressing su9-BFP (mitochondria) and Sec61-GFP (ER, cyan) during extraction. Arrows indicate the zone of ER retraction. A cantilever with an aperture of $0.5 \mu\text{m}^2$ was used. Scale bar: $10 \mu\text{m}$. See also: Supplementary Movies 1 and 2. **b**, Extraction of a single mitochondrion from a viable U2OS cell expressing su9-BFP. A cantilever with a $1 \mu\text{m}^2$ aperture was used. Scale bar: $10 \mu\text{m}$. See also: Supplementary Movie 3 **c**, Extraction of several mitochondria from a viable U2OS cell expressing su9-BFP. A cantilever with a $1 \mu\text{m}^2$ aperture was used. Scale bar: $10 \mu\text{m}$. See also: Supplementary Movie 4 **d**, Images of U2OS cells expressing Fis1TM-mCherry (OMM, cyan) and su9-BFP (mitochondrial matrix, red). Top panels: Cantilever apex is inserted inside the cell, $\Delta p = 0$ mbar. Bottom panels: Negative pressure is applied, $\Delta p = -50$ mbar. Scale bar: $5 \mu\text{m}$. **e**, Time-lapse of mitochondrial network upon pulling. Arrowheads indicate sites of a fission event. Scale bar: $10 \mu\text{m}$. See also: Supplementary Movie 5.

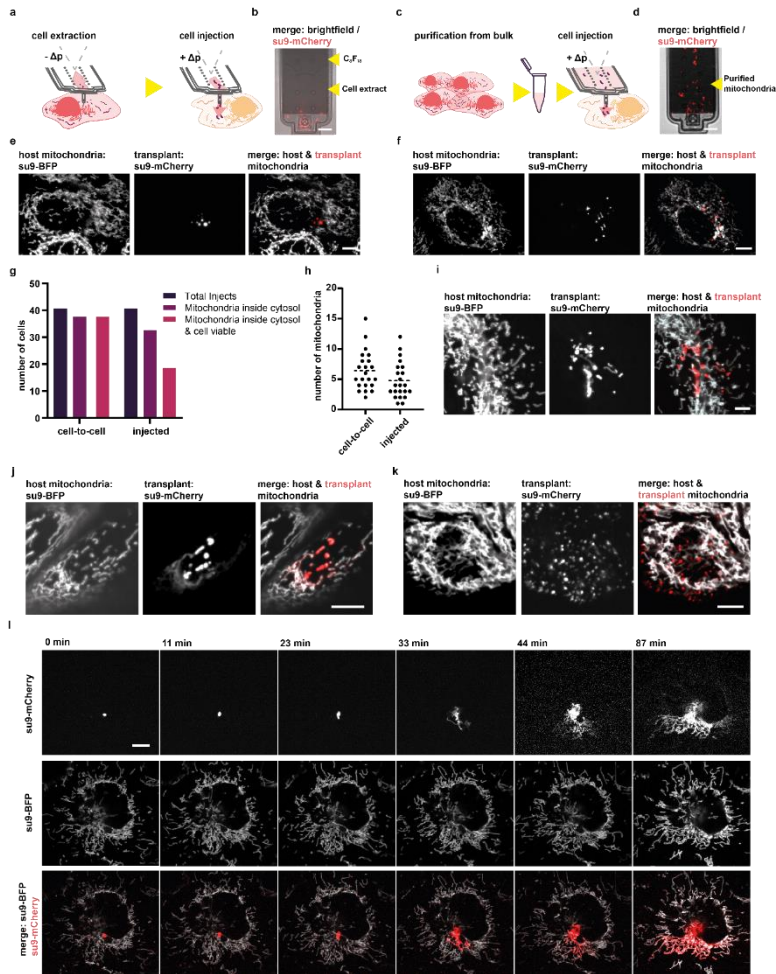


Fig. 3: Mitochondrial transplantation. **a**, Scheme of mitochondrial transplantation using the cell-to-cell transfer approach: Mitochondria are extracted via FluidFM-aspiration. Subsequently, the cantilever holding the extract is moved to a recipient cell and the extract is injected. **b**, Image of a FluidFM cantilever pre-filled with Perfluorooctane (C_8F_{18}) after mitochondrial extraction, mitochondria are labelled via su9-mCherry. The border between the extract and C_8F_{18} can be seen due to different refractive indexes of the two solutions. Extracted volume ~ 0.8 pL. Scale bar: 10 μ m. **c**, Scheme of mitochondrial transplantation using mitochondria purified by a standard mitochondrial purification protocol. The purified mitochondria are resuspended in HEPES-2 buffer and filled directly into the fluidic probe. Cells can be injected consecutively. **d**, Image of a FluidFM cantilever filled with mitochondria isolated from bulk, labelled via su9-mCherry. Scale bar: 10 μ m. **e**, Images of a recipient cell post mitochondrial transplantation via the cell-to-cell approach. The host cells' mitochondrial network is labelled via su9-BFP and the transplant is labelled via su9-mCherry. Scale bar: 10 μ m. **f**, Images of a recipient cell post mitochondrial transplantation via the injection of isolated mitochondria approach, labels similar to c. Scale bar: 10 μ m. **g**, Evaluation of mitochondrial transplantation via the cell-to-

cell approach upon optical inspection and the injection of isolated mitochondria approach. A total of 40 cells were evaluated per approach. **h**, Absolute numbers of transplanted mitochondria of 22 individual cells evaluated for the cell-to-cell and the injection of isolated mitochondria approach. **i**, Fusion states of transplanted mitochondria 30 post cell-to-cell transplantation. Mitochondria can be visualized carrying both fluorescent labels of the transplant (su9-mCherry) and of the host mitochondrial network (su9-BFP). Scale bar: 5 μ m. **j**, Fusion states of transplanted mitochondria 30 post injection of purified mitochondria, similar labelling as in **g**. Scale bar: 5 μ m. **k**, Degradation of transplanted mitochondria, the transplant is split into multiple smaller fluorescent vesicles (su9-mCherry) showing no overlap of fluorescence with the labelled host cell mitochondrial network (su9-BFP). Scale bar: 5 μ m. **l**, Time lapse image series of a single transplanted mitochondrion (su9-mCherry). The organelle donor was a HeLa cell, recipient cell is a U2OS-cell with a fluorescently labelled mitochondrial network (su9-BFP). Scale bar: 10 μ m.

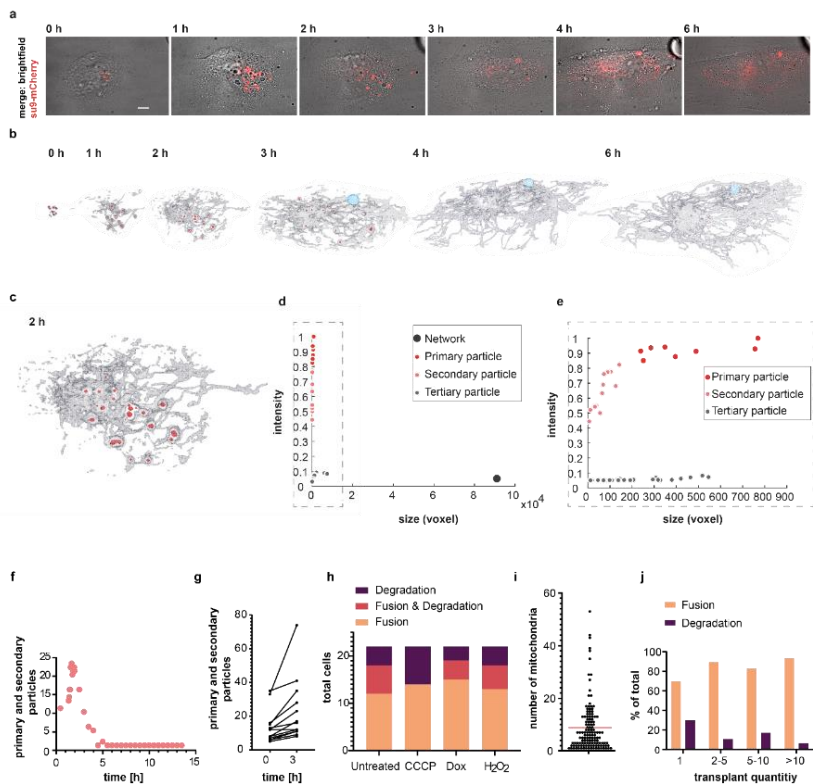


Fig. 4: Mitochondrial fate in HEKA cells. **a**, Time series of cell-to-cell transplantation from HeLa (su9-mCherry) to HEKA, fusion and degradation to the unlabeled host cell network. Scale bar: 10 μm . **b**, Surface-renderer (total su9-mCherry signal) of the time-lapse series of mitochondrial fusion and degradation within the host cell shown in **a**. The transplant is depicted in red, host cell mitochondrial network carrying fluorescent traces of the transplant is shown in grey, presumptive mitophagosomal structure is shown in light blue. **c**, enlarged section of the 2 h timepoint surface render from **b**. **d**, Scatter plot of size and normalized fluorescence intensity distribution of objects detected at the 2 h- timepoint. **e**, Zoom in on low-size fraction of the scatter plot shown in **c**. **f**, Total number of objects classified as primary transplant or secondary particle over time. **g**, Absolute number of primary and secondary particles detected directly after transplantation (0 h) and after 3 hours for 12 cells. **h**, Fusion and degradation behavior of drug-compromised mitochondrial transplants in HEKA cells. Each condition was tested with 22 cells. **i**, Distribution of mitochondrial quantity transplanted per cell from all conditions tested in **e**, total number of cells: 132. Dashed line indicates mean value. Total number of transplanted mitochondria: 1117. **j**, Correlation of the absolute number of transplanted mitochondria per cell with the cell response of either mitochondrial fusion- or degradation across all transplant conditions in percent. Total cell number: $n = 135$.

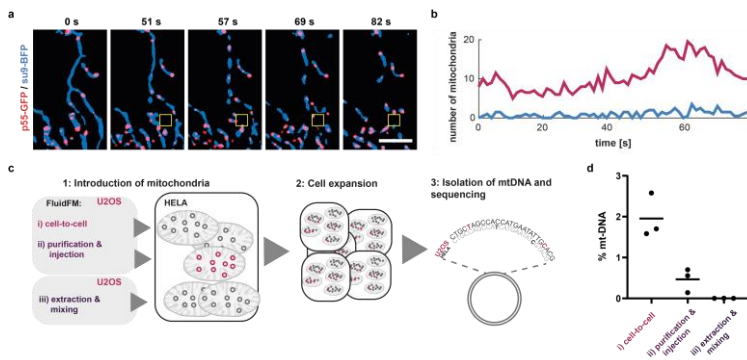


Fig. 5: Mitochondria transplantation and transfer of mitochondrial genomes. **a**, Time-lapse evaluation of mitochondria extraction visualizing mitochondrial nucleoids. An overlay of mitochondrial matrix shown in blue (su9-BFP) and mitochondrial nucleoids shown in red (p55-GFP). Yellow box indicates position of the cantilever. **b**, Dynamic localization of labelled nucleoids within a fractionating mitochondrial network. Plotted are the total amounts of mitochondria (su9-BFP) that show overlap with a labelled nucleoid (p55-GFP) in red and idle mitochondria showing no fluorescent trace of p55-GFP in blue over time. See also Supplementary Fig. 13. Scale bar: 5 μm . **c**, Strategy for the quantification of mtDNA maintenance after mitochondrial transplantation. **d**, Quantification of retained U2OS mtDNA in transplanted HeLa cells of all approaches tested. Bars indicate mean value.

Supplementary Materials for

Mitochondria transplantation between living cells

Christoph G. Gäbelein¹, Qian Feng², Edin Sarajlic³, Tomaso Zambelli⁴, Orane Guillaume-Gentil¹, Benoît Kornmann^{2,5}, Julia A. Vorholt^{1*}

¹Institute of Microbiology, ETH Zurich, 8093 Zurich, Switzerland

²Institute of Biochemistry, ETH Zurich, 8093 Zurich, Switzerland

³SmartTip BV, 7500 AH Enschede, The Netherlands

⁴Institute for Biomedical Engineering, ETH Zurich, 8092 Zurich, Switzerland.

⁵Department of Biochemistry, University of Oxford, Oxford OX1 3QU, United Kingdom

*e-mail: jvorholt@ethz.ch

This includes:

Materials and Methods
Supplementary Text mitochondrial fission
Fig. S1 to S13
Captions for Movies 1 to 11
Tables 1 & 2

Other Supplementary Materials for this manuscript include the following:

Movies 1 to 11

Supplementary Materials and Methods

Fabrication process of FluidFM probes with a cylindrical tip. The process starts with a standard 4" silicon wafer in the (100) crystallographic orientation. A 400 nm thick silicon-rich nitride (SiRN) layer is deposited by Low Pressure Chemical Vapor Deposition (LPCVD) on the selected wafer. The thickness of the SiRN layer determines the thickness of the bottom wall of the microfluidic channel. A silicon oxide layer is deposited by LPCVD from TEOS on the top of the SiRN layer. Then, a circular opening is patterned by Reactive Ion Etching (RIE) on the deposited multilayer. By using Deep Reactive Ion Etching (DRIE), a cylindrical pattern is subsequently formed in silicon. The depth of the cylindrical mold defines the height of the cylindrical tip. After formation of the cylindrical mold, a 150 nm thick SiRN layer is deposited by LPCVD. The thickness of the second SiRN layer determines the thickness of the walls in the cylindrical tip. After the tip molding, a blanket etch (RIE without an etching mask) RIE is performed to remove silicon nitride from the top surface of the wafer and from the bottom of the cylindrical mold. Due to the directionality of the RIE process, the material on the side-walls is preserved. The silicon oxide layer, which protects the underlying SiRN layer during the RIE etching, is removed. Subsequently, a 1500 nm thick polysilicon layer is deposited by LOCVD. Polysilicon is used as a sacrificial material to form a microfluidic channel. The thickness of the polysilicon layer determines the height of the microfluidic channel. The layout of the microchannel is patterned by RIE of polysilicon. A SiRN layer with a thickness of 400 nm is deposited by LPCVD after the patterning of polysilicon. This SiRN layer forms the top wall of the fluidic microchannel. The layout of the cantilever and the inlet of the microchannel are defined by RIE of silicon nitride. Next, a reflective metal layer is deposited and patterned on the cantilever. The silicon wafer is anodically bonded to a pre-diced glass wafer in which the fluidic inlets are pre-manufactured by powder blasting. After the anodic bonding, the sacrificial polysilicon layer is removed by TMAH etching in order to empty the microchannel and form a hollow cantilever. The bulk silicon is also removed during the TMAH etching to completely release the cantilever. A small part of silicon remains underneath the microfluidic inlet to provide mechanical strength for the channel walls.

FluidFM probe processing and FIB-SEM imaging and milling. The FluidFM-probes were mounted into a custom probe holder and coated with an 18 nm carbon layer using a CCU-010 Carbon Coater (Safematic) before milling by a FIB-SEM Nvision 40 device (Zeiss) using the Atlas software (Zeiss).

Pyramidal probes used for extraction of organelles and hydrodynamic pulling experiments: The milled face of the pyramidal probe was aligned perpendicularly to the FIB-beam equipped with a gallium ion source. Subsequently, the probes were milled with an acceleration voltage of 30 kV at 10 pA until the aperture was milled, controlled by optical observation (approximately to an electric charge of 10 nC per μm^2). The pyramidal probes have a 100 nm thick silicon nitride layer at the aperture region.

Cylindrical probes used for mitochondrial transplantation experiments were 'sharpened' by milling the probe apex at a 45° angle alongside the cylinder at an acceleration voltage of 30 kV at 40 pA. The probes were optically controlled after the milling procedure.

Then, the probes were glued onto a cytoclip holder by Cytosurge. Before each experiment, the cantilevers were cleaned by a 90 s plasma treatment (Plasma Cleaner PDG-32G, Harrick Plasma) before coating overnight with vapor phase SL2 Sigmacote (Sigma-Aldrich) in a vacuum desiccator. The siliconized probe was oven dried at 100 °C for 1 h. The cantilever spring constant was measured using software-implemented scripts (cylindrical probes: $2 \pm 0.4 \text{ Nm}^{-1}$, pyramidal probes: $5 \pm 1 \text{ Nm}^{-1}$). Probes were filled with a low-salt injection buffer (10 mM 4-(2-hydroxyethyl) piperazine-1-ethanesulfonic acid (HEPES), 150 mM NaCl in Millipore water adjusting the pH to 7.4 with KOH).

FluidFM setup and Microscopy. The FluidFM setup is composed of a FlexAFM 5-NIR scan head controlled by a C3000 controller (Nanosurf), a digital pressure controller (ranging from -800 mbar to +1000 mbar), and Microfluidic Probes (Cytosurge). The scan head is mounted on an inverted AxioObserver microscope equipped with a temperature-controlled incubation chamber (Zeiss). The microscope is coupled to a spinning disc confocal microscope (Visitron) with a Yokogawa CSU-W1 scan head and an EMCCD camera system (Andor). For all images and videos, a 63× oil objective with 1.4 numerical aperture and a 2× lens switcher was used (without lens switcher: 4.85 pixel/micron and 9.69 pixel per micron with lens switcher); images are in 16bit format. Image acquisition was controlled using the VisiView software (Visitron); linear adjustments and video editing were made with Fiji¹; additionally, images and videos were noise-filtered using the wiener noise filtering function (wiener2; 3 by 3 neighborhood size) in MatlabR2018a (MathWorks). Movies were created using a self-written Matlab script in order to visualize several sections or channels within the same movie. The colormap used for figure 3c originates from Thyng et al.² Images of cantilevers containing extracts (Figure 2, Figure S4) were created by summing the slices of a Z-stack via Fiji.

Cell Culture. U2OS, COS7, and HeLa cells were maintained in Dulbecco's Modified Eagle Medium containing 1% penicillin-streptomycin (ThermoFisher) and 10% fetal bovine serum (ThermoFisher) culture medium at 37°C and 5% CO₂ in a humidified incubator. Primary adult human endothelial keratinocytes (HEKa) cells were purchased from ThermoFisher. HEKa cells were cultivated in EpiLife™ Medium, with 60 μM calcium, with Human Keratinocyte Growth Supplement, 1%, (ThermoFisher) and Gentamicin/Amphotericin Solution (ThermoFisher). Cells were seeded 48 h preceding the experiments onto 50-mm tissue-culture treated low μ-dishes (ibidi) inside two-well culture inserts (ibidi) or, for experiments coupling mitochondrial extraction via FluidFM to injection of mitochondria, inside 4-well micro-inserts (ibidi). For the experiments, the culture media was replaced with CO₂-independent growth medium containing 10% FBS (ThermoFisher) and 1% penicillin-streptomycin (ThermoFisher). Cell lines stably expressing fluorescent proteins markers were created via lentiviral transduction, the constructs were previously described in Helle et al³.

Transient transfection. U2OS-cells were seeded 72 h preceding the experiment into two-well culture inserts (ibidi) inside 50-mm tissue-culture treated low μ-dishes (ibidi) in a total volume of 100 μL per well. Transfections were performed overnight 36 h preceding the experiment using 0.2 μg plasmid DNA and 0.2 μL Lipofectamine P3000 solution following the manufacturer's instructions (ThermoFisher). The media was exchanged to standard culture medium 12 h post transfection. The plasmid used for calcium imaging CMV-mito-R-GECO1 was a gift from Robert Campbell (Addgene plasmid #46021; <http://n2t.net/addgene:46021>; RRID: Addgene_46021).

Mitochondrial pulling and extraction experiments. All experiments were executed at 37°C. The cells for extraction/transplantation were selected by light microscopy. Z-stacks were taken before and after the manipulation step to document the workflow. Subsequently, the FluidFM probe was moved over a targeted area in the cytosol of a selected cell, usually close to the nucleus or mitochondrial tubes in the cell periphery. The cantilever was then inserted at the specified location driven by a forward force spectroscopy routine in contact mode, until the setpoint of 400 nanoNewtons (nN) was reached. The probe was then kept at this position (in the X-Y dimension) at the given force offset. Then, negative pressure in the range between -10 to -150 mbar was applied to aspirate cellular content. Before retracting the probe at the end of the aspiration process, the pressure was set back to 0 mbar. The force setpoint was adjusted by analyzing force distance curves from neighboring cells within the same experiment; the force value at which the curve takes a linear shape (in this case 80 nN) was estimated. This force value marks the point at which the probe makes contact with the glass bottom below the cell; consequently, this value was chosen as a setpoint for the extraction. Extraction of the ER fraction:

The experiments were performed using pyramidal cantilevers featuring an aperture area of $0.5 \mu\text{m}^2$ (see Fig. 1b) at -20 mbar using U2OS - or COS7 cells. Experiments for both cell lines were repeated twice on different days. Extraction of mitochondria and mitochondria pulling experiments were performed using pyramidal cantilevers featuring an aperture area of $1 \mu\text{m}^2$ or cantilevers with a cylindrical apex featuring an aperture area of $1.5 \mu\text{m}^2$ (see Fig. 1b) at -20 to -100 mbar using U2OS - or HeLa cells. Experiments including extraction of mitochondria were executed in 32 individual experimental setups on 32 individual days. Experiments showing recruitment of Drp1 were repeated four times on four different days with at least five cells per experiment in U2OS cells. Mitochondrial pulling experiments connected with calcium-imaging and thapsigargin-treatment (Fig. 5) were executed three times, each time on an individual day with at least seven cells per experiment.

For probe insertion with minimal Ca^{2+} influx as shown in Movie S7, newly coated (Sigmacote, see above) FluidFM cantilevers were used. To deliberately disturb the cell membrane (Movie S9), the probe was driven into the cell using the same setpoint, then the optical table (Newport) was gently flicked with the index finger to cause the probe to shift slightly, effectively disturbing the cell membrane. Cell viability was controlled using the LIVE/DEAD cell imaging kit (ThermoFisher).

Mitochondrial transplantation experiments. FluidFM injection of bulk-purified mitochondria: Mitochondria were purified from approximately 2×10^6 cultured U2OS cells continuously expressing the mitochondrial matrix marker su9-mCherry using the Qproteome Mitochondria Isolation Kit (Qiagen) following manufacturer's instructions. After purification, the mitochondria were washed two times in injection buffer (see above), and finally resuspended in $40 \mu\text{l}$ injection buffer before being loaded into FluidFM-probes having a sharpened cylindrical apex.

Coupling mitochondrial extraction with transplantation from individual cell to cell: FluidFM cantilevers were prefilled with Octadecafluorooctane (Sigma-Aldrich) to isolate the extract from the cantilever fluid in phase. Mitochondria were aspirated as described above, using FluidFM-probes having a sharpened cylindrical apex from U2OS-cells that were co-cultured on the same dish, previously seeded within another quadrant of the 4-well micro insets. Subsequently, the probe was moved to a region containing cells targeted for transplantation. For injection of mitochondria, the probe was positioned above a target cell as described above for the extraction of organelles. The cantilever containing the organelles was then inserted into the cell in contact mode (setpoint 400 nN). The injection process is controlled by observing the process in brightfield in real-time, at first, a positive pressure of 20 mbar was applied, if this did not cause the cell to visibly inflate, the pressure was slowly increased until such an inflation was visible. The pressure was then set to 0 mbar and the probe was retracted. Z-stacks were taken to control for successfully transferred mitochondria. Cell viability was controlled using the LIVE/DEAD cell imaging kit (ThermoFisher) following manufacturers instruction. Both experimental approaches were performed in six individual experiments, each on individual days.

Quantification of genetic incorporation of transplanted mitochondria. All experiments were conducted in biological triplicates. (A) FluidFM-injection of purified mitochondria: Single HeLa cells continuously expressing the mitochondrial matrix marker su9-BFP were seeded into a single quadrant of a 4-well micro-insert (ibidi) 72h before the experiment, at the day of the experiment, each seeded well contained 4-6 cells. All cells were injected as described above. (B) Coupling mitochondrial extraction with transplantation from individual cell to cell: One quadrant of a 4-well micro-insert (ibidi) was seeded with recipient HeLa (su9-BFP) cells as described above. A second quadrant was seeded with U2OS cells continuously expressing su9-mCherry acting as donors. The transplantation was executed as described above. Subsequently the U2OS cells were removed, again using a FluidFM probe filled with 1% sodium dodecyl sulfate (Merck). Before sequencing, the whole cell population was controlled for any signal mCherry positive-cells via fluorescence activated cell sorting, but no unwanted carryover of remaining U2OS cells (mCherry+) could be detected. Control for non-specific mitochondrial carryover:

Approximately 100 000 HeLa cells expressing the mitochondrial matrix marker su9-BFP were seeded onto a culture dish. They were mixed with purified mitochondria from approximately 2×10^6 U2OS cells expressing su9-mCherry by pipetting the extracts gently on top of the cultured cells. Approaches A and B were grown for 8 days, transferred into a new culture dish and grown for another 6 days. Approach C was grown for 3 days, transferred into a new culture dish and grown for another 3 days. Subsequently, the total DNA of all samples was purified using the MasterPure™ Complete DNA and RNA Purification Kit (epicentre) following manufacturer's instructions. Part of the D-loop region was amplified via PCR using primers 1 & 2 (table S2). To create a 'null hypothesis' for the following sequencing workflow, three test-samples were created consisting of 0.1% / 0.5% / 1% U2OS amplicons, mixed with HeLa amplicons. Subsequently all samples were sequenced using the a Pacbio Sequel SMRT cell, subsequently analyzed as described in Russo et al.⁴ The reads were assigned to either U2OS mtDNA, or HeLa mtDNA using four conserved mutations of U2OS cells within this region previously identified via Sanger-Sequencing (15959G>T, 16069C>T, 16108C>T, 16126T>C; see table S1).

Statistics and reproducibility

All representative experiments were repeated at least three times independently with similar results. Absolute counts of cells or mitochondrial particles are included in the main text or in the figure legends. Analysis for single nucleotide polymorphisms was performed as described in Russo et al.⁴.

Analysis of mitochondrial quality control mechanisms with mitochondrial transplantation in primary HEKa cells.

Cells were seeded into as described above, into low μ -dishes (ibidi) inside two-well culture inserts (ibidi). The special separation allows for drug-treatments of the donor cell population before the experiment, while the host cell population of HEKa cells remains under standard culture conditions. At the beginning of the experiment, the cell media was replaced with CO₂-independent growth medium containing 10% FBS (ThermoFisher) and 1% penicillin-streptomycin (ThermoFisher). 4 μ M Oligomycin was added when indicated. Treatment conditions: 10 μ M CCCP for 3 h, 8 μ M Doxycycline for 24 h, 750 μ M H₂O₂ for 3 h. Mitochondria were extracted from HeLa cells and transplanted into HEKa cells. A Z-stack image series of the transplant and the host cell was taken directly after the transplantation process with a 63 \times oil objective with 1.4 numerical aperture and a 2 \times lens switcher in 500 nm steps. Further Z-stacks were taken at other time-points depending on the individual experiment. For the endpoint at 18 - 22 h post transplantation, the mitochondrial network was visualized using MitoTracker® Green FM (ThermoFisher) following manufacturers instructions. The overlap between the transplant and the host mitochondrial network was controlled. For the quantitative analysis, data was analyzed with self-written Matlab (R2018a) scripts which will be made available upon reasonable request.

Split-kinesin experiments. pKIF5C-HA-FRB was a kind gift from Prof. Sean Munro. Expresses fusion of Rat kinesin minus tail to FRB; pFKBP-mCh-Fis1TM was subcloned from pFKBP-GFP-myc-GRIP (Sean Munro) by swapping the GFP-myc-GRIP fragment with mCherry fused to the TM domain of yeast Fis1 for outer-mitochondrial membrane targeting. U2OS cells stably expressing mtBFP and a shRNA against DRP1³ were reverse transfected with the two constructs above. 2 days later cells were imaged using a spinning disk microscope. Rapamycin was diluted in growth medium to a final concentration of 1 nM. A microfluidic imaging device was used to allow (rapamycin-containing) medium replacement while imaging. Experiments were performed twice on different days.

Supplementary Text

Force-induced mitochondrial fission

It has previously been suggested that mitochondrial membrane constriction is a prerequisite for mitochondria fission^{3,5}; however it was impossible to exert highly localized hydrodynamic pulling forces intracellularly with sub micrometer resolution. FluidFM has the advantage of allowing to distinguish between mechanical force exertion and other cellular processes possibly involved such as calcium signaling. When extracting mitochondria, we observed induction of the pearls-on-a-string phenotype on mitochondria (Supplementary Fig. 5a), followed by division of the inner and outer mitochondrial membrane (Fig. 2d and 2e Movies 3, 4 and 5). We wondered, whether the scission process was due to mechanical forces exerted by FluidFM or by recruitment of the native mitochondrial fission machinery to these sites. A main component of this machinery is Drp1, a mechanoenzyme that assembles circularly around mitochondria and uses the energy from GTP hydrolysis to mediate membrane scission⁶. To assess the recruitment of the fission machinery to constricted sites, we expressed a fluorescently labelled version of Drp1 (Drp1-mCherry) in U2OS cells and performed mitochondrial pulling experiments to follow the fluorescent signals of both the mitochondrial matrix and Drp1. We observed that the FluidFM-induced pearls-on-a-string phenotype led to the recruitment of fluorescently labelled Drp1 (Drp1-mCherry) at the induced constriction sites of targeted mitochondrial tubes (Supplementary Fig. 5b, n = 18), thus providing a direct link between induced constriction and recruitment of Drp1.

The observed force-induced shape transition leads to the question of its relevance *in vivo*. To investigate this question further we examined kinesin as an endogenous motor protein⁷ as a potential trigger. We employed the split-kinesin strategy using rapamycin-inducible protein interactions⁸. Briefly, FK506 binding protein (FKBP) was fused to mCherry and to the transmembrane domain of Fis1 for OMM targeting. Its partner, FKBP-rapamycin binding (FRB), was fused to the motor domain of kinesin. Upon rapamycin exposure, FKBP and FRB form a stable complex, thereby coupling mitochondria to the kinesin motor domain and directs their transport on microtubules. Addition of rapamycin to cells expressing these constructs induced a global shape transition of mitochondria similar to that observed upon FluidFM aspiration (Supplementary Fig. 5c), suggesting that hydrodynamic pulling forces created by FluidFM aspiration are in a similar range as forces created by kinesin motor proteins.

These results are congruent with previous studies suggesting that mitochondrial membrane constriction is a prerequisite for mitochondria fission^{3,5,9}.

An indicator of plasma membrane damage and an inducer of mitochondrial pearling is leakage of calcium ions into the cytoplasm and mitochondria¹⁰. Mammalian cells tightly control calcium concentrations whereby the ER acts as Ca²⁺ storage compartment and mitochondrial pearling and subsequent fission has previously been associated with Ca²⁺ signaling^{11,12}. To investigate whether Ca²⁺ flux is associated with shape transition of mitochondria in our approach, we used the Ca²⁺ sensitive fluorophore mito-R-GECO1¹³ targeted to the mitochondrial matrix and followed mitochondrial Ca²⁺ dynamics in time-lapse microscopy experiments. We observed no change in signal intensity of R-GECO1, neither after probe insertion, nor during the extraction process (Supplementary Movie 6). To control for functionality of the sensor system, we probed the initially extracted cells twice (n = 17). In the second approach, we manually displaced the probe while it was inside the cell, inducing rupture of the cytoplasmic membrane. Because the cell culture medium contains roughly a 6000-fold excess of calcium compared to mitochondria¹⁰, we expected an influx of Ca²⁺. Indeed, a systemic Ca²⁺ influx signal of mito-R-GECO occurred, propagating radially from the probe insertion site, followed by rounding of mitochondria and cell death (Supplementary Movie 7), in line with Ca²⁺ inducing apoptosis via cytochrome *c* release from mitochondria¹⁰. A similar mitochondrial calcium influx was observed when using imperfectly coated probes that we expected to result in localized Ca²⁺ influx upon membrane puncture. Indeed, we observed a rapid and transient increase of R-GECO1 fluorescence intensity in mitochondria upon probe insertion. However, there was no immediate influence on the

mitochondrial morphology. Only when negative pressure was applied, ‘pearling’ of mitochondrial tubes was observed exclusively in direct proximity of the aperture. The morphology of mitochondria situated further away did not change, despite being equally affected by the Ca^{2+} influx (n=14) (Supplementary Fig. 6a and Supplementary Movie 8). Finally, we depleted Ca^{2+} in the medium by adding the chelating agent EGTA. Under this condition, the signal intensity of R-GECO1 did not rise, neither upon probe entry nor during the mechanically induced fission process (Supplementary Fig. 6b and Supplementary Movie 9). To rule out an involvement of calcium stored within the ER, we treated U2OS-cells with thapsigargin, which depletes the ER calcium reservoir. We did not detect any impact of thapsigargin on force induced pearling of mitochondria (Supplementary Fig. 6c). Based on these results, we conclude that calcium influx is not linked to the observed mitochondrial shape transition. Due to the directional propagation along mitochondrial tubes, rather than a radial propagation from the site of probe insertion, as well as lacking evidence of an influence of calcium on the observed process, we conclude that hydrodynamic pulling forces rather than a biochemical signal is responsible for mitochondrial pearling and fission.

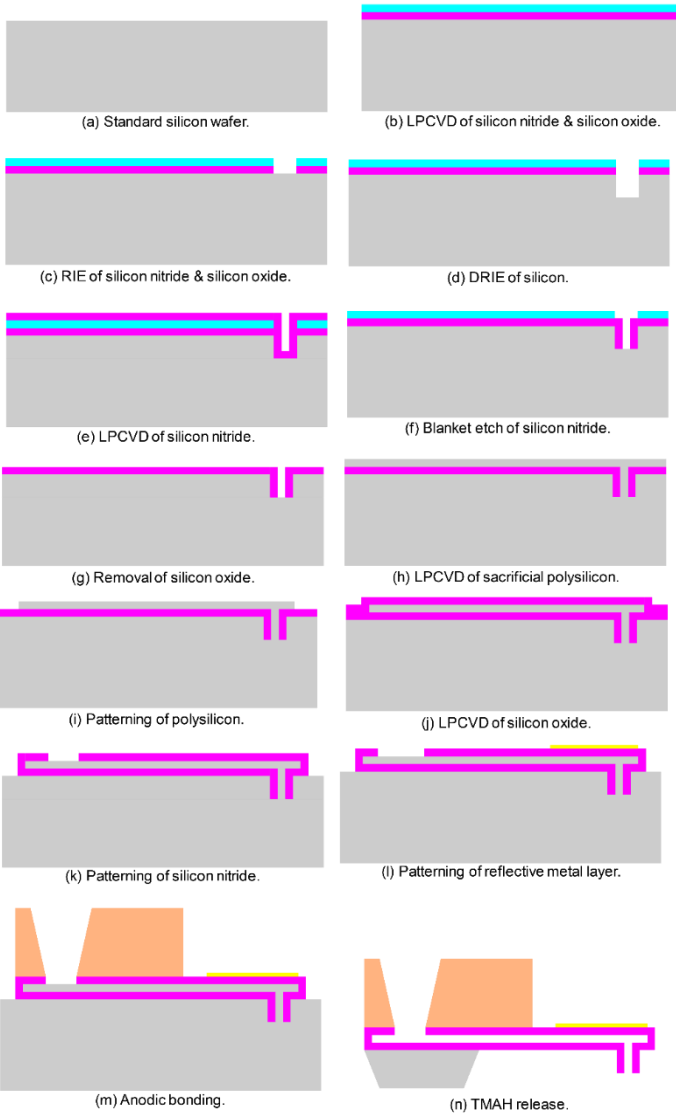
Above, we show that FluidFM can be used to apply intracellular tensile forces, allowing for the study of mechanobiological processes intracellularly and in real time. While compressive force application can be controlled in time and space¹⁴, application of controlled tensile force was, to date, impossible. The technology developed here revealed that mechanical force can be a driver for mitochondrial shape transition strictly localized to sites of pulling force application. Our experimental data fit well to theoretical considerations¹⁵, connecting mitochondrial shape to membrane tension (amongst other factors), increase of membrane tension has ‘pearling’ as an outcome, which in turn may result in fission. Potentially damaging events are likely to play a role in eukaryotic cells that are exposed to mechanical stress. Transition into the pearls-on-a-string phenotype could be an elegant solution, protecting against membrane leakage upon mechanical stress, for instance if a mitochondrion is attached to molecular motors of diverging directions, or when a cell as a whole is being stretched. In particular, mitochondria must travel through meters of axons and dendrites in neurons. ‘Pearling’ is frequent in these cells, and even more so when fission is inhibited⁹. Our approach opens up new opportunities to study organelle physiology and mechanobiology within viable cells.

1. Schindelin, J. *et al.* Fiji: an open-source platform for biological-image analysis. *Nat. Methods* **9**, 676–82 (2012).
2. Thyng, K. M., Greene, C. A., Hetland, R. D., Zimmerle, H. M. & DiMarco, S. F. True colors of oceanography. *Oceanography* **29**, 9–13 (2016).
3. Helle, S. C. J. *et al.* Mechanical force induces mitochondrial fission. *Elife* **6**, 1–26 (2017).
4. Russo, G. *et al.* Highly sensitive, non-invasive detection of colorectal cancer mutations using single molecule, third generation sequencing. *Appl. Transl. Genomics* **7**, 32–39 (2015).
5. Carlini, L., Mahecic, D., Kleele, T., Roux, A. & Manley, S. Membrane bending energy and tension govern mitochondrial division. *BioRxiv* 1–34 (2018). doi:10.1101/255356
6. Smirnova, E., Shurland, D. L., Ryazantsev, S. N. & Van Der Blik, A. M. A human dynamin-related protein controls the distribution of mitochondria. *J. Cell Biol.* **143**, 351–358 (1998).
7. Meyhofer, E. & Howard, J. The force generated by a single kinesin molecule against an elastic load. *Proc. Natl. Acad. Sci.* **92**, 574–578 (1995).
8. van Bergeijk, P., Hoogenraad, C. C. & Kapitein, L. C. Right Time, Right Place: Probing the Functions of Organelle Positioning. *Trends Cell Biol.* **26**, 121–134 (2016).
9. Cho, B. *et al.* Constriction of the mitochondrial inner compartment is a priming event for mitochondrial division. *Nat. Commun.* **8**, 15754 (2017).
10. Ghibelli, L., Cerella, C. & Diederich, M. The dual role of calcium as messenger and stressor in cell damage, death, and survival. *Int. J. Cell Biol.* **2010**, (2010).
11. van der Blik, A. M., Shen, Q. & Kawajiri, S. Mechanisms of mitochondrial fission and fusion. *Cold Spring Harb. Perspect. Biol.* **5**, (2013).
12. Nemani, N. *et al.* MIRO-1 Determines Mitochondrial Shape Transition upon GPCR Activation and Ca²⁺ Stress. *Cell Rep.* **23**, 1005–1019 (2018).
13. Wu, J. *et al.* Improved orange and red Ca²⁺ indicators and photophysical considerations for optogenetic applications. *ACS Chem. Neurosci.* **4**, 963–972 (2013).
14. Li, Q. S., Lee, G. Y. H., Ong, C. N. & Lim, C. T. AFM indentation study of breast cancer cells. *Biochem. Biophys. Res. Commun.* **374**, 609–613 (2008).
15. Gonzalez-Rodriguez, D. *et al.* Elastocapillary Instability in Mitochondrial Fission. *Phys. Rev. Lett.* **115**, 1–5 (2015).

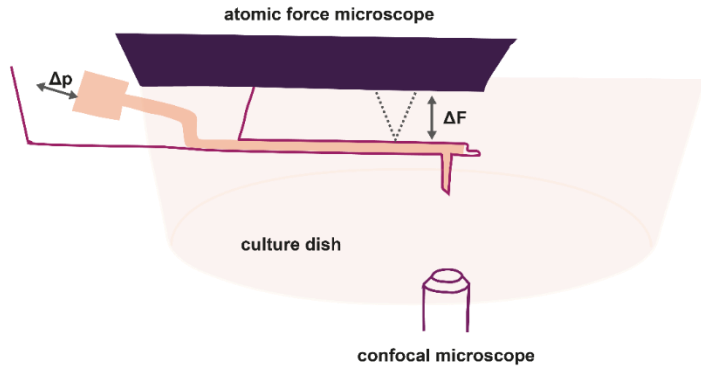
Supplementary Figures

a

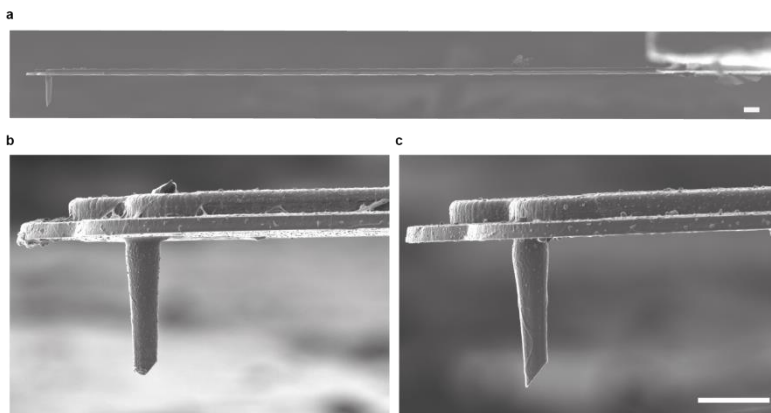
■ (Poly)silicon ■ Silicon nitride ■ Silicon oxide ■ Glass ■ Metal



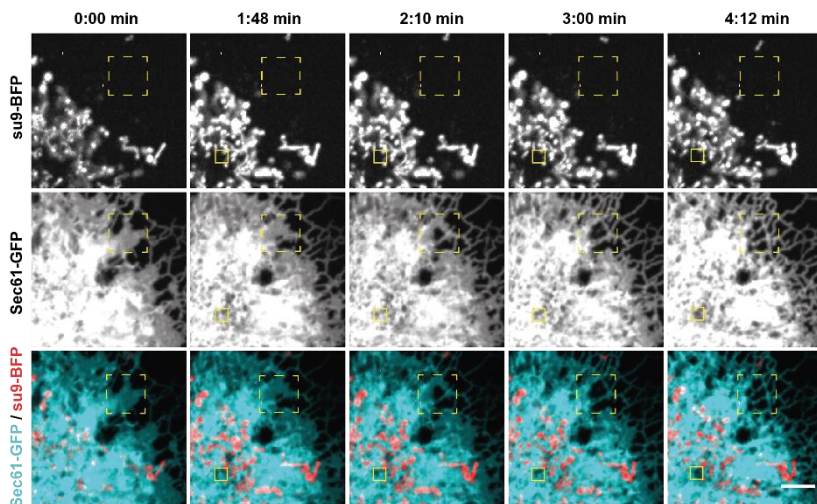
b



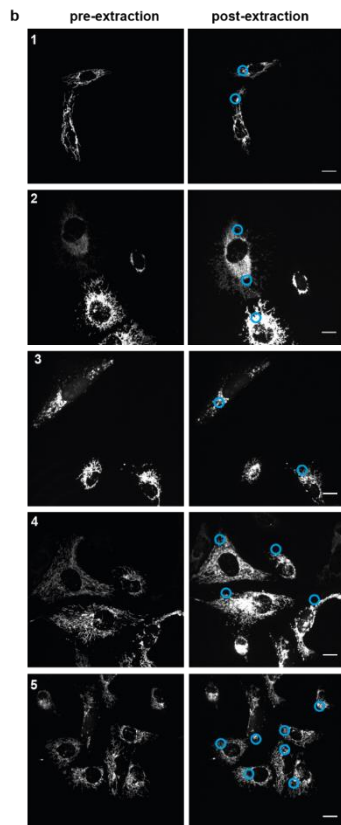
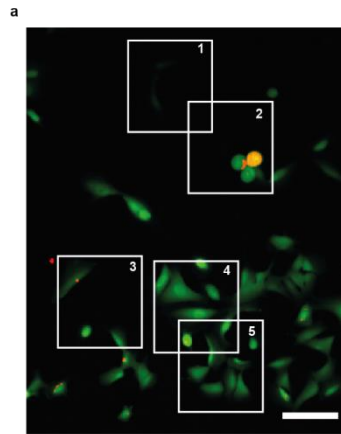
Supplementary Fig. 1: a FluidFM fabrication process. **(a-n)** Steps for the fabrication of hollow FluidFM cantilevers comprising a cylindrical apex. **b**, Schematic overview of the FluidFM setup.



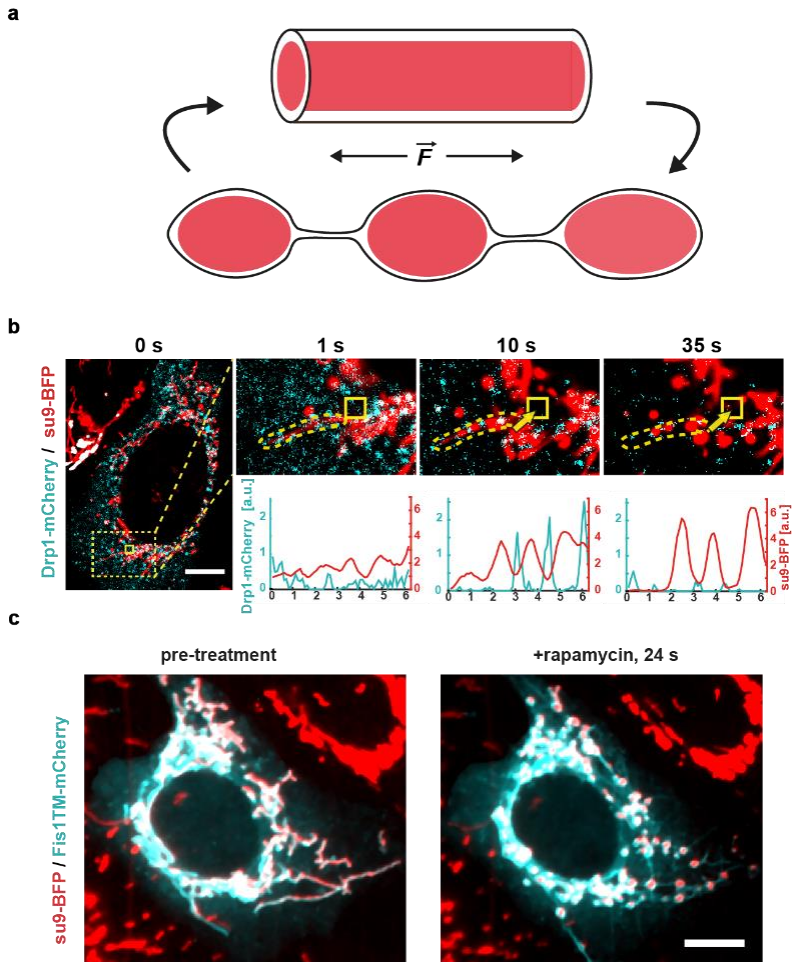
Supplementary Fig. 2: Mechanical robustness of FluidFM cantilevers comprising a sharpened cylindrical apex. Focused Ion Beam images of FluidFM cantilevers: **a**, Side view of a slanted cylindrical FluidFM cantilever with a 1.2 μm diameter of the cylinder. **b**, Cantilever that was used for mitochondrial transplantation with a setpoint of 1000 nN, the apex is broken impairing insertion of the probe into cells **c**, Cantilever that was used for mitochondrial transplantation with a setpoint of 400 nN, the apex remains intact. Scale bar: 10 μm .



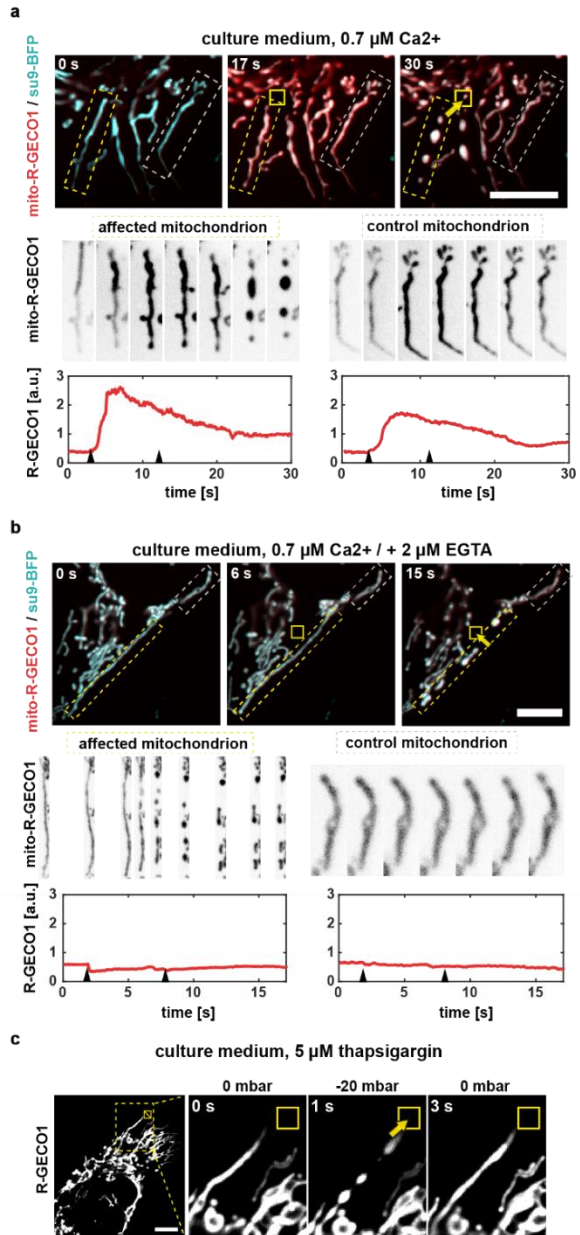
Supplementary Fig. 3: ER extraction of COS7-cells. COS7-cells stably expressing the ER membrane marker Sec61-GFP and mitochondrial matrix marker su9-BFP. Small square indicates cantilever position, big dashed line indicates a zone of ER re-arrangement. Scale bar: 5 μ m.



Supplementary Fig. 4: Viability of HeLa cells post extraction of mitochondria. **a**, Overview of HeLa cells 2 h post mitochondrial extraction, stained with the LIVE-DEAD Cell imaging kit. Viable cells show green fluorescence signal, dead cells show red fluorescence. Areas 1 - 5 show regions with extracted cells. Scale bar: 50 μm . **b**, Mitochondrial networks (su9-BFP) from the regions shown in a, before and 2 h post extraction. The insertion sites of the cantilevers for extraction are highlighted by blue circles. The experiment was conducted twice, 36 out of 37 sampled cells remained viable. Scale bar: 10 μm .

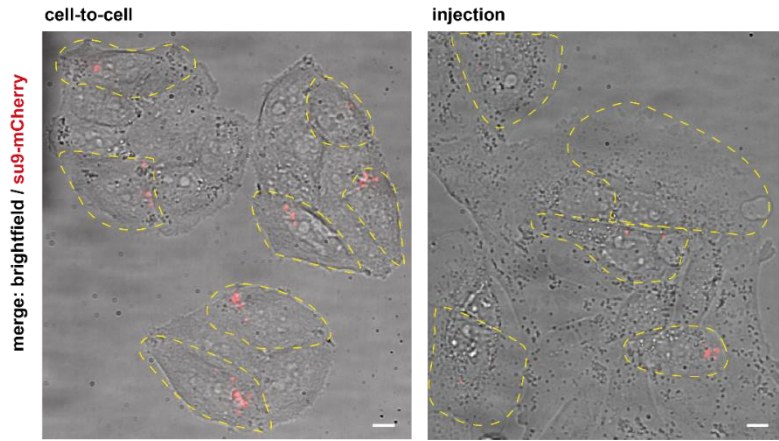


Supplementary Fig. 5: Mitochondrial shape transition and fission. **a**, Schematic representation of the working model of the shape transition into the pearls-on-a-string phenotype upon exertion of pulling forces. **b**, Image series U2OS-cells overexpressing Drp1-mCherry (cyan) and quantified fluorescent signal along mitochondrial tubes during force induced shape transition of pulled mitochondria. **c**, U2OS cell expressing kinesin-FRP (minus tail) and FKBP-Fis1. Mitochondria fragment following addition of rapamycin. Scale bars: 10 μ m.

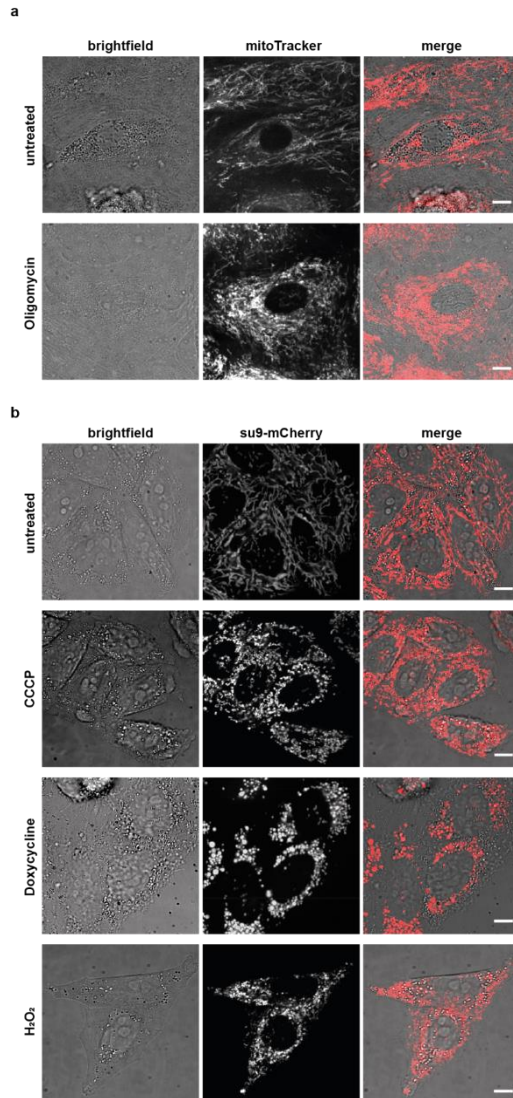


Supplementary Fig. 6: Mitochondrial shape transition is Ca^{2+} -independent. **a** and **b**, Ca^{2+} imaging series of mitochondrial shape changes. U2OS cells express su9-BFP (mitochondrial

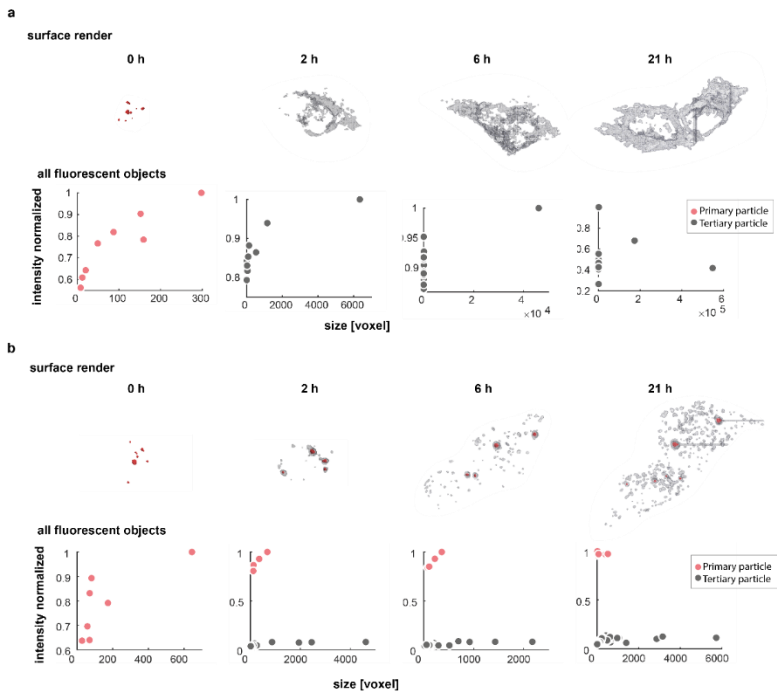
matrix, cyan) and the Ca^{2+} -sensing fluorophore mito-R-GECO1 (red). The upper panel shows an overlay of the two fluorophores during extraction. The middle panel shows an enlarged section of (left panel) a mitochondrion directly adjacent to the cantilever tip and (right panel) a peripheral mitochondrion. The bottom panel shows the total fluorescence intensity of mito-R-GECO1 of the displayed mitochondria during the manipulation process. Yellow boxes indicate position of the cantilever aperture, arrows indicate time point of application of $-\Delta p$. **a**, Experiment done in culture medium containing $0.7 \mu\text{M}$ calcium. **b**, Experiment executed in culture medium after addition of $2 \mu\text{M}$ EGTA. **c**, Pulling experiment of an individual mitochondrial tube 30 minutes after the addition of $5 \mu\text{M}$ thapsigargin. $n = 8$. Scale bars: $10 \mu\text{m}$.



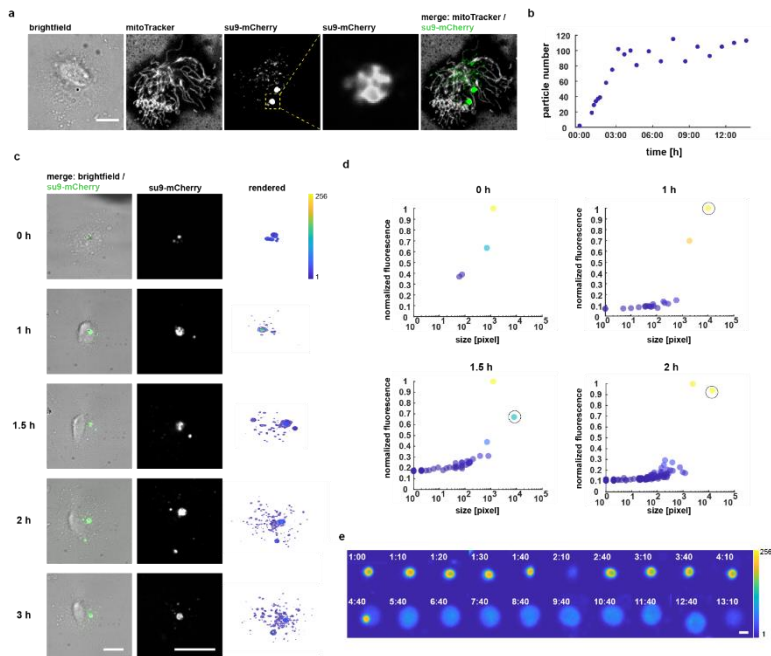
Supplementary Fig. 7: images of HeLa cells post mitochondrial transplantations via the cell-to-cell and the injection approach. Images show and overlay of brightfield (grey) and the transplant (su9-mCherry, red). Transplanted cells are outlined in yellow. Scale bars: 10 μ m



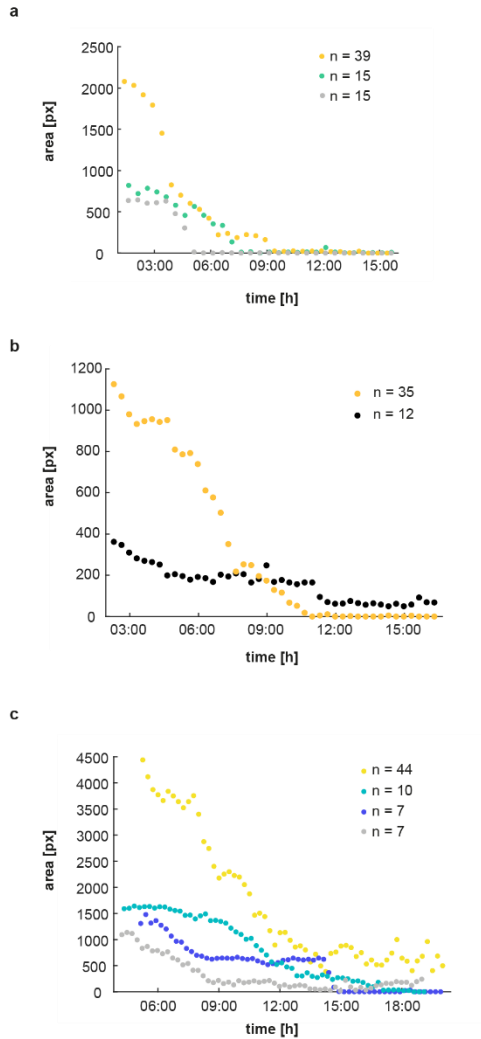
Supplementary Fig. 8 Fusion states of the mitochondrial network of HEKa cells upon drug-treatments. **a** HEKa cells in culture medium, the mitochondrial network is visualized using mitoTracker Green. Cells in the lower panel were treated with 4 μ M Oligomycin for 22 h. **b** HeLa cells in culture medium, the mitochondrial matrix is visualized via permanent expression of su9-mCherry. Treatments: 10 μ M CCCP for 3 h, 8 μ M Doxycycline for 24 h, 750 μ M H₂O₂ for 3h. Scale bars: 10 μ m.



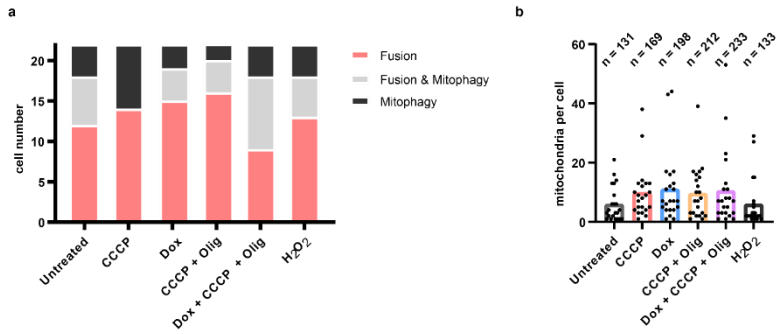
Supplementary Fig. 9 Visualisation and analysis of transplanted mitochondria in single HeLa cells. Top: surface render of the total fluorescence of the transplant over time bottom: objects plotted by size in pixel and normalized fluorescence intensity. Objects carrying the high fluorescence intensity of the initial transplant at the 0 h time point are depicted in red; objects with low fluorescence are depicted in grey. **a**, HeLa cell showing mitochondrial acceptance of 8 mitochondria within 2 h **b**, HeLa cell showing full degradation of the transplant, 7 mitochondria were transplanted.



Supplementary Fig. 10: Exemplary quantification of mitochondrial degradation in HEK293T cells. **a**, Fluorescence microscopy images of a cell 19 h post mitochondrial transplantation, 4 mitochondria were initially transplanted. The enlarged section shows a presumptive mitophagosomal structure. Scale bar: 10 μm . **b**, Total number of fluorescent objects within the host cell over time. **c**, Time-lapse images of mitochondrial degradation. Surface-rendered images of all detected fluorescent images show the increasing number and spatial distribution of particles over time. Scale bar: 10 μm . **d**, Scatter plots of objects plotted by size in pixel (logarithmic scale) and normalized fluorescence intensity. Outlined dot shows the largest tertiary particle shown in the central panel in **c**. **e**, degradation of individual mitochondria over time [h]. After fusion with a presumptive mitophagosomal structure at 4:40 hours, the degradation progresses for over 8 hours. Scale bar: 1 μm .



Supplementary Fig. 11: Fluorescent traces of the mitochondrial transplant and directly derived particles in single HEK293 cells over time. Plots show the total volume occupied by unfused mitochondrial transplant over time in various conditions. The number of initially transplanted mitochondria per cell is depicted on the upper right. **a**, Transplant was treated with CCCP and Oligomycin. **b**, Transplant was treated with Doxycycline, CCCP and Oligomycin. **c**, Transplant was treated with Doxycycline.



Supplementary Fig. 12: **a**, Fusion and degradation behavior of drug-compromised mitochondrial transplants in HEKa cells. Each condition was tested with 22 cells. **b**, Distribution of mitochondrial quantity transplanted per cell from all conditions tested in a (22 cells for each conditions). Line shows median value.

Captions for supplementary movies:

Supplementary Movie 1: ER-extraction from a COS7 cell using FluidFM. Panels from left to right: Mitochondrial matrix, su9-BFP; ER, Sec61-GFP; Merge of panels one and two: mitochondria (red) and ER (cyan). Arrowheads mark the site of extraction. Scale bar: 5 μm .

Supplementary Movie 2: Cell-wide view of ER-extraction from a COS7 cell using FluidFM. Channels from left to right: Mitochondrial matrix, su9-BFP; ER, Sec61-GFP; merge of channels one and two: mitochondria (red) and ER (cyan). Arrowheads mark the site of extraction. Scale bars: 10 μm .

Supplementary Movie 3: Extraction of mitochondria from a U2OS cells using FluidFM. Mitochondrial matrix is labelled via su9-BFP. Arrowhead indicates site of extraction. Left side: cell wide view of the extraction process; scale bar: 10 μm . Right side: enlarged view of the extraction site; scale bar: 5 μm .

Supplementary Movie 4: Extraction of singular mitochondrial sphere from a U2OS cell using FluidFM. Mitochondrial matrix is labelled via su9-BFP. Arrowhead indicates site of extraction. Left side: cell wide view of the extraction process; scale bar: 10 μm . Right side: enlarged view of the extraction site; scale bar: 5 μm .

Supplementary Movie 5: Pearling of mitochondrial tubes upon exertion of pulling force. Channels from left to right: Mitochondrial matrix: su9-BFP; outer mitochondrial membrane: Fis1TM-mCherry; merge of mitochondrial matrix (red) and outer mitochondrial membrane (cyan). Arrowheads indicate site of extraction. Scale bars: 5 μm .

Supplementary Movie 6: Calcium imaging during mitochondrial extraction without membrane disruption via FluidFM. Movie of an individual U2OS cell. Channels from left to right: Ca^{2+} sensor within the mitochondrial matrix, mito-R-GECO1; mitochondrial matrix, su9-BFP; merge of the Ca^{2+} sensor (red) and the mitochondrial matrix label (cyan). Arrowheads indicate site of extraction. Scale bar: 10 μm .


Supplementary Movie 7: Calcium imaging during membrane disruption via FluidFM. Movie of the individual U2OS cell shown in Movie S7. Channels from left to right: Ca^{2+} sensor within the mitochondrial matrix, mito-R-GECO1; mitochondrial matrix, su9-BFP; merge of the Ca^{2+} sensor (red) and the mitochondrial matrix label (cyan). Arrowhead indicates site of extraction. Scale bar: 10 μm .

Supplementary Movie 8: Calcium imaging during extraction with mild membrane disruption. Channels from left to right: Ca^{2+} sensor within the mitochondrial matrix, mito-R-GECO1; mitochondrial matrix, su9-BFP; merge of the Ca^{2+} sensor (red) and the mitochondrial matrix label (cyan). Arrowheads indicate site of extraction. Scale bars: 10 μm .

Supplementary Movie 9: Calcium imaging during extraction with mild membrane disruption after addition of EGTA. Channels from left to right: Ca^{2+} sensor within the mitochondrial matrix, mito-R-GECO1; mitochondrial matrix, su9-BFP; merge of the Ca^{2+} sensor (red) and the mitochondrial matrix label (cyan). Arrowheads indicate site of extraction. Scale bars: 10 μm .

Supplementary Movie 10: Fusion of a singular transplanted mitochondrial sphere with the mitochondrial network of a U2OS cell. Channels from left to right: Mitochondrial matrix of the transplanted mitochondrion, su9-mCherry; mitochondrial matrix of the host cell network, su9-BFP; merge: transplant mitochondria (red) and host network (cyan). Scale bar: 10 μm .

Supplementary Movie 11: Time-lapse images of mitochondrial acceptance in HEKa cells.

Left: Brightfield images. Right: Fluorescence signal of the transplanted mitochondria, su9-mCherry in the 'hot' colormap, Matlab R2018a: 1 256. The amount of the  initially transplanted mitochondria are depicted in the first and last frame next to the respective cell.

Supplementary tables:

Supplementary Table 1: Viability of HeLa cells post mitochondrial transplantation: Injection of purified mitochondria, extracted from bulk cultured cells

Control - PCR-amplified U2OS mtDNA was mixed with PCR-amplified HeLa mtDNA to the following concentrations: Ct11 - 0.1%/ Ct12 - 0.5% / Ct13 - 1%

position	Ct11.A	Ct11.C	Ct11.G	Ct11.T	Total reads	HeLa mtDNA [%]	U2OS mtDNA [%]	average [%]
15959	3	0	20059	18	20080	99.9	0.09	0.1
16069	0	19831	0	20	19851	99.9	0.1	
16108	0	19650	0	20	19670	99.9	0.1	
16126	0	19	0	19639	19658	99.9	0.1	
position	Ct12.A	Ct12.C	Ct12.G	Ct12.T	Total reads	HeLa mtDNA [%]	U2OS mtDNA [%]	average [%]
15959	5	0	28675	120	28800	99.57	0.42	0.47
16069	1	28388	0	141	28530	99.5	0.49	
16108	0	28139	0	140	28279	99.5	0.5	
16126	0	137	0	28129	28266	99.52	0.48	
position	Ct13.A	Ct13.C	Ct13.G	Ct13.T	Total reads	HeLa mtDNA [%]	U2OS mtDNA [%]	average [%]
15959	2	0	25492	164	25658	99.35	0.64	0.77
16069	1	25226	0	210	25437	99.17	0.83	
16108	1	25021	0	210	25232	99.16	0.83	
16126	0	201	0	25016	25217	99.2	0.8	

Transplanted - biological replicates 1-3 (i)

position	TP1.A	TP1.C	TP1.G	TP1.T	Total reads	HeLa mtDNA [%]	U2OS mtDNA [%]	average [%]
15959	0	0	27638	658	28296	97.67	2.33	2.58
16069	0	27360	0	757	28117	97.31	2.69	
16108	0	27296	0	750	28046	97.33	2.67	
16126	0	734	0	27263	27997	97.38	2.62	
position	TP2.A	TP2.C	TP2.G	TP2.T	Total reads	HeLa mtDNA [%]	U2OS mtDNA [%]	average [%]
15959	1	0	32063	498	32562	98.47	1.53	1.7
16069	1	31738	0	571	32310	98.23	1.77	
16108	0	31674	0	571	32245	98.23	1.77	
16126	0	560	0	31662	32222	98.26	1.74	
position	TP3.A	TP3.C	TP3.G	TP3.T	Total reads	HeLa mtDNA [%]	U2OS mtDNA [%]	average [%]
15959	0	0	15191	221	15412	98.57	1.43	1.58
16069	0	15097	0	253	15350	98.35	1.65	
16108	1	15081	0	252	15334	98.35	1.64	
16126	0	247	0	15084	15331	98.39	1.61	

Injected - biological replicates 1-3 (ii)

position	Inj1.A	Inj1.C	Inj1.G	Inj1.T	Total reads	HeLa mtDNA [%]	U2OS mtDNA [%]	average [%]
15959	0	0	12555	79	12634	99.37	0.63	0.7
16069	0	12434	0	92	12526	99.27	0.73	
16108	2	12403	0	92	12497	99.25	0.74	
16126	1	88	0	12398	12487	99.29	0.7	
position	Inj2.A	Inj2.C	Inj2.G	Inj2.T	Total reads	HeLa mtDNA [%]	U2OS mtDNA [%]	average [%]
15959	0	0	23824	116	23940	99.52	0.48	0.56
16069	0	23609	0	137	23746	99.42	0.58	
16108	1	23567	1	140	23709	99.4	0.59	
16126	0	135	0	23569	23704	99.43	0.57	
position	Inj3.A	Inj3.C	Inj3.G	Inj3.T	Total reads	HeLa mtDNA [%]	U2OS mtDNA [%]	average [%]
15959	0	0	29343	35	29378	99.88	0.12	0.14
16069	0	29123	0	44	29167	99.85	0.15	
16108	2	29080	0	45	29127	99.84	0.15	
16126	0	42	0	29075	29117	99.86	0.14	

Mixed - biological replicates 1-3 (iii)

position	Mixed 1.A	Mixed 1.C	Mixed 1.G	Mixed 1.T	Total reads	HeLa mtDNA [%]	U2OS mtDNA [%]	average [%]
15959	2	0	38482	3	38487	99.99	0.01	0
16069	0	38329	0	1	38330	100	0	
16108	0	38281	0	0	38281	100	0	
16126	1	0	0	38265	38266	100	0	
position	Mixed 2.A	Mixed 2.C	Mixed 2.G	Mixed 2.T	Total reads	HeLa mtDNA [%]	U2OS mtDNA [%]	average [%]
15959	2	0	32911	0	32913	99.99	0	0
16069	0	32764	0	1	32765	100	0	
16108	1	32725	0	1	32727	99.99	0	
16126	0	0	0	32719	32719	100	0	
position	Mixed 3.A	Mixed 3.C	Mixed 3.G	Mixed 3.T	Total reads	HeLa mtDNA [%]	U2OS mtDNA [%]	average [%]
15959	3	0	38647	0	38650	99.99	0	0
16069	0	38446	0	0	38446	100	0	
16108	0	38402	0	1	38403	100	0	
16126	0	0	0	38389	38389	100	0	

Supplementary Table 2: Primers used in this study

Name	Binding site mtDNA	Sequence 5' – 3'
Primer 1	15720	ATTGACTCCTAGCCGCAGAC
Primer 2	16298	AAGGGTGGGTAGGTTTGTG

IV Engineering of synthetic endosymbioses using FluidFM injection of bacteria into host cells

Christoph G. Gäbelein, Michael Reiter, Chantal Ernst, Julia A. Vorholt

Institute of Microbiology, ETH Zürich, Zürich, Switzerland

Abstract

Synthetic endosymbiosis provides a defined starting point for studying fundamental processes in symbiogenesis. Here, we model the initial stages of an endosymbiont-host relationship by injecting commensal bacteria directly into the cytosol of cultured HeLa cells and analyzing intracellular growth behavior using fluorescence microscopy. To match the growth of the merged pair of cells, we generated auxotrophic mutants of a laboratory strain of *Escherichia coli* and introduced them into host cells. We found that *E. coli* mutants, auxotrophic in amino acid biosynthesis- and uptake have little effect on intracellular growth rate, while defects in purine synthesis considerably slow down intracellular growth, however inhibit intracellular cell division. The experimental framework provides unique opportunities to test and engineer the behavior and co-growth of cell-cell mergers in a fully accessible synthetic system.

Introduction

Endosymbioses are symbiotic relationships in which one partner, the endosymbiont, is incorporated within a living host cell. This type of close and long term biological interaction is widespread in nature, e.g. in land plants, where endosymbiotic bacteria fix nitrogen in exchange for nutrients and shelter¹. Endosymbiosis drives fundamental evolutionary developments in unifying two separate entities metabolically and genomically, it's most famous example being eukaryogenesis: Eukaryotic cells likely emerged from an endosymbiosis between an endosymbiont bacterium related to Alphaproteobacteria and an archaeal host some 2 billion years ago^{2,3}. However, evolutionary younger endosymbioses exist in nature, revealing common patterns in the evolution of host-endosymbiont pairs like gene transfer from endosymbiont to host and conjunct biosynthesis of metabolites⁴⁻⁷.

Boundary conditions for the formation of a stable merger between two organisms are under debate⁸ and there are several challenges that need to be overcome in order to create a stable unicellular host-endosymbiont pair, one of the requirements being a matching growth speed. Once the endosymbiont resides inside the host cytosol, three scenarios present themselves: (i) The host cell grows faster than the endosymbiont, resulting in loss of the symbiont within one-or several generations (Fig. 1a). (ii) The endosymbiont grows faster than the host, inevitably draining the host of nutrients and killing it (Fig. 1b). (iii) Similar growth rate of both organisms, stable co-growth is possible (Fig. 1c).

Active mechanisms need to be in place to regulate growth rates of host and symbiont in order to ensure a stable partnership. Nutrient allocation and metabolic co-regulation were speculated to be major factors in the establishment and stabilization of host-endosymbiont pairings, but the weighting of individual contributing factors in such a complex setting are unknown and hard to dissect^{9,10}. In nature, the host is often predicted to be dependent on the endosymbiont, while the endosymbiont is not necessarily dependent on the host organism. In this case, the host is speculated to facilitate matching of growth rates actively; 'host control' over endosymbiont load was reported to be enforced via nutrient limitation^{11,12}. Whether there are other mechanisms for regulating co-growth is a matter of speculation, theoretical considerations suggest that self-limited division of endosymbionts is in general possible¹³. Whether coordinated metabolic regulation alone is sufficient to achieve stable synchronized growth of host and endosymbiont remains an open question that is difficult to answer by studying natural endosymbioses. Endosymbioses formed in nature already went through evolutionary processes resulting in a stable organism, a development that is difficult to infer due to genetic drift of the two ancestral organisms and changing environmental conditions. Therefore, the use of naturally occurring

endosymbioses for the study of isolated scientific questions is problematic because the complex environmental backgrounds under which they evolved cannot be accounted for. Furthermore, the investigation of natural host-endosymbiont pairs is aggravated by practical hurdles such as long generation time and limited genetic accessibility¹⁰.

The establishment of artificial biological systems provides an opportunity to tackle questions regarding the boundary conditions and early steps of co-regulation. Recently, a first synthetic merger between *Escherichia coli* and *Saccharomyces cerevisiae* was published¹⁰, as a first step towards an artificial minimal system, but central characteristics of the system like parallelization of growth speed or resource allocation remain to be investigated. *E. coli* has been extensively studied over the years and the organism provides a great platform as endosymbiotic partner for synthetic biology¹⁴. However, its metabolic capabilities far outstretch the capabilities of evolved endosymbiotic bacteria like *Buchnera* and *Wigglesworthia*, who likely underwent large genome reduction events¹⁵⁻¹⁷. This might indicate that the reduction of metabolic capabilities from once larger genomes as present in *E. coli* is part of the establishment and stabilization of stable host-endosymbiont pairs.

To create a synthetic minimal system for the analysis of intracellular growth rate and its regulation in context of the intracellular environment of a host cell, cytoplasmic entry has to be facilitated. Several publications describe genetic and chemical modifications facilitating cell-entry and phagosomal escape of non-invasive bacterial strains¹⁸, however these protocols need to be adapted for every tested strain and may influence the strains growth behavior. An alternative delivery protocol of bacteria into the cytosol of mammalian cells consists in the use of microinjection devices^{19,20}. Among such devices, fluidic force microscopy (FluidFM) is particularly promising. The technology features an atomic force microscope (AFM) that connects the ability of microinjection devices to dispense small volumes (fL - pL) with the precision of an atomic force microscope²¹. Recent developments show the transfer of mitochondria in between cells utilizing a novel set of FluidFM probes harboring a cylindrical apex that allow for the injection of mitochondria into cultured cells (see chapter III). Here, we expanded the toolbox of the FluidFM platform for the introduction of non-pathogenic *E. coli* bacteria into cultured HeLa cells for the analysis of their intracellular growth speeds. We explore the impact of rationally designed metabolic *E. coli* mutants, aiming to match the growth speeds of *E. coli* to that of cultured HeLa cells as the designated host organism, in order to explore the genetic impact of shrinking metabolic capabilities towards host-endosymbiont stability.

Results

Bacteria injection via FluidFM and evaluation of intracellular growth

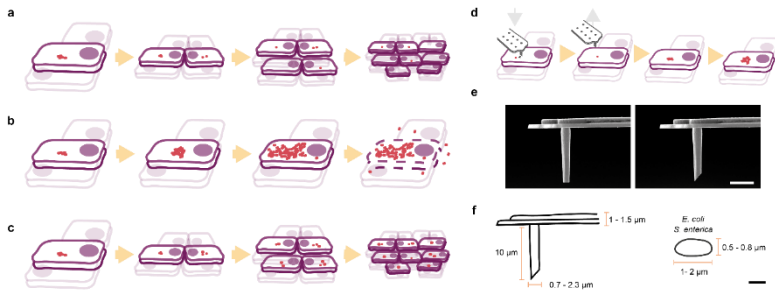


Figure 1: Intracellular growth and bacteria injection via FluidFM. **a-c**, Schemes for possible growth scenarios of possible host-endosymbiont pairs. **a**, Host grows faster than the endosymbiont. **b**, Endosymbiont grows faster than the host. **c**, Host and endosymbiont show similar growth rates. **d**, Schematic view of bacteria injection experiments using FluidFM. **e**, SEM-images of cylindrical FluidFM-cantilevers pre- (left) and post- (right) milling via FIB for injection experiments. Scale bar: 5 μm. **f**, Size constraints of FluidFM cantilevers for bacteria injection. Scale bar: 1 μm.

In order to create a cell merger between a bacterial cell and a eukaryotic cell, we adapted the FluidFM platform towards injection of bacteria into mammalian cultured cells. Cantilevers featuring a cylindrical apex, sharpened using a focused ion beam, were proven to be minimally invasive and allowed injection of mitochondria (Fig. 1e). Absolute dimensions of the hollow channel of FluidFM cantilevers can be fine-tuned to fit cargo sizes (Fig. 1f). In this study, we optimized FluidFM cantilever dimensions towards efficient injection of *E. coli* bacteria: The fluidic channel had a height of 1 μm and cylinder diameters of 1.2 μm. Smaller sizes (< 1 μm) are prone to be clogged by the dispensed bacteria while larger sizes (> 1.4 μm) are less efficient in facilitating bacterial injection because the aperture needs to be fully inserted into the cytoplasmic membrane and larger apertures are more likely to protrude from the cell.

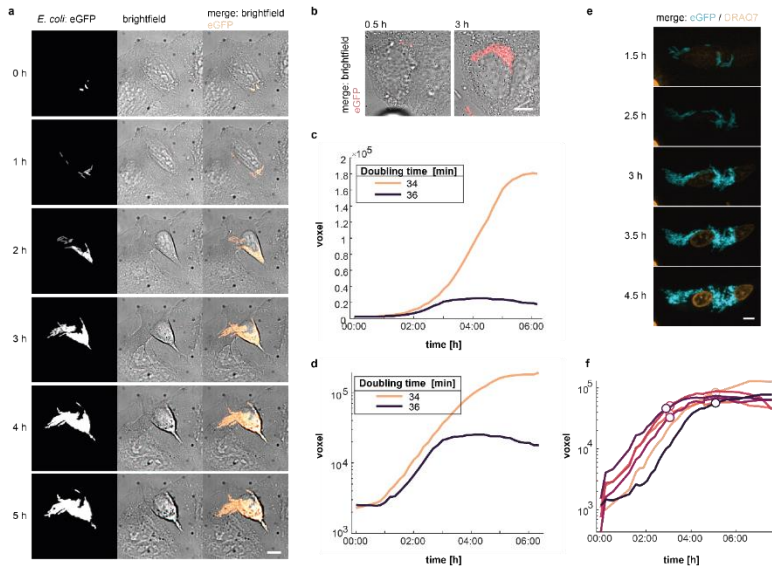


Figure 2: Intracellular growth of injected Bacteria. **a**, Time-lapse series of *E. coli* cells injected into HeLa cells. Scale bar: 10 μ m. **b**, Microscopy images of injected *S. enterica* cells, directly after – and 3 h post injection. Scale bar: 10 μ m. **c**, Growth curve of intracellular *E. coli* cells within single host cells. **d**, Growth curve of intracellular *E. coli* cells within a single host cell with a logarithmic scale, same data as in **c**. **e**, Time-lapse series of DRAQ7 influx into HeLa during

In a first set of experiments, we injected a laboratory strain of *E. coli* (BW25113) and *Salmonella enterica* bacteria into cultured HeLa cells and followed the behavior of host cell and injected bacteria. To reassure purely intracellular growth, we added 5 μ M gentamicin to the culture medium, an antibiotic not permeating eukaryotic membranes²². Both bacteria strains expressed a constitutive cytosolic fluorescent marker (eGFP) enabling optical control of intracellular growth. *E. coli* ($n = 43$) and *S. enterica* ($n = 16$) proliferate within HeLa cells after injection into the cytoplasm (Fig 2a and b respectively). These results stand in contrast to a previous study: Goetz et al observed intracellular growth after microinjection exclusively for facultative intracellular pathogens in Caco-2, HepG2 and J774 macrophage cells, but not for extracellular bacteria strains, including an *E. coli* strain¹⁹.

The injected *E. coli* cells exhibited variations in their lag phases and absolute cell yield within individual HeLa cells, which complicated the assessment of growth rates. Therefore, we developed a protocol to quantify bacterial load within mammalian cells based on fluorescence microscopy, using intensity thresholding. The approach allowed investigation of bacterial cell growth from Z-stack data (Supplementary Fig. 1) and extraction of growth curves from single bacterial cells to small intracellular populations (Fig. 2c, d). We observed that the yield of *E. coli*

cells per injected HeLa cell varied greatly (Fig. 2c), while the growth speed remained constant for individual bacterial strains, independent of total *E. coli* cell doublings (Fig. 2d). The calculated mass doubling times matched those previously observed for *Shigella flexneri* cells²³ (37 ± 4 min), a close relative of *E. coli* harboring similar metabolic capabilities.

To have an indication of host cell viability in relation to the intracellular cell mass and growth rate exhibited by *E. coli*, we used the nucleic acid stain DRAQ7. DRAQ7 does not permeate intact plasma membranes of living cells, therefore, influx correlates with damaged plasma membranes and apoptosis²⁴. We simultaneously monitored the fluorescent signal of intracellularly growing *E. coli* cells and the fluorescence signal of DRAQ7 in the cell nucleus and observe an onset of DRAQ7 fluorescence after 3 h for the depicted cell (Fig. 2e). The rise of DRAQ7 fluorescence correlates with deceleration of *E. coli* growth (Fig. 2f). This behavior was expected, since influx of the DRAQ7 dye likely correlates with Gentamicin influx from the culture media.

Having established protocols for the determination of *E. coli* growth from volumetric fluorescence data and HeLa cell death via DRAQ7 influx time points, we approximated the absolute *E. coli* cell numbers per host cell at the time of membrane permeabilisation. Assuming, that the average *E. coli* cell size remains constant within an individual experiment, we calculated and averaged voxel number for a single *E. coli* cell in our setup: 522 ± 120 voxel. We estimated an absolute cell number of 110 ± 23 *E. coli* cells per HeLa cell, corresponding to 6-7 doublings. Within this experimental series we injected between 1 and 6 *E. coli* cells into individual HeLa cells, but the initial bacterial load had no influence on the absolute cell yield, single injects resulted in 129 ± 17 cells ($n = 12$) per HeLa and double / triple injects resulted in 101 ± 24 ($n = 17$) cells per HeLa.

In summary, we showed injection of a laboratory strain of *E. coli* and *S. enterica* bacterial cells into cultured HeLa cells. Furthermore, we established a method for the quantification of intracellular *E. coli* growth, yielding mass doubling times, time points of HeLa cell death and absolute bacterial cell numbers. In the current state, the interaction between *E. coli* and HeLa follows scenario ii, i.e. *E. coli* grows faster than its host, resulting in HeLa cell death 2-5 h post injection (Fig. 1b). Thus, in order to match growth speeds of the 'endosymbiont' (37 min) and the host (23 hours²⁵), the endosymbiont needs to reduce its doubling time by a factor of ~ 37 .

Growth rate evaluation of metabolically impaired *E. coli* mutants

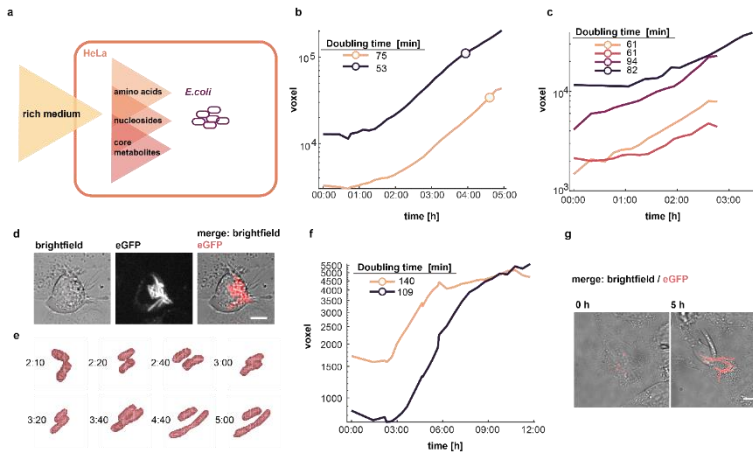


Fig 3: Intracellular growth behavior of *E. coli* metabolic mutants. **a**, Schematic of nutrient fluxes for the HeLa-*E. coli* pair. **b**, Intracellular growth curves of *AproC* mutants. **c**, Growth curves of mutants deficient in phenylalanine synthesis- and uptake. **d**, Fluorescence-microscopy images of *AguaB* mutants 4 h post injection. **e**, Surface render of individual intracellular growing *AguaA* *E. coli* cells over time upon addition of 10 μ M guanine. **f**, Growth curves of the intracellular growing *AguaA* strain, supplemented with 10 μ M guanine. **g**, Fluorescence-microscopy images of filamentous intracellular growth of the *AguaA* strain supplemented with 50 μ M guanine.

Conceptually, the cell cytoplasm is a growth environment which is rich in nutrients. These nutrients are in part supplemented in the cell culture media surrounding the host cell and in part synthesized by the host cell itself; thus, their concentrations may vary within a certain range depending on cell state (Fig 3a). Despite being rich in nutrients, the cytoplasmic compartment of mammalian cells is not generally considered permissive for intracellular growth^{19,26}. Previous studies showed ambiguous outcomes depending on the host cell type and cell state, as well as inherent metabolic properties of different bacteria^{27,28}. We wondered, whether it is possible to slow down *E. coli* growth by introducing metabolic deficiencies, aiming to create bottlenecks in interplay with the host cell metabolism. To couple the metabolism of *E. coli* and HeLa, we focused on metabolites that have to be synthesized from HeLa and are not supplemented in the culture media. Blockages in the flux of core metabolites exhibiting a high intracellular flux are more likely to establish rapid feedback on cell growth because they influence synthesis of basic cell building blocks such as lipids, cell wall or DNA components. Low flux metabolites, like vitamins, were shown to have a delayed impact on bacterial cell growth²⁹.

First, we investigated amino acid auxotrophs, starting with a mutant in proline synthesis (*AproC*). Proline is not supplemented in the cell culture medium. In consequence, the mutant depends on proline synthesized by the host cell. *E. coli* was able to grow with a slight reduction in growth

speed (Fig. 3b, ± 64 minutes). Next, we tested a mutant deficient in phenylalanine synthesis and uptake (*ApheA*, *ApheP*, *ΔaroP*, *ΔlivHMGKF*), with similar results (doubling time: 75 ± 14 min). We concluded that *E. coli* is able to compensate amino acid auxotrophies either by non-specific uptake by other amino acid importers or by the uptake of peptides³⁰.

These results prompted us to focus on another core pathway: purine biosynthesis. We chose a strain comprising a knockout in the *guaB* gene (inosine 5'-monophosphate dehydrogenase). Again, the doubling time was about 1 h (58 ± 13 min). The cells grew elongated in later growth phases (Fig 3d), hinting towards an impairment of cell the division machinery. The inosine 5'-monophosphate dehydrogenase synthesizes the first step from Inosine-monophosphate to Guanosine-monophosphate, the second step is synthesized by the GMP-synthetase (*guaA*). The *ΔguaA* mutant did not show excessive growth leading to HeLa cell death. We observed a slow increase of cell mass of single *ΔguaA* mutant cells, but none of the injected *E. coli* cells divided within 12 h (Fig. 3e, n = 27). The doubling time based on pure mass acquisition was estimated to be > 100 min. We postulated that a lack of GTP, in the synthesis of which the GMP-synthetase is crucial, might lead to failure of the division machineries main component FtsZ, which is GTP dependant³¹. However, increasing the concentration of supplemented guanine to 50 μ M did not result in successful cell division. Instead, intracellular *E. coli* cells strongly elongated without dividing (Fig 3g). Subsequently, we tested a strain deficient in hypoxanthine biosynthesis, another precursor in the synthesis of purines (*ApurE::kan*, *AdeoD*, *Δgsk*, *Δgpt*). The mutant grew wild-type like with a doubling time of 39 ± 3.7 min (Supplementary Fig. 2).

The observed growth behavior of *E. coli* highlights its broad metabolic capabilities aggravating the creation of metabolic bottlenecks. Furthermore, pleiotropic effects such as the observed filamentous growth and disabled cell division of auxotrophic mutants in guanine metabolism caused by distortions of central carbon metabolism are hard to predict. Since deficiencies in individual pathways showed only minor effects on intracellular growth speeds, additional work is required to identify suitable key steps in individual pathways in order to stabilize the *E. coli* – HeLa relationship.

Discussion

In this study, we introduce FluidFM as an efficient tool to inject bacteria into cultured cells while preserving viability of both organisms. The newly developed FluidFM cantilevers with cylindrical diameters ranging from 0.7 – 2.3 μ m allow the injection of bacteria with a minimum ferret diameter smaller than the corresponding cylindrical diameter. Using fluorescently labelled

bacteria and analyzing their growth via fluorescence microscopy, we deduced intracellular growth from individual injected cells. The calculated doubling times are well in line with literature values²³. The use of fluorescence microscopy for the evaluation of bacterial cell masses provides a powerful tool for the analysis of intracellular growth behavior of bacteria and can be extended to hosts other than cultured mammalian cells. Further development of image software might enable to study behavior of the bacterial cell cycle in constantly changing nutrient conditions. This could be achieved by the use of deep learning tools³².

We chose to investigate whether the host-endosymbiont pair HeLa and a laboratory strain of *E. coli* can be pushed towards a stable relationship via introduction of metabolic bottlenecks of *E. coli*. The metabolic versatility of *E. coli* in its means to produce energy and assimilate carbon make it hard to create actual metabolic shortages leading to slower growth rates, as discovered for mutants deficient in amino acid synthesis. Furthermore, this versatility inhibits the development of self-regulatory growth modes for the merger because *E. coli* can switch to other resources to fuel its growth. The creation of bottlenecks in the synthesis of central cellular building blocks like purines or cell wall components is another promising strategy. It may however, lead to unpredictable pleiotropic effects, as discovered in the case of the *AguaA* mutant, which led to a severely reduced doubling time in terms of mass acquisition, but also to defects in cell division.

We used a K12 laboratory strain of *E. coli*, which was not evolved for intracellular growth, therefore the observed robust intracellular growth was surprising. Generally, it is not surprising that the order of Enterobacterales, to which *E. coli* belongs, is prone towards the development of pathogenic strains. Even with several mutations and deficiencies within the core metabolism, *E. coli* is still able to proliferate intracellularly with minimal impact on its growth speed behavior. This indicates that major rearrangements of its core metabolism will be necessary to create clear metabolic feedback behavior between host and endosymbiont. In nature, likely a combination of metabolic feedback and active control of the host seem to be the key for the generation of stable host-endosymbiont pairings, effectively limiting metabolic scenarios in which the endosymbiont proliferates excessively. Endosymbionts in nature undergo massive reduction of genome size, simultaneously shrinking their network of metabolic pathways as observed e.g. in the genus of Buchnera³³. ‘Slimmer’ genomes, being general pattern also observed in obligate pathogenic bacteria, are speculated to be the result of Muller’s Ratchet^{33,34}. Muller’s Ratchet describes genome reduction resulting from accumulating loss of function mutations together with the failure to recover wild-type genotypes through recombination in isolated symbiont lineages. Active selective pressure could arise from the fact that broad metabolic capabilities of intracellular proliferating bacteria may provide an ‘involuntary’ thread to a stable host-

endosymbiont relationship by providing a possible escape from controlled growth. Hence, a major driving force of genome reduction might be host control over cell division of the endosymbiont.

We show that removal of single metabolic pathways is not sufficient in order to stabilize host-endosymbiont relationships and that, in the case of *E. coli*, a far more extensive reduction of metabolic capabilities will be necessary. This conclusion is underlined by the genome sizes of the endosymbiotic bacteria *Buchnera* (630-650 kb) or *Wigglesworthia* (698 kb) compared to *E. coli* (4.5 – 5.5 Mb)¹⁷.

A stable endosymbiotic relationship requires one cell doubling of the endosymbiont population during the host cell cycle. Therefore, activation of cell doubling within a limited timeframe of the host cell cycle could also lead to similar growth rates. This could be achieved by making *E. coli* growth dependent on a metabolite that fluctuates throughout the host cell cycle.

Besides passive metabolic regulation host may develop means to control endosymbiont growth speed actively, i.e. using antimicrobial peptides (AMPs). The best studied AMPs act extracellularly by having adverse effects on cell wall and membrane, making them porous and thus lysing invading microbes³⁵. In an osmotically protective environment like the cytoplasm however, even cell wall degradation does not necessarily result in lysis of a microbe³⁶, hence AMPs are commonly observed in host-endosymbiont systems controlling rather than killing the endosymbiont³⁷. Endosymbionts in multicellular hosts like aphids or plants are usually separated within dedicated organs, where their growth is isolated from the host organism as a whole and tightly controlled both on the metabolic level- and via the expression of antimicrobial peptides³⁸; however, similar control mechanisms also exist in single-celled host-endosymbiont pairs³⁹.

The development of host-endosymbiont pairs is a multi-faceted process in which many mechanisms occur simultaneously, making it hard to make out individual contributing factors. With the development of bacterial injection via FluidFM, we provide a first step towards the ability to re-investigate parts of fundamental biological processes including endosymbiont formation and organogenesis. The use of model organisms in our study also aims at long-term exploitation of synthetic cell mergers for basic research including mutual symbiosis and pathogenicity, as well as biotechnological applications.

References

1. Markmann, K. & Parniske, M. Evolution of root endosymbiosis with bacteria: how novel are nodules? *Trends Plant Sci.* **14**, 77–86 (2009).
2. Martin, W. & Müller, M. The hydrogen hypothesis for the first eukaryote. *Nature* **392**, 37–41 (1998).
3. Gould, S. B. Membranes and evolution. *Curr. Biol.* **28**, R381–R385 (2018).
4. Ku, C. *et al.* Endosymbiotic origin and differential loss of eukaryotic genes. (2015). doi:10.1038/nature14963
5. Marin, B., Nowack, E. C. M. & Melkonian, M. A Plastid in the Making : Evidence for a Second Primary Endosymbiosis. **156**, 425–432 (2005).
6. Graf, J. S. *et al.* Anaerobic endosymbiont generates energy for ciliate host by denitrification. *Nature* **591**, 445–450 (2021).
7. Smith, T. E. & Moran, N. A. Coordination of host and symbiont gene expression reveals a metabolic tug-of-war between aphids and *Buchnera*. *Proc. Natl. Acad. Sci. U. S. A.* **117**, 2113–2121 (2020).
8. Zimorski, V., Ku, C., Martin, W. F. & Gould, S. B. Endosymbiotic theory for organelle origins. *Curr. Opin. Microbiol.* **22**, 38–48 (2014).
9. Martin, W. & Müller, M. The hydrogen hypothesis for the first eukaryote. *Nature* **392**, 37–41 (1998).
10. Mehta, A. P. *et al.* Engineering yeast endosymbionts as a step toward the evolution of mitochondria. *Proc. Natl. Acad. Sci.* **115**, 11796–11801 (2018).
11. Lowe, C. D., Minter, E. J., Cameron, D. D. & Brockhurst, M. A. Shining a Light on Exploitative Host Control in a Photosynthetic Endosymbiosis. *Curr. Biol.* **26**, 207–211 (2016).
12. Herren, J. K. *et al.* Insect endosymbiont proliferation is limited by lipid availability. *Elife* **3**, e02964 (2014).
13. Uchiumi, Y., Ohtsuki, H. & Sasaki, A. Evolution of self-limited cell division of symbionts. *Proc. R. Soc. B Biol. Sci.* **286**, (2019).

14. ALLEN G. MARR. Growth Rate of Escherichia coli. *Microbiol. Rev.* **55**, 316–333
15. Shigenobu, S., Watanabe, H., Hattori, M., Sakaki, Y. & Ishikawa, H. Genome sequence of the endocellular bacterial symbiont of aphids Buchnera sp. APS. *Nature* **407**, 81–86 (2000).
16. Akman, L. *et al.* Genome sequence of the endocellular obligate symbiont of tsetse flies, *Wigglesworthia glossinidia*. *Nat. Genet.* **32**, 402–407 (2002).
17. Wernegreen, J. J. Genome evolution in bacterial endosymbionts of insects. *Nat. Rev. Genet.* **3**, 850–861 (2002).
18. Grillot-courvalin, C., Goussard, S., Ojcius, D. M. & Courvalin, P. Functional gene transfer from intracellular bacteria to mammalian cells. **16**, (1998).
19. Goetz, M. *et al.* Microinjection and growth of bacteria in the cytosol of mammalian host cells. *Proc. Natl. Acad. Sci. U. S. A.* **98**, 12221–12226 (2001).
20. Wu, T. *et al.* Photothermal Nanoblade for Large Cargo Delivery into Mammalian. *Anal. Chem.* **83**, 1321–1327 (2011).
21. Meister, A. *et al.* FluidFM: Combining atomic force microscopy and nanofluidics in a universal liquid delivery system for single cell applications and beyond. *Nano Lett.* **9**, 2501–2507 (2009).
22. Vaudaux, P. & Waldvogel, F. A. Gentamicin antibacterial activity in the presence of human polymorphonuclear leukocytes. *Antimicrob. Agents Chemother.* **16**, 743–749 (1979).
23. Kentner, D. *et al.* Shigella reroutes host cell central metabolism to obtain high-flux nutrient supply for vigorous intracellular growth. *Proc. Natl. Acad. Sci. U. S. A.* **111**, 9929–9934 (2014).
24. Akagi, J. *et al.* Real-time cell viability assays using a new anthracycline derivative DRAQ7®. *Cytom. Part A* **83 A**, 227–234 (2013).
25. Liu, Y. *et al.* Multi-omic measurements of heterogeneity in HeLa cells across laboratories. *Nat. Biotechnol.* **37**, 314–322 (2019).
26. Agapakis, C. M. *et al.* Towards a synthetic chloroplast. *PLoS One* **6**, 1–8 (2011).
27. Ray, K., Marteyn, B., Sansonetti, P. J. & Tang, C. M. Life on the inside: The

- intracellular lifestyle of cytosolic bacteria. *Nat. Rev. Microbiol.* **7**, 333–340 (2009).
28. Eisenreich, W., Rudel, T., Heesemann, J. & Goebel, W. Persistence of Intracellular Bacterial Pathogens—With a Focus on the Metabolic Perspective. *Front. Cell Infect. Microbiol.* **10**, 1–25 (2021).
 29. Hartl, J., Kiefer, P., Meyer, F. & Vorholt, J. A. Longevity of major coenzymes allows minimal de novo synthesis in microorganisms. *Nat. Microbiol.* **2**, (2017).
 30. Garai, P., Chandra, K. & Chakravorty, D. Bacterial peptide transporters: Messengers of nutrition to virulence. *Virulence* **8**, 297–309 (2017).
 31. Mukherjee, A., Dai, K. & Lutkenhaus, J. Escherichia coli cell division protein FtsZ is a guanine nucleotide binding protein. *Proc. Natl. Acad. Sci. U. S. A.* **90**, 1053–1057 (1993).
 32. Weigert, M., Schmidt, U., Haase, R., Sugawara, K. & Myers, G. Star-convex polyhedra for 3D object detection and segmentation in microscopy. *Proc. - 2020 IEEE Winter Conf. Appl. Comput. Vision, WACV 2020* 3655–3662 (2020). doi:10.1109/WACV45572.2020.9093435
 33. Moran, N. A. & Wernegreen, J. J. Lifestyle evolution in symbiotic bacteria : insights from genomics. **15**, 321–326 (2000).
 34. Muller, H. J. The relation of recombination to mutational advance. *Mutat. Res. - Fundam. Mol. Mech. Mutagen.* **1**, 2–9 (1964).
 35. Bahar, A. A. & Ren, D. Antimicrobial peptides. *Pharmaceuticals* **6**, 1543–1575 (2013).
 36. Kawai, Y., Mickiewicz, K. & Errington, J. Lysozyme Counteracts β -Lactam Antibiotics by Promoting the Emergence of L-Form Bacteria. *Cell* **172**, 1038-1049.e10 (2018).
 37. Mergaert, P., Kikuchi, Y., Shigenobu, S. & Nowack, E. C. M. Metabolic Integration of Bacterial Endosymbionts through Antimicrobial Peptides. *Trends Microbiol.* **25**, 703–712 (2017).
 38. Masson, F., Zaidman-Rémy, A. & Heddi, A. Antimicrobial peptides and cell processes tracking endosymbiont dynamics. *Philos. Trans. R. Soc. B Biol. Sci.* **371**, (2016).

39. Singer, A., Poschmann, G., Rensing, S. A. & Nowack, E. C. M. Massive Protein Import into the Early-Evolutionary- Stage Photosynthetic Organelle of the Amoeba *Paulinella chromatophora* Massive Protein Import into the Early-Evolutionary-Stage Photosynthetic Organelle of the Amoeba *Paulinella chromatophora*. 2763–2773 (2017). doi:10.1016/j.cub.2017.08.010
40. Baba, T. *et al.* Construction of *Escherichia coli* K-12 in-frame, single-gene knockout mutants: The Keio collection. *Mol. Syst. Biol.* **2**, (2006).
41. Cormack, B. P., Valdivia, R. H. & Falkow, S. FACS-optimized mutants of the green fluorescent protein (GFP). *Gene* **173**, 33–38 (1996).
42. Schindelin, J. *et al.* Fiji: an open-source platform for biological-image analysis. *Nat. Methods* **9**, 676–82 (2012).
43. Thyng, K. M., Greene, C. A., Hetland, R. D., Zimmerle, H. M. & DiMarco, S. F. True colors of oceanography. *Oceanography* **29**, 9–13 (2016).

Material and Methods

FluidFM probe processing and FIB-SEM imaging and milling

FluidFM-probes were mounted into a custom probe holder and coated with an 13 nm carbon layer using a CCU-010 Carbon Coater (Safematic) before milling by a FIB-SEM Helios 5UX (Thermo). Cylindrical probes used for mitochondrial transplantation experiments were ‘sharpened’ by milling the probe apex at a 50° angle alongside the cylinder at an acceleration voltage of 10 kV at 40 pA, with the slanted side facing towards the back of the probe. Probes were optically controlled after the milling procedure.

Then, the probes were glued onto a cytoclip holder by Cytosurge. Before each experiment, the cantilevers were cleaned by a 90 s plasma treatment (Plasma Cleaner PDG-32G, Harrick Plasma) before coating overnight with liquid SL2 Sigmacote (Sigma-Aldrich) for 10 seconds and subsequently rinsed with ddH₂O. The cantilever spring constant was measured using software-implemented scripts (cylindrical probes: $1 \pm 0.4 \text{ Nm}^{-1}$). The probes were back-filled (into the reservoir) with bacteria in buffered solution (see below).

Bacteria culture and preparation for injection

Single mutants were acquired from the KEIO stock collection⁴⁰. Strains were fluorescently labelled with the plasmid pDGUV-GFP⁴¹. Strains were grown to stationary phase on an agar plate (24 – 48 h, 37°C), subsequently the bacteria were resuspended in 500 µl low-salt injection buffer (10 mM 4-(2-hydroxyethyl) piperazine-1-ethanesulfonic acid (HEPES), 150 mM NaCl in Millipore (pH = 7.4 with KOH). Spun down (3 min at 3000g) and washed three times in low-salt injection buffer. The OD₆₀₀ was adjusted to 2, 15 µl of the bacterial solution were then back-

filled into the FluidFM cytoclip reservoir. Metabolic mutants were controlled for a viability of >90 % using the LIVE/DEAD™ BacLight™ Bacterial Viability Kit (Invitrogen) following manufacturers instructions.

FluidFM setup and Microscopy

The FluidFM setup is composed of a FlexAFM 5-NIR scan head controlled by a C3000 controller (Nanosurf), a digital pressure controller (ranging from -800 mbar to +1000 mbar), and Microfluidic Probes (Cytosurge). The scan head is mounted on an inverted AxioObserver microscope equipped with a temperature-controlled incubation chamber (Zeiss), the incubation chamber was pre-heated to 37°C for experiments. The microscope is coupled to a spinning disc confocal microscope (Visitron) with a Yokogawa CSU-W1 scan head and an EMCCD camera system (Andor). For all images and videos, a 63× oil objective with 1.4 numerical aperture and a 2× lens switcher was used (without lens switcher: 4.85 pixel/micron and 9.69 pixel per micron with lens switcher); images are in 16bit format. Image acquisition was controlled using the VisiView software (Visitron); linear adjustments and video editing were made with Fiji⁴². Fluorescence-microscopy images of bacteria shown in the manuscript were created adding up fluorescence from individual slices to improve the signal to noise ratio and in order to improve visibility in 2D. Fluorescence microscopy images in Figure 2e were additionally noise-filtered using the wiener noise filtering function (wiener2; 3 by 3 neighborhood size) in MatlabR2020b (MathWorks). The colormap used for figures originate from Thyng et al.⁴³ Images of cantilevers containing extracts (Figure 2, Figure S4) were created by summing the slices of a Z-stack via Fiji.

Cell Culture

HeLa cells were maintained in Dulbecco's Modified Eagle Medium containing 1% penicillin-streptomycin (ThermoFisher) and 10% fetal bovine serum (ThermoFisher) culture medium at 37°C and 5% CO₂ in a humidified incubator. For experiments, cells were seeded 48 h preceding the experiment into culture dishes within dedicated zones created by using cell culture inlets (ibidi; μ -Dish, 50 mm, Low, ibidiTreat; Culture-Inserts 2 Well for self-insertion respectively). Injection experiments were executed in CO₂ Independent Medium (Gibco) supplemented with 10% fetal bovine serum (ThermoFisher). Post injections, Gentamicin was added to the culture medium a final concentration of 5 μ M.

Bacterial injection experiments via FluidFM

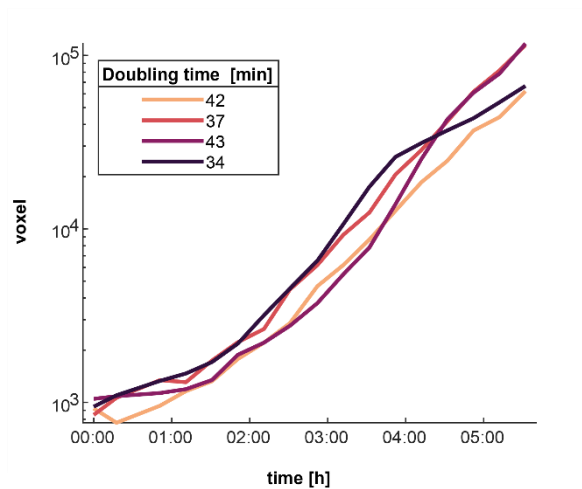
The experimental setup including bacteria, cultured cells, optical microscope and FluidFM probes were prepared as described above. For the injection, the probe was positioned above the cell, usually in close proximity to the nucleus. The probe was approached via motor + piezo to the cytoplasmic membrane using a setpoint of 42 nN and subsequently retracted for 8 μ m (50% of the piezo range). Subsequently the probe was inserted using a maximal force setpoint of 100 nN. After the setpoint was reached, effectively touching the bottom of the culture dish, the probe was retracted for 300 nm in 4 s. Then, the microfluidic pressure was set from 0 mbar to 20 – 50 mbar, simultaneously supervising the injection process via optical control to manually stop the injection process to prevent over-injection of the cell (this process usually takes between 2 and 20 s per cell). Following successful injection, the probe was retracted and moved to the next cell.

Image processing for the retrieval of intracellular growth curves

Growth curves were calculated using self-written scripts (MatlabR2020b). All code will be made available upon request. In brief, individual host cells were isolated in 3D for each timepoint, subsequently the background was separated from the signal and all 'signal' voxels are counted and plotted.



Supplementary Figure 1: Quantification of bacterial load within HeLa cells. Three-dimensional renderings of all pixels classified as 'cell' for the time-lapse experiment shown in Fig. 2a.



Supplementary Figure 2: Cell growth of *E. coli* strains auxotrophic for hypoxanthine.

V Discussion and outlook

“Those studying chaotic dynamics discovered that the disorderly behavior of simple systems acted as a creative process. It generated complexity: richly organized patterns, sometimes stable and sometimes unstable, sometimes finite and sometimes infinite, but always with the fascination of living things. That was why scientists played with toys.”— James Gleick, Chaos: Making a New Science

Biological systems are inevitably prone to stochastic fluctuations on the level of cell populations as well as within individual cells, broadening diversity on all layers. These differences are enhanced by the influence of an ever changing environment, driving cells to change their genetic structure e.g. in imperfect replication, mutational events, horizontal gene transfer, mating and cell fusion. Small differences in initial conditions do not necessarily result in chaotic behavior of the system; to the contrary, they are likely to increase robustness towards random perturbations within biological systems. The stabilizing effect of diversity is also the driver of cellular development, leading to the emergence of new species, leading to long term adaptation of changing niche requirements and increasing stability of life itself.

Chaos theory focuses on the study of dynamical systems, who seem random and irregular, yet are governed by underlying patterns and deterministic laws. The impact of these laws is highly dependent on initial conditions, and good predictions depend on precise assessment of the initial conditions. To identify the initial conditions and underlying patterns of biological systems, they need to be studied on all meta levels, i.e. the study of systemic responses, integrating a multitude of individual events within a given measurement, is as important as the study of individual building blocks of a system. Therefore, the study of individual cells, the fundamental unit of life, is crucial to foster its comprehension as a whole. The work presented in this thesis provides innovative means to perturb and analyze single cells with subcellular resolution, providing a new angle to tackle fundamental aspects of cellular evolution.

In chapter II, we show injection of fluorescent molecules and proteins into fungal cells as well as extraction of cytoplasmic content from fungal cells using FluidFM. Fungal species vary greatly in size, shape, cell wall structure and membrane composition¹, therefore current methods for cell perturbation need to be adapted for each organism. Mechanical delivery methods have the advantage of functioning independent of chemical cell wall composition and are in principle solely dependent on mechanical properties of their target cells. Therefore, they provide a methodological angle that potentially provides applicability across a wide range of otherwise inaccessible fungal species and possibly hard walled protists.

Penetration of the fungal cell wall is the most challenging hurdle to accessing the cell cytoplasm. Despite variances in chemical composition and crosslinking², its task of providing mechanical strength and withstanding changing environments leads to similar mechanical properties across fungal species³. Hence, mechanical insertion of a microfluidic probe qualifies for a broadly applicable tool to perturb fungal cells. Together with the tools developed in chapter III and IV, namely extraction of organelle structures and injection of organelles as well as bacteria, we thus potentially open up the possibility to perform dynamic studies on non-model organisms that were not accessible before.

Fungal syncytia were shown to react towards localized nutrient resources by directed growth and intra-network resource-allocation⁴. Here, FluidFM has the potential to foster mechanistic insights by depositing nutrients extracellularly and intracellularly with high spatial resolution. Injection of metabolites could furthermore deepen insights on the mechanics of resource allocation within fungal networks, or directional growth towards nutrient sources as well as influences of local osmotic pressure.

Besides abiotic stimuli, fungi are influenced by biotic factors, e.g. via infection of bacteria and mycoviruses^{5,6} and thus must have dedicated mechanisms to combat viral –or bacterial spread. Especially for larger syncytial networks or populations of single celled fungi, one would expect organism-wide or cell population-wide responses as well as more localized responses to infection events. Where the boundary between single cell- and systemic reactions towards biotic and abiotic stresses lies and whether division of labor is a universal theme relevant for fungal syncytia as well as for fungal communities remains to be investigated.

These questions extend beyond the influence of chemical and biological stimuli and include the impact of mechanical stimuli, as fungi were shown to react to cell damage by isolating parts of the injured body in order to preserve viability for the network as a whole⁷. FluidFM is able to perturb single cells by exerting mechanical pressure, by pushing or pulling cellular structures directly using the piezoelectric element to change cantilever position, or by exerting positive and negative hydrodynamic pressure. These stimuli can be applied separately or in combination extra- and intracellularly. This allows the dissection of stimuli co-occurring in nature to their individual contributions when triggering a cellular reaction. We simulated cell penetration and suction of *Coprinopsis cinerea* by the sap feeding nematode *Alphelenchus avenae* via cytoplasmic extraction using FluidFM. FluidFM could be used to direct and change intracellular fluid flows within a syncytial network, triggering direct mechanical perturbation induced by shearing forces as well as the possibility to influence intracellular pressure on a ‘cell global’ scale i.e. for all cellular parts within a connected network.

In chapter III, we show that the mitochondrial network within mammalian cells reacts in response to the mechanical trigger of hydrodynamic pulling forces. We see the transition of a tubular network into a ‘pearls-on-a-string’ phenotype in which every constriction offers a potential site for scission, effectively separating part of the network from the source of mechanical stress. Generation of the pearls-on-a-string phenotype is a physical process based on Rayleigh-Plateau instability described for viscous fluid and viscoelastic filaments⁸, therefore its occurrence in mitochondrial tubes is not surprising. However, whether this type of conversion has a general impact on mitochondrial biology remains an open question. In our experimental setup, we see induction of membrane constricted sites mediated by increased membrane tension, which in turn results in localized recruitment of the mechanoenzyme Drp1. Drp1 mediates membrane constriction by forming contractile ring having an inner diameter of 16 nm, but whether this is enough to mediate scission of the outer mitochondrial membrane is under debate⁹. In our experimental setup, the membrane tension is elevated constantly and we see recruitment of Drp1 to constricted sites followed by fission. However, the simultaneous occurrence makes it impossible to distinguish whether scission is mediated by membrane tension, recruitment of Drp1 or possibly a combination of both.

Mahecic et al. observed recruitment of Drp1 at already constricted sites of mitochondrial tubes; however, scission occurred in only 66% of all cases, while 33% of cases resulted in ‘non-productive’ Drp1 recruitment, without mitochondrial fission¹⁰. They showed that Drp1 recruitment occurs regularly at sites that are pre-constricted by tubular ER structures, similar to the pearls-on-a-string phenotype observed in our experiments. The proposed model explains that mitochondrial fission results from a combination of membrane tension and bending energy and hypothesizes that a certain tension energy barrier needs to be overcome in order to enable Drp1-mediated fission¹⁰. Our experiments show that membrane tension is propagated homogeneously along connected mitochondrial tubes. In the cellular context, this could hint towards a coordination of the fission machinery with active mitochondrial transport mediated by pulling motor proteins that, once bound and active, likely increase membrane tension similar to FluidFM-pulling. The resulting ‘mitochondria-global’ increase in membrane tension would be propagated along mitochondrial tubules and, following laws of energy minimization, result in a local peak of membrane tension at pre-constricted sites^{10,11}:

$$\tau = \frac{2\kappa}{d^2}$$

τ = membrane tension

d = tube diameter

κ = membrane bending rigidity

Independent of whether the membrane is constricted directly by force, as seen in our experiments, or by ER tubules, fission could be mediated by spatially confined membrane tension. Drp1 constriction would then act as a local amplifier by actively decreasing local tube diameter, thus increasing local membrane tension until the forces increase over a certain threshold to facilitate scission. If this is true, mitochondrial scission should also be facilitated directly via FluidFM-pulling in Drp1 knockdown or knockout cells.

We also enable extraction of cellular organelles, by tuning aperture sizes and exerting hydrodynamic forces during the extraction process. In previous work by our group, cytosolic cell extracts were analyzed using electron microscopy, mass spectrometry, qPCR, enzyme activity assays and recently via genome wide RNA-sequencing¹²⁻¹⁴. These assays are now also open for the analysis of cell extracts containing cell cytoplasm and organelle content. Extraction of organelles is adding an additional layer by facilitating analysis of the larger cellular structures and membrane-enclosed structures themselves. While mitochondria remain localized and require active transport in order to move inside the cytosol¹⁵, small molecules like RNA diffuse quickly within the cytosol ($0.6 \mu\text{m}^2/\text{s}$)¹⁶. Therefore, extraction of cytoplasm facilitates a molecular snapshot of the cell as a whole, while organelle extraction offers subcellular resolution. In addition to tuning hydrodynamic forces and aperture sizes, certain organelles are occupying locally defined spaces within the cell and can thus be excluded- or included of the extraction process by probe positioning. Subcellular resolution coupled to extract analysis opens up new opportunities for e.g. compartmental transcriptomics: it would be for example interesting to see whether certain mitochondria or fractions of the mitochondrial network differ in transcriptional activity, and how this relates to mitochondrial activity and shape phenotypes.

Furthermore, fundamental questions of how cell content, size and volume are regulated, and how this relates to organelle content, remain to be investigated. By targeted removal of certain organelles –or parts of organelles, FluidFM now offers the possibility to investigate regeneration of organelles after perturbation on a single cell level, as well as the impact of changing organelle content on cellular function. Besides removal of organelle structures, we also show direct transplantation or injection of purified organelle structures into cells. On the other end of cell size and content regulation, this technique could be used to manipulate cells towards organelle oversaturation.

The transplantation of organelles opens up several interesting aspects of multicellular organisms- and potentially closely related cell communities: Cells are generally conceived as holistic constructs who synthesize all complex structures from small molecular building blocks. The exchange of these complex structures could in the past only be traced in cases of horizontal gene transfer. Certainly, exchange of organelle structures and mutual rescue of cells within

multicellular organisms and closely related cell populations would be economically reasonable, especially in somatic cells where 'systemic fitness' of a tissue or an organism is most important. A focus lies on mitochondria, because they are the only transferable component that cannot be created *de novo* and, being central to cellular function, their transfer into recipient cells potentially affects cellular behavior and makeup in a fundamental way.

Since mitochondria play a central part in both cell metabolism and signaling while presenting a complex system themselves, their fate and impact post transfer cannot be predicted. Several reports show natural mitochondrial transfer events that were correlated with increased fitness of diverse cell types *in vivo* in mammals and plants¹⁷⁻¹⁹. In these natural settings, mitochondria are transferred via nanotubes or microvesicles in small amounts compared to the entire mitochondrial content of a recipient cell¹⁸. The transfer of 'healthy' mitochondria, i.e. undamaged and functional, might provide a direct positive impact on an impaired cell metabolism as well as a long term positive impact by transferring mtDNA content. In this manner mitochondrial transfer was proposed to impact cellular aging, which is correlated with a general decline in mitochondrial quality and activity²⁰. However, mechanistic insights and dose response relationships of mitochondrial transfer events are lacking, as well as basic knowledge on the initiation of mitochondrial transfer, like reciprocal sensing of fitness on single cell level or pathways for the initiation of organelle transfer.

Following transplantation, the transplant needs to be processed by the recipient cell. In the experiments conducted in chapter III, the transferred mitochondria either fused to the host cell mitochondrial network, were degraded, or showed an intermediary phenotype in which the transplant was restructured and both degraded and fused to the host network. In the chosen experimental setup, it was not possible to determine what influences the outcome of host cell transplant processing. Several factors could lead to transplant degradation over uptake within the recipient cells: An imperfect injection of mitochondria could leave the transplant outside the plasma membrane, albeit in close contact. In that case, the mitochondria could be taken up via phagocytosis leaving them surrounded by an additional membrane resulting in distinct transplant processing and potentially degradation. Furthermore, mitochondria are subjected to shearing forces during the extraction –or injection process, varying from cell to cell, which is potentially harming their membrane integrity and thus affecting mitochondrial quality during the transfer process. Another possible source of heterogeneity is the transplantation protocol that involves individual donor cells and individual acceptor cells. The cell cycle phase in which mitochondria are extracted from the donor cell could influence their makeup and uptake behavior as well as the cell cycle phase of the recipient cells. The mitochondria of the HeLa cells used as mitochondrial donors are likely homogeneous in terms of genomic content and mitochondrial quality, because the cell line originates from clonally expanded cells that were continuously

grown for several years since the establishment of the cell line in 1951²¹. The recipient primary HEKa cells originate from different cell donors, exhibiting genetic heterogeneity as well as differences in cell age. The cells themselves undergo an aging process once taken into culture, changing in cell shape and in their potential to divide: 'aged' HEKa cells are fully postmitotic and large compared to smaller 'young' HEKa cells, which undergo 4 to 8 doublings on average. Nonetheless, aged and young cells showed similar uptake behavior of transplanted mitochondria across the tested conditions. Additional experiments with a more homogeneous acceptor cell population would be required to assess why receptor cells act heterogeneously in response to mitochondrial transplantation.

In order to profit from the uptake of small amounts of mitochondria, cells would either need to control mitochondrial gene expression depending on individual mtDNA quality, or have mechanisms to actively propagate 'well performing' mitochondrial nucleoids while degrading impaired mitochondria. Mitochondrial quality control based on membrane potential as shown for the PINK1 / Parkin pathway for mitochondrial quality control^{22,23} qualifies for exactly this task, since the maintenance of mitochondrial membrane potential inevitably depends on functional mtDNA genes. However, the syncytial state regularly observed for somatic cells dampens the impact of malfunctioning mtDNA variants, allowing high tolerance towards poorly performing nucleoids and resulting malfunctioning proteins. Proteins diffuse rapidly throughout the mitochondrial network and cell mitochondria-wide responses exist to lessen the impact of unfolded proteins^{24,25}. To tackle these questions, the artificial transfer of different amounts of mitochondria provides the opportunity to study dose-response relationships, leading to mechanistic insights.

Mitochondrial transfer events could also act as a mediator of cell signaling, because mitochondria are also hubs of cell signaling and connect metabolic queues to cell fate decisions²⁶. Whether transferred mitochondrial subpopulations have effects on major cell fate decisions by altering the cells' metabolic state or via inducing cell signaling cascades remains to be investigated. As mediators of cell signaling, small amounts of transferred mitochondria could have a big impact i.e. by inducing apoptosis via Bak/Bax. Another cellular signaling trigger mediated by mitochondria is cytokine production as an immune response, which is transmitted via the cGAS-STING pathway that in turn is activated by mitochondrial DNA that reaches the cytosolic compartment due to formation of Bak/Bax macropores^{27,28}.

Efficient mitochondrial transfer opens up the opportunity to manipulate mitochondrial content *in vitro*, to subsequently re-introduce altered mitochondria into cells having a functional mitochondrial network –or rho0 cells. Together with DNA synthesis and advanced methods of cloning, it could be in principle possible to change the content of propagated mtDNA altogether. Koob and coworkers showed successful transfer of DNA into mitochondrial membranes via

bacterial conjugation or electroporation^{29,30} and later showed the propagation of murine mtDNA in viable yeast rho0 cells³¹. However, prove for functional activity of the transferred mtDNA is still lacking. Essential factors for uptake and maintenance of engineered mtDNA, besides basics on replication and proper packaging in mitochondrial membranes and nucleoids, were not explored so far, which could hamper approaches to incorporate synthetic mitochondrial genomes. Efficient introduction of engineered mitochondria into the cytoplasm of somatic cells represents a major bottleneck in these studies and our work provides efficient means to overcome this problem. The general idea of modifying the mitochondrial genome to enable the generation of new organelles in a synthetic bottom-up approach is fascinating and potentially opens up a new area for cell engineering.

In chapter IV we work towards a top-down approach of organellogenesis. The aim of synthetic symbiogenesis is to create a stable merger of two cells, where one cell becomes the host while the other cell becomes the endosymbiont. When unifying two systems that are in themselves only conditionally predictable, the outcome will inevitably be unpredictable. This reflects on short term aspects like metabolite exchange, growth rates and cell cycle, as well as on long-term effects influenced by the interaction between two genomes and the presence of a new cellular compartment. In eukaryogenesis, this development led to massive emergence and diversification of species, a capability potentially shared by all endosymbiotic mergers.

To reduce the likelihood of unpredictable short- and long-term behavior, we picked two model organisms as host and endosymbiont, HeLa cells and *E. coli* respectively. Based on their genomic content, the metabolic potential of the two organisms in terms of transfer and creation of desirable traits like phototrophy, nitrogen fixation or one-carbon metabolism are limited. However *E. coli* presents the greatest resource for the establishment of heterologous pathways, i.e. conversion from CO₂ into biomass³², thus enabling the transfer of engineered- as well as inherent traits.

Obviously, many more possible pairings are conceivable. Whether host and endosymbiont need to be metabolically synergistic and symbiotic in the sense that both organisms profit from the interaction is unlikely, because in natural pairings the host often tends to solely profit from the endosymbionts metabolic capabilities³³. Furthermore, the endosymbiont loses individual fitness over the course of symbiogenesis and degrades towards an obligate endosymbiont and eventually towards an organelle. Therefore, the function of the endosymbiont is to provide its host with a fitness advantage, while the sole function of the host is to provide the endosymbiont with a constant growth environment. The use of an eukaryotic organism as a host organism results mostly from the practical concern of their increased cell size compared to prokaryotic counterparts, which allows for superior means to insert and maintain one or multiple

endosymbiont cells within their cytoplasm. Single celled organisms as host cells for synthetic cell mergers are presumably favorable, because they grow steadily, are less prone to undergo apoptosis and, in the case of hard-walled eukaryotes have less extensive means to degrade 'large' foreign particles by means of xenophagy. The use of mammalian cancer cells is not fully out of line when subjected to these criteria, because in many ways, cancer cells behave like single celled organisms, they grow steadily, are less likely to undergo apoptosis and additionally have limited xenophagic capabilities^{34,35}.

The first hurdle of creating a synthetic model system for symbiogenesis, creation of a physical merger, was solved using FluidFM cantilevers developed in chapter III to inject *E. coli* directly into the cytosol of HeLa cells. We observed rapid growth (Doubling time: ± 40 min) of *E. coli* inside the cytoplasm, concluding that *E. coli* growth needs to be slowed down in order to stabilize the host-endosymbiont relationship. The creation of metabolic bottlenecks in its metabolism is straightforward; however, either the introduced bottlenecks had limited effects, or they led to pleiotropic effects downstream, i.e. the disability to divide. Therefore, *E. coli* needs to be further limited in its means to generate biomass by accumulating metabolic mutations, or perhaps another key regulator of cell growth like cell wall synthesis³⁶ could inhibit cell growth without causing unexpected deficiencies. Of course, bacterial strains exhibiting a more limited capability to adapt their metabolism towards intracellular environment will also be interesting to test.

In nature, likely a combination of metabolic feedback and active control of the host seem to be the key for the creation of stable host-endosymbiont pairings. Widely discussed is the use of antimicrobial peptides in naturally occurring endosymbioses, who are commonly expressed by eukaryotes to inhibit growth or to kill harmful microbes^{37,38}. Antimicrobial peptides target the microbial cellular membrane and inhibit its function as a natural barrier. In an osmotically non-protected environment, this leads potentially to cell lysis, whereas the effect on bacteria residing intracellularly is potentially less grave. Their broad spectrum of action and simple structure of antimicrobial peptides increases their transferability from naturally occurring endosymbioses to our system.

Further possibilities to control endosymbiont growth are the use of low doses of antibiotics, establishment of toxin-antitoxin systems, tuned host xenophagy, the use of sub-compartments within a eukaryotic cell acting as 'bacteriosome' and molecular sieve limiting nutrient availability, limiting energetic efficiency by the endosymbiont or the export of metabolically expensive products as in Mehta et al³⁹.

In conclusion, the established technologies will open up opportunities to investigate and

manipulate single cells in a novel and fundamental way. I hope that the created resources will inspire others to drive the comprehension of complex biological systems forward.

References

1. PJ, Kuhn; APJ, Trinci, MJ, Jung, MW, Goosey, LG, C. *Biochemistry of cell walls and membranes in fungi*. **37**, (1990).
2. Bowman, S. M. & Free, S. J. The structure and synthesis of the fungal cell wall. *BioEssays* **28**, 799–808 (2006).
3. Touhami, A., Nysten, B. & Dufrière, Y. F. Nanoscale mapping of the elasticity of microbial cells by atomic force microscopy. *Langmuir* **19**, 4539–4543 (2003).
4. Tlalka, M., Watkinson, S. C., Darrah, P. R. & Fricker, M. D. Continuous imaging of amino-acid translocation in intact mycelia of *Phanerochaete velutina* reveals rapid, pulsatile fluxes. *New Phytol.* **153**, 173–184 (2002).
5. Son, M., Yu, J. & Kim, K. H. Five Questions about Mycoviruses. *PLoS Pathog.* **11**, 5–11 (2015).
6. Leveau, J. H. J. & Preston, G. M. Bacterial mycophagy: Definition and diagnosis of a unique bacterial-fungal interaction. *New Phytol.* **177**, 859–876 (2008).
7. Gonçalves, A. P., Heller, J., Daskalov, A., Videira, A. & Glass, N. L. Regulated forms of cell death in fungi. *Front. Microbiol.* **8**, (2017).
8. Sattler, R., Gier, S., Eggers, J. & Wagner, C. The final stages of capillary break-up of polymer solutions. *Phys. Fluids* **24**, (2012).
9. Kalia, R. *et al.* Structural basis of mitochondrial receptor binding and constriction by DRP1. *Nature* **558**, 401–405 (2018).
10. Mahecic, D. *et al.* Mitochondrial membrane tension governs fission. *Cell Rep.* **35**, (2021).
11. Derényi, I., Jülicher, F. & Prost, J. Formation and Interaction of Membrane Tubes. *Phys. Rev. Lett.* **88**, 4 (2002).
12. Chen, W. *et al.* Genome-wide molecular recording using Live-seq. *bioRxiv* 2021.03.24.436752 (2021).
13. Guillaume-Gentil, O. *et al.* Tunable Single-Cell Extraction for Molecular Analyses. *Cell* **166**, 506–517 (2016).
14. Guillaume-Gentil, O. *et al.* Single-Cell Mass Spectrometry of Metabolites Extracted from Live Cells by Fluidic Force Microscopy. *Anal. Chem.* **89**, 5017–5023 (2017).

15. Aaron D. Pilling, Dai Horiuchi, Curtis M. Lively, and W. M. S. Kinesin-1 and Dynein Are the Primary Motors for Fast Transport of Mitochondria in *Drosophila* Motor Axons. *Mol. Biol. Cell* **17**, 5356–5372 (2006).
16. Braga, J., McNally, J. G. & Carmo-Fonseca, M. A reaction-diffusion model to study RNA motion by quantitative fluorescence recovery after photobleaching. *Biophys. J.* **92**, 2694–2703 (2007).
17. Caicedo, A., Aponte, P. M., Cabrera, F., Hidalgo, C. & Khoury, M. Artificial Mitochondria Transfer: Current Challenges, Advances, and Future Applications. *Stem Cells Int.* **2017**, (2017).
18. Liu, D. *et al.* Intercellular mitochondrial transfer as a means of tissue revitalization. *Signal Transduct. Target. Ther.* **6**, (2021).
19. Gurdon, C., Svab, Z., Feng, Y., Kumar, D. & Maliga, P. Cell-to-cell movement of mitochondria in plants. **113**, 3395–3400 (2016).
20. Sun, N., Youle, R. J. & Finkel, T. The Mitochondrial Basis of Aging. *Mol. Cell* **61**, 654–666 (2016).
21. Scherer, W. F., Syverton, J. T. & Gey, G. O. Studies on the propagation in vitro of poliomyelitis viruses: IV. Viral multiplication in a stable strain of human malignant epithelial cells (strain hela) derived from an epidermoid carcinoma of the cervix. *J. Exp. Med.* **97**, 695–710 (1953).
22. Narendra, D., Tanaka, A., Suen, D. F. & Youle, R. J. Parkin is recruited selectively to impaired mitochondria and promotes their autophagy. *J. Cell Biol.* **183**, 795–803 (2008).
23. Narendra, D. P. *et al.* PINK1 is selectively stabilized on impaired mitochondria to activate Parkin. *PLoS Biol.* **8**, (2010).
24. Sacconi, S. *et al.* A functionally dominant mitochondrial DNA mutation. **17**, 1814–1820 (2018).
25. Lin, Y. F. *et al.* Maintenance and propagation of a deleterious mitochondrial genome by the mitochondrial unfolded protein response. *Nature* **533**, 416–419 (2016).
26. Zhu, J. & Thompson, C. B. Metabolic regulation of cell growth and proliferation. *Nat. Rev. Mol. Cell Biol.* **20**, 436–450 (2019).
27. West, A. P. *et al.* Mitochondrial DNA stress primes the antiviral innate immune response. *Nature* **520**, 553–557 (2015).
28. McArthur, K. *et al.* BAK/BAX macropores facilitate mitochondrial herniation and mtDNA efflux during apoptosis. *Science (80-.)*. **359**, (2018).
29. Yoon, Y. G. & Koob, M. D. Transformation of isolated mammalian mitochondria by bacterial conjugation. *Nucleic Acids Res.* **33**, 1–8 (2005).

30. Yoon, Y. G. & Koob, M. D. Efficient cloning and engineering of entire mitochondrial genomes in *Escherichia coli* and transfer into transcriptionally active mitochondria. *Nucleic Acids Res.* **31**, 1407–1415 (2003).
31. Yoon, Y. G. & Koob, M. D. Intramitochondrial transfer and engineering of mammalian mitochondrial genomes in yeast. *Mitochondrion* **46**, 15–21 (2019).
32. Gleizer, S. *et al.* Conversion of *Escherichia coli* to Generate All Biomass Carbon from CO₂. *Cell* **179**, 1255-1263.e12 (2019).
33. Lowe, C. D., Minter, E. J., Cameron, D. D. & Brockhurst, M. A. Shining a Light on Exploitative Host Control in a Photosynthetic Endosymbiosis. *Curr. Biol.* **26**, 207–211 (2016).
34. Lu, S. L. *et al.* Endothelial cells are intrinsically defective in xenophagy of *Streptococcus pyogenes*. *PLoS Pathog.* **13**, 1–19 (2017).
35. Ygal Haupt, Sheldon Rowan, Eitan Shaulian, Karen H. Vousden, and M. O. Induction of apoptosis in HeLa cells by trans-activation-deficient p53. *Chem. Biodivers.* **3**, 742–753 (2006).
36. Cuenca, M. *et al.* D-alanine-controlled transient intestinal mono-colonization with non-laboratory-adapted commensal *E. coli* Strain HS. *PLoS One* **11**, 1–17 (2016).
37. Michael Zasloff. Antimicrobial peptides of multicellular organisms. *Nature* **415**, 389–395 (2002).
38. Mergaert, P., Kikuchi, Y., Shigenobu, S. & Nowack, E. C. M. Metabolic Integration of Bacterial Endosymbionts through Antimicrobial Peptides. *Trends Microbiol.* **25**, 703–712 (2017).
39. Mehta, A. P. *et al.* Engineering yeast endosymbionts as a step toward the evolution of mitochondria. *Proc. Natl. Acad. Sci. U. S. A.* **115**, 11796–11801 (2018).

Acknowledgements

I would like to thank Prof. Julia Vorholt, for giving me the opportunity to work in her group in this exciting field of research. For constant support and mentorship over the years, for wisdom and lots of patience. It was very important to me.

Furthermore, I would like to thank Prof. Tomaso Zambelli, for his commitment and excitement for the project and his natural talent for connecting people. I enjoyed our time together, both in science and on occasional bike rides together with Dr. Patrick Kiefer.

Sincere thanks to the members of my PhD committee, Prof. Matthias Peter, Prof. Sophie Martin, Prof. Sonja Albers, and Prof. Tomaso Zambelli for their valuable input and new perspectives.

I would like to thank my collaborators Dr. Qian Feng and Prof. Benoît Kornmann for support on all levels, and for teaching me a lot.

I am grateful for the great atmosphere, the Vorholt group has provided over the years, for always being supportive and open to discussion. I enjoyed working with you and the fun we had both in- and outside working hours, you made it easy to stay motivated day in and out.

Special thanks goes to the FluidFM, now single cell subgroup and members of my box Orane, Max, Chantal, Gabriel, Patrick, Michi, Tom and Janine. The appreciation and support of my closest peers always meant a lot to me and you always had my back. Keep up the positive spirit!

Thanks to the institute staff, the members of ScopeM and Stephen Wheeler for technical support and for providing the foundation on which this work was built.

Finally, I would like to thank my family and friends for their support and for providing a steady environment and great times throughout my studies. This would not have been possible without you.

